THE EXCITATION OF UHF SIGNALS BY PARTIAL DISCHARGE IN GAS INSULATED SUBSTATIONS

Thesis presented for the degree of

Doctor of Philosophy

in Electrical Engineering
of the University of Strathclyde

Martin David Judd, BSc
June 1996

Centre for Electrical Power Engineering
Department of Electronic and Electrical Engineering
University of Strathclyde
Glasgow
UK
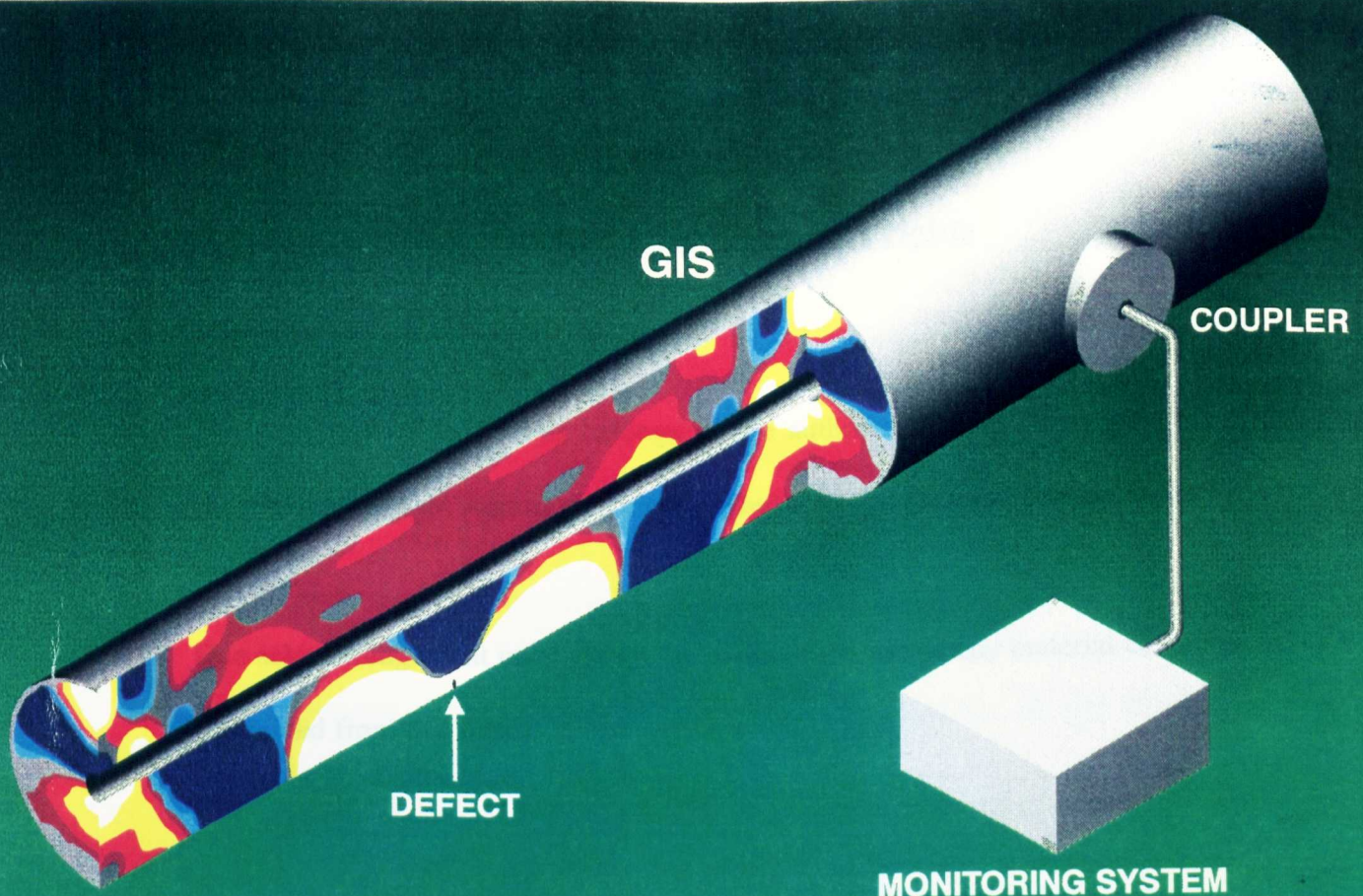
This work is dedicated to my wife Jo, who risked her own career to give me the opportunity to carry out this research.

Declaration of author's rights

The copyright of this thesis belongs to the author under the terms of the United

Kingdom Copyright Acts as qualified by University of Strathclyde Regulation 3.49.

Due acknowledgement must always be made of the use of any material contained in,

or derived from this thesis.

Abstract

This work is an investigation of the ultra-high frequency (UHF) signals excited by partial discharge (PD) sources inside gas insulated substations (GIS). PD is indicative of defects in the insulation system and by using couplers mounted at intervals along the GIS, the corresponding bursts of UHF signal can be extracted. This is the principle of the UHF monitoring technique used for detection and identification of insulation defects in GIS.

UHF diagnostics are the most useful of a range of techniques for PD detection that are reviewed. The UHF technique is compared with conventional PD measurements, illustrating the requirement for a study of the fundamental aspects covered in this research.

Current pulses from a test cell containing a needle PD source are measured using a transient digitiser with an analogue bandwidth of 1GHz. A scheme for injecting calibrated repetitive pulses to simulate PD and excite similar UHF signals is presented. Waveguide transfer functions are derived that relate the electric field at a remote UHF coupler to the current flowing at the PD source by using the dyadic Green's functions for cylindrical and coaxial configurations. These expressions are implemented in a computer simulation of the theoretical model. Experiments that validate the model are described and it is used to predict the effect of various PD parameters on the UHF signal. As a result of this research, the excitation of UHF signals by PD currents (previously understood only in general terms) can now be quantified.

A scheme for standardising UHF measurements of PD in GIS is suggested, based on the improved understanding of the processes involved. This would ensure that a GIS monitoring system is designed with adequate sensitivity to detect a critical defect. Possible topics for future research based on the theory developed in this work are discussed.

Contents

List of principal symbols

Symbol	Unit	Description
μ_0	H/m	Free space permeability
ε_0	F/m	Free space permittivity
$Z_0 = \sqrt{\mu_0/\varepsilon_0}$	Ω	Free space impedance
$c = 1/\sqrt{\mu_0\varepsilon_0}$	m/s	Free space velocity of light
λ_0	m	Free space wavelength
$\omega = 2\pi f$	rad/s	Radian frequency
$\beta_0 = \omega\sqrt{\mu_0\varepsilon_0}$	rad/m	Free space propagation constant
$J_n(x)$		Bessel function, first kind, order n
$J_n'(x)$		First derivative of the Bessel function J
$Y_n(x)$		Bessel function, second kind, order n
$Y_n'(x)$		First derivative of the Bessel function Y
n,m		Integers used in the normal designation of waveguide modes as TE$_{nm}$ or TM$_{nm}$
δ_0^n		Kronecker delta, $\quad \delta_0^n = \begin{cases} 1 & n = 0 \\ 0 & n \neq 0 \end{cases}$
$U(x)$		Heaviside unit step, $\quad U(x) = \begin{cases} 0 & x < 0 \\ 1 & x \geq 0 \end{cases}$
$\delta(x)$		Dirac delta, which has the property $$\int_a^b f(x)\delta(x-x_0)dx = \begin{cases} f(x_0) & a < x_0 < b \\ 0 & \text{elsewhere} \end{cases}$$
j		$\sqrt{-1}$
$\Re\{s\}$		Real part of s
$\Im\{s\}$		Imaginary part of s
$\hat{r}, \hat{\phi}, \hat{z}$		Unit vectors, cylindrical coordinates
$\overline{E}$		Electric field vector
Er		Radial electric field component
$\overline{J}$		Current density vector
$\overline{R}, \overline{R}'$		Position vectors, cylindrical coordinates
$\overline{\overline{G}}$		Dyadic Green's function
$\hat{r}\hat{r}, \hat{r}\hat{\phi}, \hat{\phi}\hat{z}, \ldots$		Vector dyads (see [42])

1. INTRODUCTION

1.1 Gas Insulated Substations and Partial Discharge

Gas insulated substations (GIS) are installed at power stations and key locations in electrical transmission systems across the world. The insulating properties of sulphur hexafluoride (SF_6) gas permit the electrical conductors of GIS to be assembled into a more compact structure than can be achieved in conventional air insulated substations. A GIS can be enclosed in a building and occupies a much smaller area than its air insulated counterpart. Consequently, there is less impact on the quality of the surrounding environment. Although GIS are generally very reliable [1], when internal breakdown does occur, it often causes extensive damage and an outage of several days duration is required to effect the repair. The consequences of GIS failure are costly to the transmission company and may lead to an interruption of electricity supply to its customers. If in addition the GIS links the output of a nuclear station to the transmission network and the breakdown leads to a reactor shutdown, the financial penalties could be severe. Present GIS designs have benefited from the experience gained with earlier versions, and their reliability is much improved. Nevertheless, it is often necessary to build bypass facilities into the GIS that allow important circuits to remain in service when a faulty section is isolated for repair. This reduces the likelihood a forced outage but significantly increases the cost of the installation. There is therefore an incentive to develop a more economical means of improving the GIS reliability.

One method for detecting defects in GIS is to over-stress the insulation with high ac and surge voltages during commissioning tests. If breakdown does not occur under these extreme conditions, the equipment may be considered satisfactory for use at normal operating voltages. Some obvious disadvantages to this approach are:

- The statistical nature of the breakdown caused by certain defects can result in a false indication of satisfactory performance.

- If breakdown does occur during over-stressing, there is a risk of causing unnecessary damage to components that are not defective.

- Although the insulation may initially be free of defects, there will be no indication of deterioration as the equipment ages.

For these reasons, the use of lower testing voltages accompanied by insulation diagnostics is to be preferred.

Most of the defects that could lead to eventual failure of GIS can be detected at an early stage by monitoring the installation for the presence of partial discharge (PD) [2]. Breakdown can be triggered by comparatively small internal defects [3] because the small distance between conductors results in a high electric field in the gap. An extraneous conducting body present in this field will cause increased stressing of the gaseous insulation and may lead to localised ionisation in the SF_6 gas. Current pulses flow along these ionisation paths, driven by the high voltage (HV) electric field. PD is usually quantified in terms of the amount of charge associated with these current pulses.

Published data on GIS reliability [3,4] indicates the most common cause of electrical failure to be free metallic particles. Moving under the influence of the power frequency field, a particle can strike the HV conductor, producing a micro-discharge that may trigger breakdown. Other mechanisms that can lead to failure include discharges from stress-raising protrusions and capacitive sparking from an electrode that is not properly bonded to either conductor. The common feature of all these defects is that they generate PD activity before complete breakdown occurs. GIS diagnostics are increasingly used during factory testing, site commissioning and during the service life of equipment [4,5,6,7]. Diagnostic sensors are usually specified for new GIS in the UK, and in some cases they have been retrospectively fitted to existing substations. The insulation is monitored for signs of developing PD which could be the precursor to breakdown. Preventive action can then be initiated to avert a complete failure.

1.2 Partial Discharge Detection Techniques

1.2.1 Fundamental processes

A PD is a localised current pulse caused by ionisation of the insulation in a region of high electric field stress [8], such as occurs at the tip of a metallic protrusion. The term partial discharge arises because the gap between the two conductors is only partially bridged by the ionised discharge path. This temporary ionisation normally occurs over a distance of less than 1mm in SF_6, being terminated when the electric field falls below the level required to sustain further ionisation [9,10]. For a defect such as a small protrusion on one of the conductors, the discharge takes the form of corona streamers involving current pulses with sub-nanosecond risetimes. Other discharges, such as those which occur in voids, and those associated with poor contacts and conducting particles, are also characterised by very short current pulses. The short risetime of each PD pulse creates an electromagnetic disturbance within the GIS chamber. The energy dissipated in the discharge is replaced by a current pulse from the external supply circuit. In the cases of microsparks at poor contacts and of intense coronas, the discharge is followed by a rapid expansion of gas from the ionised channel, generating an acoustic pressure wave. PD is also accompanied by the emission of light from excited molecules, and by the creation of chemical breakdown products. In principle, any of these electrical, physical and chemical consequences of PD could be used to detect its presence.

1.2.2 Chemical techniques

Dissociation of SF_6 in the discharge channel gives opportunity for the formation of other molecules. The main decomposition product is the highly reactive gas sulphur tetrafluoride (SF_4). Further reactions, typically with traces of water vapour and oxygen, lead to formation of the more stable compounds thionyl fluoride (SOF_2) and sulphuryl fluoride (SO_2F_2) [6]. These are the two most common diagnostic gases. They can be detected in concentrations as low as 1ppmv by using a gas

chromatograph and mass spectrometer. Chemical detection tubes can also be used as a simpler but less sensitive alternative [11].

Chemical techniques have the advantage that chemical decomposition is immune to electrical interference. The concentration of the diagnostic gas should accumulate, even for an intermittent source of PD, until it reaches a detectable level. In low volume laboratory test chambers a reasonably small discharge of 10-15pC can be detected, typically after some tens of hours. However, the large volume of SF_6 in a GIS would greatly dilute the diagnostic gases and a much longer detection time would result, even if a gas absorbing reagent is not used in the chambers. The chemical approach is therefore considered too insensitive for general PD monitoring in GIS [2].

1.2.3 Acoustic techniques

Acoustic signals are generated by pressure waves from thermal expansion of gas at the PD site. In the case of free particles, additional acoustic signals are generated by the mechanical action of the particle bouncing on the floor of the GIS chamber. Acoustic signals in GIS have a wide spectrum (extending from the audible range to ultrasonic frequencies in excess of 100kHz), and can travel by a number of different paths from the PD site to the detector [12]. Those propagating through the chamber wall have velocities that increase with the square of the signal frequency to a maximum of around 3000 m/s while propagation through the gas is at a much lower velocity in the region of 150 m/s. Higher frequencies in the signal are strongly attenuated during propagation through the gas, and the insulating gas barriers also attenuate the signal markedly.

The signal can be picked up by accelerometers or acoustic emission sensors mounted externally on the GIS [12]. Multiple reflections and the various signal propagation paths through differing materials result in a complex signal pattern. However, defects can be identified by techniques such as point on wave analysis, in which the

PD signal is displayed against a timebase synchronised to the power frequency. The patterns of correlation between the acoustic signals and the phase of the GIS busbar voltage are characteristic of the type of defect [13]. For example, the signal from a particle bouncing on the chamber floor is readily identified as such because it shows no correlation with the power frequency cycle. Other features can also be used to infer the shape of the particle and its movement pattern. These include parameters such as the impact rate, the crest factor (ratio of the peak signal amplitude to the rms amplitude), and the ratio of the 'lift off' to 'fall down' voltages [13].

A field measurement system based on the acoustic technique can achieve a sensitivity of typically 2pC [4]. However, due to the high attenuation experienced by acoustic signals, the technique is not suitable for a permanently installed monitoring system, because very many sensors would be required. Nevertheless, acoustic measurements have the advantage of being made non-intrusively using external sensors that can be moved from place to place on the GIS. This in itself gives the approximate position of a defect, as the largest signal should be obtained when the sensor is placed on the chamber containing the source. A more accurate location can be obtained by using a second sensor mounted at some distance from the first sensor and comparing the arrival times of the two acoustic signals.

1.2.4 Optical techniques

Detection of the light output from a discharge [14] is probably the most sensitive of all diagnostic techniques, because a photomultiplier can detect the emission of even a single photon. This option is initially appealing because it promises immunity from the electrical noise that is inevitably present in GIS, without the long time delay suffered by chemical techniques. However, radiation from PD in SF_6 occurs primarily in the ultraviolet band that is strongly absorbed by both glass and SF_6. Consequently, it is necessary to use quartz lenses and to minimise the distance between the source and detector. Although optical techniques are useful as a

laboratory tool for determining the onset of PD at a known source position, they are not suitable for detecting a discharge that could be located anywhere within a GIS.

1.2.5 Electrical techniques

1.2.5.1 Conventional method

The principle of the conventional method described in IEC Publication 270 [15] is illustrated by the schematic circuit shown in Figure 1.1. At low frequencies the GIS is equivalent to a lumped capacitance C_0 corresponding to the electrostatic capacitance between its inner and outer conductors. A coupling capacitor C_c is connected in parallel with the GIS. The voltage source U at the power frequency is effectively decoupled from the fast PD transients by the source impedance Z. Any PD induced redistribution of charge inside C_0 requires a current $i(t)$ to flow in the loop containing C_c so that the voltages across the two capacitors remain equal. This current is measured as the voltage V_m developed across a measurement impedance Z_m connected in series with C_c. The measured charge Δq_m released from C_c is determined by integrating $i(t)$. If the values of C_0 and C_c are known, the *apparent charge* Δq_a induced on the terminals of C_0 as a result of the PD can be determined from the relationship [16]

$$\frac{\Delta q_m}{\Delta q_a} = \frac{C_c}{C_0 + C_c} \qquad (1.1)$$

Although the amount of charge involved in a PD is tiny compared to that stored in the GIS, the rapid rate of change of the PD current allows it to be detected using a suitable filter, despite the much higher displacement currents flowing in the circuit at the power frequency. The measurement system can be calibrated by injecting a short current pulse of known charge into the GIS terminals. This calibration can be used to verify the operation of the equipment and to assess its measurement sensitivity. PD levels are expressed in terms of the apparent charge. When the location and structure

6
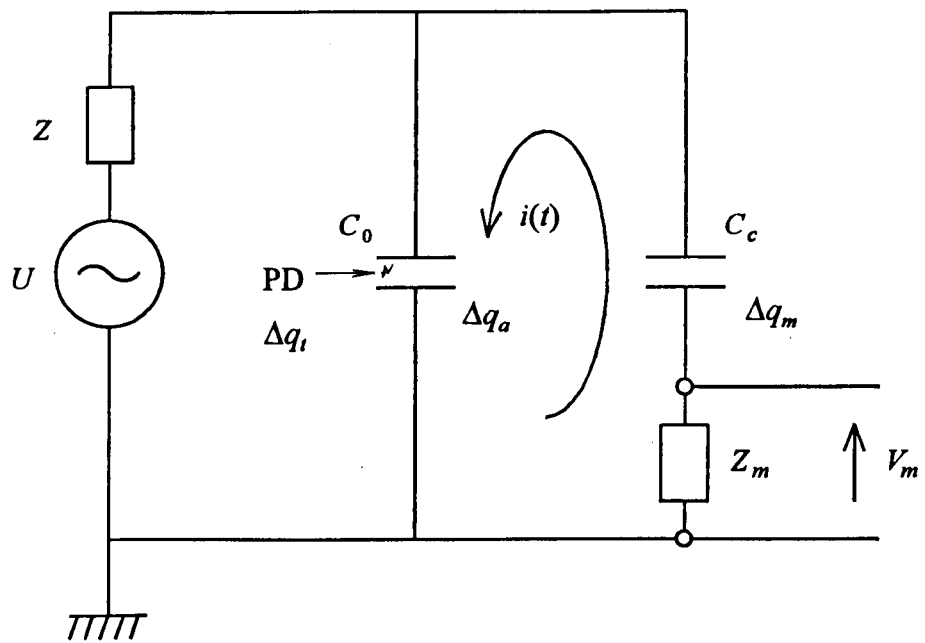
C_0	GIS capacitance
C_c	coupling capacitance
Z_m	measurement impedance
Δq_a	apparent charge
Δq_t	true charge
Δq_m	measured charge

Figure 1.1 Schematic representation of the conventional PD measurement circuit.

of the PD source are not known, the apparent charge cannot be related to the true charge Δq_t transferred at the defect [8,15,16,17].

To obtain maximum sensitivity, a completely shielded measurement configuration is required [15,18]. While this is acceptable for a laboratory test it may be inconvenient when testing a complete GIS. Equation (1.1) indicates that $\Delta q_m = \Delta q_a$ when $C_c \gg C_0$, but in the case of GIS this condition cannot be realised and it is likely that $C_c < C_0$, so that the measurement sensitivity is reduced. Construction of the coaxial coupling capacitor is similar to that of a normal GIS busbar because it must withstand the same HV levels. If the coupling capacitor is not to represent a major addition to the cost and complexity of a GIS it must of necessity be much smaller, resulting in a low capacitance ratio. Therefore a complete GIS must be divided into sub-assemblies for testing if a reasonable sensitivity is to be achieved. PD sources cannot be located using the conventional method because the GIS appears as a simple lumped capacitance. Furthermore, GIS are not normally fitted with a coupling capacitor, so the technique cannot be used for in-service measurements.

1.2.5.2 Introduction to high frequency methods

While the movement of gas ions is relatively slow, the electronic component of the PD pulse, typically of risetime <500ps [19], can contain significant spectral energy to frequencies in excess of 1500MHz. The resulting electromagnetic disturbance propagates within the network of coaxial transmission lines formed by the GIS structure. Extraction of the high frequency signal using sensors known as couplers [20] enables detection of the PD. A monitoring system connected to couplers mounted at intervals along the GIS can record these signals, to provide a warning of developing faults.

High frequency methods for PD detection are usually subdivided into the VHF (30-300MHz) [4,21,22] and UHF (300-3000MHz) [4,23,24] ranges, although the same coupling sensors [25] are often employed for both measurements.

1.2.5.3 VHF measurements

The VHF method bridges the gap between the conventional and UHF electrical methods. Therefore VHF measurements benefit somewhat from the lower interference levels present at higher frequencies. With suitable processing and calibration the signals can also be related to the conventional apparent charge measurement [4,21].

The sensor has a small capacitance (typically <1pF [25]) to the centre conductor, and forms a high pass filter when it is loaded by a 50Ω measurement system. The frequency band for the measurements is often restricted to 100-300MHz in practice because of this effect [4]. Signals measured within this range can be converted to lower frequencies for processing with conventional PD measurement equipment. Provided the whole system is linear, calibration in terms of apparent charge is possible. This is possible because the 300MHz upper limit of the VHF range normally does not exceed the frequency above which higher order electromagnetic modes begin to propagate in GIS of sizes typical for voltage ratings ≤400kV. Therefore only a single mode of propagation occurs in the VHF band and there is minimal signal dispersion. However, recent work has shown that by limiting the measurement bandwidth to frequencies below the cut-off of higher order modes, a large proportion of the total available signal energy is lost [26]. This can cause a significant reduction in the sensitivity of PD detection.

1.2.5.4 UHF measurements

The UHF method involves detecting PD signals at frequencies above 300MHz. The spectrum of these signals tends to be broadband in nature and often extends to above

1500MHz [23]. The many modes of signal propagation that become possible at UHF result in complicated signal patterns that bear no obvious relationship to the PD pulse. Thus, while the technique has been shown to be very sensitive, the lack of a theoretical basis has remained a drawback.

Systems for monitoring PD activity in GIS using UHF methods have developed substantially over the past few years [24,27]. The condition of GIS insulation can be monitored remotely, giving an immediate warning of PD activity that could lead to subsequent breakdown [7]. For continuous monitoring of a 400kV GIS, UHF couplers are fitted approximately 20m apart to provide coverage of the complete substation and to enable location of PD sources by time of flight measurements [27]. The UHF PD detection technique can equally be applied to sub-assemblies during manufacture.

All high frequency PD detection techniques are subject to the effects of electromagnetic interference. The background noise levels in GIS fed by cable connection are usually very low, but when entry is by overhead line, signals from corona discharge may be fed into the chambers. The intensity of the interference signal from air corona falls rapidly with increasing frequency, and for this reason it is preferable to make measurements in the UHF range. Signals from communications equipment such as portable telephones may also be picked up, but these are usually restricted to narrow frequency bands and can be recognised and suppressed using techniques such as adaptive filtering. Internal GIS switching can also generate high frequency signals at the couplers. These can be rejected by time-domain gating during switching operations.

1.3 Principles of UHF Detection of PD in GIS

1.3.1 Comparison with conventional PD measurements

UHF monitoring systems have been in use at substations for several years [28] and are increasingly regarded as standard equipment for GIS by the electrical utilities. The principal advantages of the UHF method are its sensitivity, the possibility of locating discharges accurately by time of flight measurements, and that it can be used for continuous remote monitoring. In contrast to the conventional technique, the UHF signals generated by PD can be detected at a nearby coupler regardless of the total size of the GIS. However, the lack of a calibration procedure for UHF PD measurements has remained a contentious issue.

1.3.2 Diagnostic techniques

In addition to being used for PD detection and location, UHF signals can be processed for conventional displays that assist with defect classification [4,29], such as a phase resolved point on wave display [30,31]. In a monitoring system, the PD signals can be digitised and stored in a data file containing amplitude and phase position information [7]. By this means, the temporal development of a PD can be displayed, indicating whether the PD is becoming more severe or is changing in character. A three dimensional display of the processed PD signal is most helpful in this respect, and some examples are given in Figure 1.2 to illustrate the characteristic patterns generated by typical defects. The vertical axis in these plots indicates the relative amplitude of the detected UHF pulses. The other two axes show consecutive cycles of the 50Hz power frequency and the phase position (point on wave) of each PD pulse on the cycle. The three examples shown are as follows:

- Figure 1.2(a) shows PD from a free metallic particle. The particle bounces asynchronously with the power frequency and generates a random pattern of pulses whose magnitude depends on the change in potential of the GIS conductor
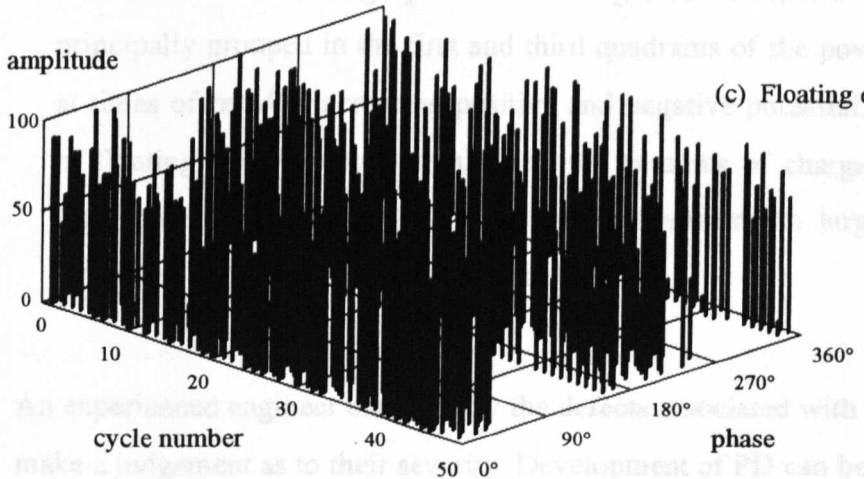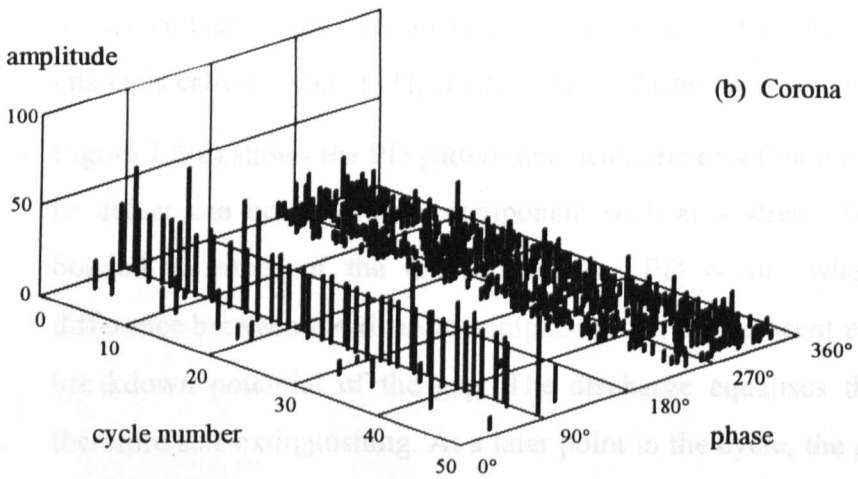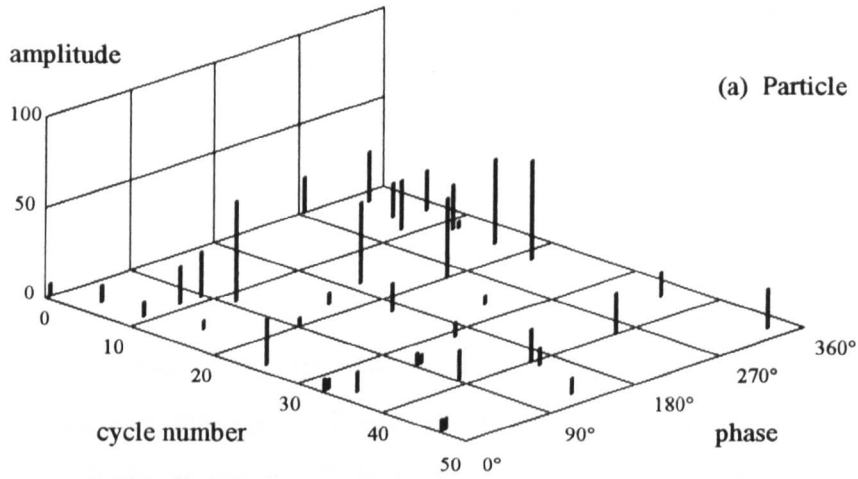
Figure 1.2 Three-dimensional displays of PD pulses from typical defects in GIS.
The cycle number and phase axes refer to the HV power frequency
signal. (a) A conducting particle, (b) a protrusion on the busbar, and
(c) a floating component.

between particle 'lift off' and 'fall down'. Longer periods between successive bounces can indicate that the particle is in flight for a sufficient time to reach the inner conductor [32], at which point breakdown might occur.

- Figure 1.2(b) shows the discharge pattern for a protrusion on the GIS busbar. A large number of pulses occur in the negative half cycle, when the electron required to initiate the PD is readily liberated from the tip of the metallic protrusion. The larger pulses in the positive half cycle are due to the formation of positive streamers. These are fewer in number and have a higher inception voltage, as the initial electron must now be supplied by ionisation of the SF_6. At higher voltages, these streamers are replaced by highly conducting hot ionisation channels called leaders [33], at which point flashover is imminent.

- Figure 1.2(c) shows the PD pattern characteristic of a floating electrode. This type of defect can occur when a component such as a stress shield is not properly bonded to either of the GIS conductors. PD occurs whenever the potential difference between the floating component and the adjacent electrode exceeds the breakdown potential of the gap. The discharge equalises the potentials and is therefore self-extinguishing. At a later point in the cycle, the gap will again break down, and the discharge pulses will be generated repetitively. The pulses are principally grouped in the first and third quadrants of the power frequency cycle, at times of rapidly increasing positive and negative potential. As the capacitance of floating components is significant, the amounts of charge involved are quite high, and floating components typically generate much larger PD signals than those associated with other types of defect.

An experienced engineer can identify the defects associated with the PD patterns and make a judgement as to their severity. Development of PD can be a slow process and is by no means certain to end in breakdown of the GIS. Protrusions may eventually be worn away by the continuing action of discharge at the tip. Particles often bounce into low field regions, such as particle traps, where they are no longer a hazard. The vast amount of data produced by a monitoring system must be stored and presented

in a convenient manner. For this reason, considerable effort is being devoted to the study of the statistical properties of PD [34,35,36]. The knowledge gained is being used to develop expert systems that will process this data [37,38,39] and identify the significant traits of PD caused by the various types of defect.

1.4 Research Objectives

1.4.1 Aspects of the UHF technique requiring investigation

Although the UHF method of PD detection is well established, fundamental principles of the excitation of UHF signals by PD have not been investigated. Consequently, it has been unclear how the UHF signals relate to conventional PD measurements, or what calibrated information can be expected from a UHF system. Various experiments have been carried out to assess the sensitivity of the UHF technique and improve signal interpretation [2,18,32,33,40], but these are no substitute for an understanding of the underlying theory. One approach to this problem has been to measure the variations in UHF signal amplitude using a simulated PD source [41]. Certain relationships between the PD current and the UHF signal are thereby revealed but this method does not explain the effect of the source and coupler locations on the UHF signal. Also, the technique used in [41] to simulate PD on a protrusion does not permit an equivalent charge magnitude to be assigned to the PD.

The following questions summarise the areas of particular interest which formed the basis of this research:

- How does PD excite the UHF signal, and can this signal be defined in terms of useful parameters of the discharge at the defect?

- Are there any limitations to the use of the UHF technique, such as types of PD that cannot be detected?

- Can information about the PD be extracted from the UHF signal, and how much of a UHF PD detection system can be calibrated to define its sensitivity?

1.4.2 Summary of the experimental and theoretical approach

This research is directed towards the development of a fundamental theory explaining how PD excites UHF signals within the coaxial GIS chambers. The basis of this theory is the use of dyadic Green's function techniques to describe the excitation of electromagnetic fields by a current source in a waveguide. The chamber sizes used in the experiments are chosen to be typical of 400kV GIS, as this is the rating to which UHF PD monitoring is most commonly applied. Experimental results are compared with the results of computer simulations based on the theoretical model. This demonstrates that the UHF signal can be predicted using a mathematical expression for the complete transfer function relating the coupler output voltage to the PD current at the defect.

Initial experiments were carried out in a hollow cylindrical chamber with the aim of assessing the accuracy of this approach in a relatively simple configuration. An analytical time-domain solution was sought, at the expense of a number of approximations that resulted in a somewhat idealistic model. However, the level of agreement between simulation and experiment was sufficient to validate the theoretical work. Subsequent work on the coaxial configuration benefited from the experience gained during the study of the hollow chamber. Analysis of PD signals in the coaxial chamber was combined with a more rigorous modelling of the measurement equipment. A numerical approach making use of FFT processing led to much better agreement between the measured and simulated UHF signals, despite the more complex mathematical functions involved in the coaxial analysis. Having experimentally verified the simulation technique in a variety of test configurations, it

was then used to model the effect of changing parameters at the PD source that cannot be controlled experimentally. The model represents a powerful tool for assessing the capabilities of the UHF technique.

A test rig comprising a 3.6m length of aluminium tube of internal diameter 0.5m was used in the experimental work (Figure 1.3). To measure the shape of current pulses from a real PD source, a special test cell was designed. This allows a PD current pulse to be recorded and compared with the specific UHF signal excited in the test rig by that pulse. A pulse injection procedure for simulating a calibrated PD on a short protrusion was also developed.

In Chapter 2, theory relating to the excitation of signals in waveguides is developed into a form suitable for modelling PD signals. In Chapter 3 the test equipment is described and measurements of PD current pulses are presented. Chapters 4 and 5 respectively describe the analysis and experiments relating to the hollow circular cylindrical and coaxial configurations. In both cases, experimental results are compared with simulated UHF signals. The cylindrical analysis is an important step in the development of the coaxial model, rather than an end in itself. For this reason, the cylindrical analysis is presented in its original form, rather than revising it to include the improvements incorporated into the coaxial analysis. In Chapter 6, the model is used to study the effects which changing parameters of the PD source have on the UHF signal that is excited in a GIS. The significance of this research is discussed in Chapter 7, which draws conclusions relevant to PD detection using the UHF technique and suggests topics for further investigation.
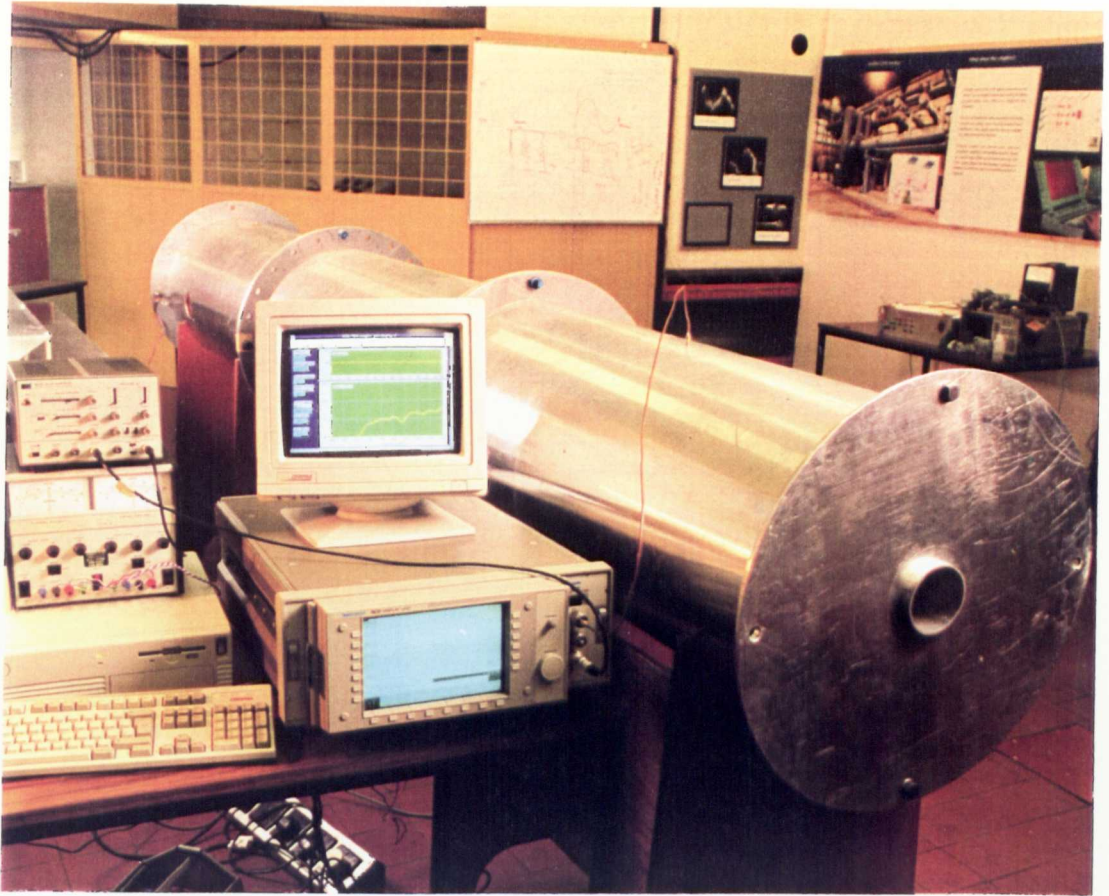
Figure 1.3 A typical configuration of the test equipment. The cylindrical test
chamber was fabricated in three sections, each of length 1.2m.
An electric field probe inserted through the wall of the chamber
is shown connected to the SCD1000 transient digitiser.

2. THEORY OF SIGNAL EXCITATION

2.1 Introduction

General acceptance of the UHF technique has primarily been inhibited by a lack of understanding of the transfer functions involved in the UHF detection of PD in GIS. Three stages of energy transfer can be identified, as illustrated in Figure 2.1, and these are:

      1. *Excitation* of the UHF signal by a PD.

      2. *Propagation* of UHF signals within the GIS.

      3. *Extraction* of UHF signals from the GIS using a coupler.

The purpose of this work is to demonstrate how these three transfer functions can be determined.

A PD normally occupies only a small fraction of the distance between the GIS conductors. The current that flows during the discharge alters the distribution of charge in the region of the defect, but does not flow directly between the two conductors. The PD current follows a path that can include a conducting particle or protrusion, as well as the ionised SF_6 gas. The direction of current flow will tend to follow the lines of the HV electric field, which is predominantly radial within a GIS. Determination of the fields radiated by a current source is a common requirement in high frequency electromagnetic theory, and the first step is to identify an approach suitable for the boundary conditions present in GIS.

Radiation from a current element in free space is quite easily determined. However, the application of boundary conditions from first principles would neglect some powerful techniques that have been developed for various classes of boundary conditions, particularly by Tai [42]. At the other extreme, the excitation of closed cavities is too restrictive for the geometry of GIS, as it requires the imposition of

EXTRACTION

PROPAGATION

EXCITATION

PD
SOURCE

GIS
CHAMBER

UHF
COUPLER

Source parameters:
- location of the PD
- length of discharge path
- shape of current pulse

Propagation effects:
- delay
- dispersion
- reflections
- attenuation

Coupling factors:
- UHF field strength
- coupler response
- noise levels
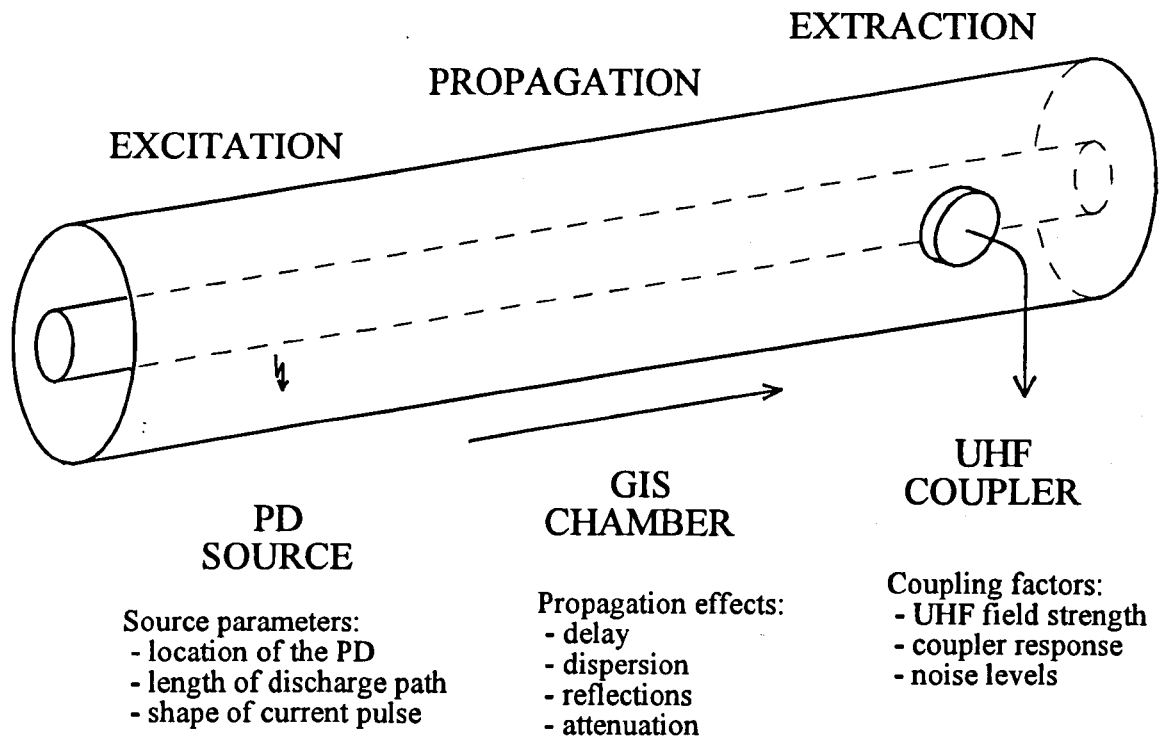
Figure 2.1 Transfer functions involved in the UHF detection of PD in GIS.

boundaries in all spatial co-ordinates. Although a GIS is made up of many chambers, each one is coupled to adjacent chambers by partially reflecting discontinuities in the coaxial transmission lines, such as gas barriers, corners and circuit breakers. The most suitable approach is to use waveguide theory, in which a certain cross-section is defined, with propagation taking place in the direction normal to this plane. There are then no restrictions on the length of chambers, and both total and partially reflecting obstacles can be analysed. The two cross-sections investigated in this work are the coaxial and hollow cylindrical waveguides that are most pertinent to the geometry of GIS.

In modelling the PD as a current source, the terms 'current filament' and 'PD path length' will be introduced. A current filament is defined as a one-dimensional current density, of negligible cross-sectional area compared to the dimensions of the GIS enclosure and flowing in a straight line. The PD path length is then defined as the distance over which this current flows, including the length of any particle, protrusion and ionisation path. The conduction component of the current does not have to be of constant amplitude along this path. Although the theory which is developed can be applied generally, the main concern is with the detection of small defects. These occur in the early stages of insulation degradation and will define the detection threshold required from a PD measurement system. The defects most easily related to this work are metallic protrusions, in which a conduction current pulse $i(t)$ caused by ionisation of gas at the tip flows along the protrusion as shown in Figure 2.2.

inner conductor

SF$_6$ gaseous
         insulation

radial
electric Er
field
lines

outer conductor $i(t)$ ionisation
                            region

                            conducting
                            protrusion
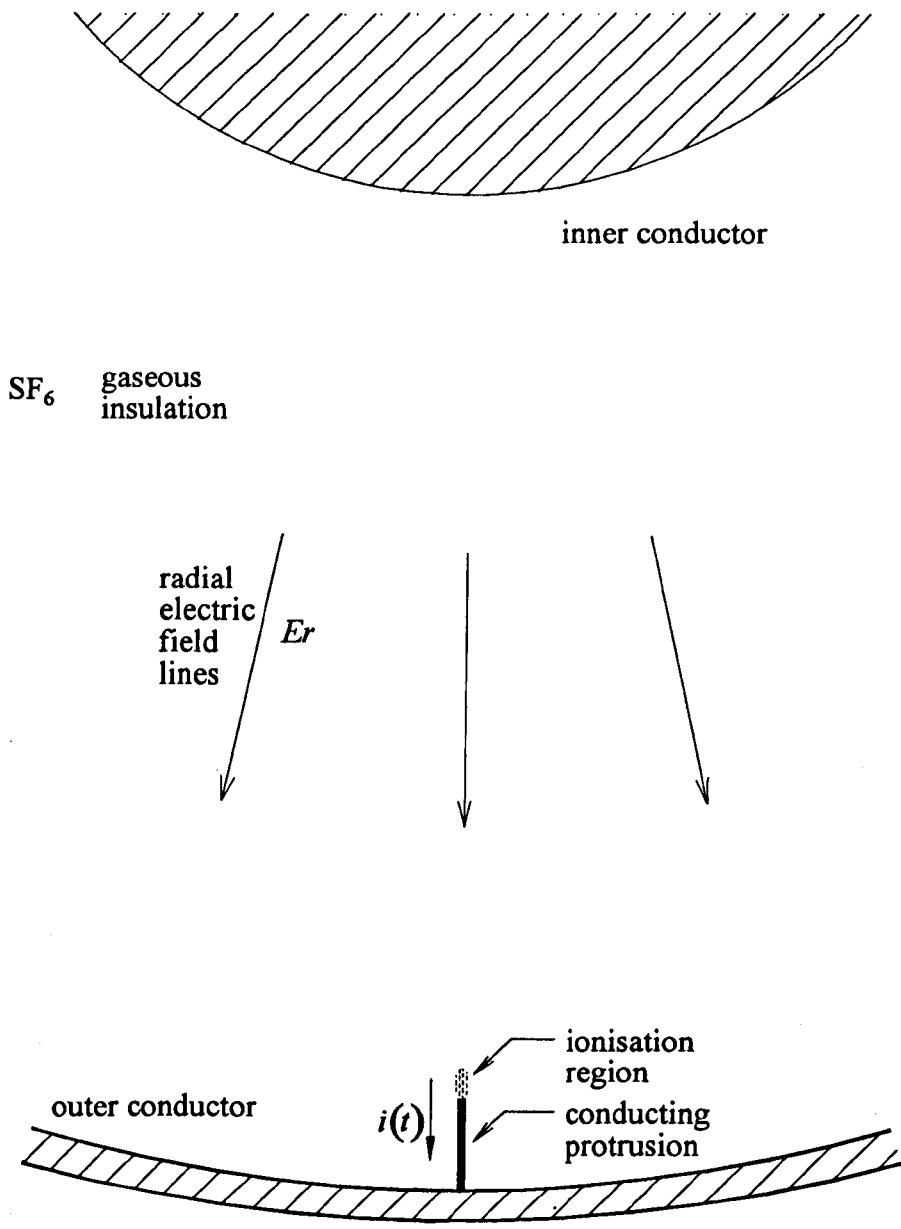
Figure 2.2 Current path for PD at the tip of a protrusion on the outer conductor
            of a GIS.

2.2 Excitation and Propagation of Signals in Waveguides

An electromagnetic field that exists within perfectly conducting boundaries can be expanded in terms of a series of normal modes [43,44], in a manner analogous to the representation of periodic signals by a Fourier series in the time-domain. In a closed cavity, each mode represents a resonant frequency, while in a waveguide each mode has a cut-off frequency below which it does not propagate. In the normal applications of waveguides as transmission lines, analysis is simplified by restricting the frequency content of the signal to a range in which only one mode of propagation occurs. The excitation of waveguides by current sources is described in detail by Collin [43], with the aim of determining the transfer function and input impedance of various antennas for coupling signals to the waveguide. The situation in GIS is novel because the excitation current is not fed from an external source, but derives its energy from the HV field between the conductors. Also, the broad frequency spectrum of a PD pulse, and the highly localised nature of the source result in many modes of propagation being excited. To determine the response at a remote location in the waveguide, it is necessary to include all modes of propagation within the bandwidth of the measurement system.

The familiar mode of propagation in a coaxial transmission line is the transverse electromagnetic (TEM) mode, in which the only non-zero components of the electric and magnetic fields lie in the plane perpendicular to the direction of propagation. However, at sufficiently high frequencies, other modes of propagation become possible [45]. These higher order modes are divided into two categories, transverse electric (TE) and transverse magnetic (TM) types. Each mode has a unique cut-off frequency that is a function of the propagation medium and the waveguide dimensions [45]. Propagation in higher order modes is dispersive, with a single input pulse being transformed into a damped, oscillatory signal [46].

Only the higher order TE and TM modes of propagation exist in a hollow cylindrical waveguide. This configuration was selected to verify the theoretical approach for the following reasons:

1) Only two mode types need to be considered, since the TEM mode is not supported.

2) The theoretical development is more straightforward than that for coaxial waveguide, because only Bessel functions of the first kind are admissible in the vector wave solutions.

3) There has been more attention devoted in the literature to higher order mode theory in hollow waveguides than in coaxial ones because coaxial transmission lines are normally intended for use at frequencies well below the cut-off of higher order modes.

4) The experimental configuration is simplified, and energising the PD test cell is more easily accomplished in a hollow waveguide.

Once the electromagnetic analysis had been successfully applied to the hollow cylindrical waveguide, the more difficult task of developing the coaxial theory could be addressed. The theoretical studies of both configurations are presented in the remainder of this chapter. Experimental results are dealt with separately in Chapters 4 and 5.

2.3 Dyadic Green's Functions for Waveguides

In simple terms, Green's functions relate all possible infinitesimal Dirac type sources to all possible observation positions for a function which is the solution of a differential equation. The Green's function therefore has twice as many dimensions as the solution to the differential equation. Boundary conditions are incorporated in the Green's function, so that the solution for any forcing function can be determined once the appropriate Green's function has been obtained. Consider the displacement

$y(x)$ of a guitar string in response to a Dirac type unit force $\delta(x')$ acting at a distance x' from one end of the string. The Green's function $g(x|x')$ appropriate to the solution would be a function of both the position x at which $y(x)$ was to be observed and of the source position x'. The actual displacement caused by a defined forcing function $f(x')$ can be obtained by integrating the product $g(x|x')f(x')$ over x', since in the limit $f(x')$ can be represented by suitably weighted Dirac functions. The result is a one-dimensional solution giving the particular solution for the displacement $y(x)$. When using Green's functions to solve for an electric field, the 'displacement' becomes the electric field strength at a point in space. For a detailed introduction to this topic and a description of the mathematical concepts, see [47].

A transfer function combining both excitation and propagation of electromagnetic fields in a waveguide can be obtained using dyadic Green's functions. These functions ensure that the proper boundary conditions are satisfied at the waveguide walls. The fields due to an arbitrary excitation current at any location within the waveguide can then be found by solving a volume integral. Dyadic vector functions involve terms such as $\hat{x}\hat{x}$ and $\hat{y}\hat{z}$. These terms are called dyads, and the order of the unit vectors is important, as they relate components of the excitation vector to components of the vector solution. In three-dimensional space there are nine vector dyads. An explanation of dyadic analysis and its application to electromagnetic analysis has been given by Tai [42]. As an introduction to the terminology required in subsequent sections, the basic principles and formulation of the Green's function technique are developed in this section. The development follows the pattern given by Tai [42] and is based on both the first and second editions of the text. Both editions contain typographical errors that can be confusing. It is hoped that these have been eliminated here, and that by concentrating only on the material directly relevant to this work the theory will be more accessible. For proofs of theorems and identities that are quoted, refer to [42].

Maxwell's equations for time harmonic fields in the free space region outside a source with current density $\bar{\mathbf{J}}$ define the interdependence of the electric field $\bar{\mathbf{E}}$ and magnetic field $\bar{\mathbf{H}}$. These equations can be written as:

$$\nabla \times \bar{\mathbf{E}} = j\omega\mu_0\bar{\mathbf{H}} \tag{2.1}$$

$$\nabla \times \bar{\mathbf{H}} = \bar{\mathbf{J}} - j\omega\varepsilon_0\bar{\mathbf{E}} \tag{2.2}$$

Eliminating $\bar{\mathbf{H}}$ between these two equations and substituting $\beta = \omega\sqrt{\mu_0\varepsilon_0}$, we obtain the inhomogeneous vector wave equation,

$$\nabla \times \nabla \times \bar{\mathbf{E}} - \beta^2\bar{\mathbf{E}} = j\omega\mu_0\bar{\mathbf{J}} \tag{2.3}$$

The dyadic Green's technique has been developed with the primary aim of finding solutions to this type of equation, subject to a set of boundary conditions. $\overline{\overline{\mathbf{G}}}(\bar{\mathbf{R}}|\bar{\mathbf{R}}')$ will be used to denote a vector dyadic Green's function which is a solution of the equation

$$\nabla \times \nabla \times \overline{\overline{\mathbf{G}}}(\bar{\mathbf{R}}|\bar{\mathbf{R}}') - \beta^2\overline{\overline{\mathbf{G}}}(\bar{\mathbf{R}}|\bar{\mathbf{R}}') = \bar{\bar{\mathbf{I}}}\delta(\bar{\mathbf{R}} - \bar{\mathbf{R}}') \tag{2.4}$$

where $\bar{\mathbf{R}}$ and $\bar{\mathbf{R}}'$ are position vectors, respectively defining the observation point and source point for the field. The idem dyadic $\bar{\bar{\mathbf{I}}}$ has special properties [42], analogous to those of the unit matrix. Different classes of $\overline{\overline{\mathbf{G}}}$ are distinguished by a subscript according to the type of solution and the boundary conditions that apply. Thus $\overline{\overline{\mathbf{G}}}_{e0}$ designates the Green's function for the electric field in free space that satisfies the radiation condition at infinity, with no other boundaries. In this work, we shall be exclusively concerned with the $\overline{\overline{\mathbf{G}}}_{e1}$ type function that is appropriate to

the electric field of a current source in the presence of a perfectly conducting diffracting body. This situation is illustrated for the general case in Figure 2.3. The choice of electric field for the analysis is based on the requirement to obtain the response of a UHF coupler to an electric field within the waveguide formed by the GIS. However, the derivation of $\overline{\mathbf{E}}$ also defines the magnetic fields through the relationship given in (2.1) and (2.2).

To obtain an expression for $\overline{\mathbf{E}}(\overline{\mathbf{R}})$ in terms of the source current $\overline{\mathbf{J}}$, first let

$$\overline{\mathbf{P}} = \overline{\mathbf{E}}(\overline{\mathbf{R}}) \qquad \text{and} \qquad \overline{\overline{\mathbf{Q}}} = \overline{\overline{\mathbf{G}}}_e\left(\overline{\mathbf{R}}|\overline{\mathbf{R}}'\right) \qquad (2.5)$$

Applying the second vector-dyadic Green's theorem [42] to these two functions through a volume V bounded by a surface S gives

$$\iiint_V \left(\overline{\mathbf{P}} \cdot \nabla \times \nabla \times \overline{\overline{\mathbf{Q}}} - \overline{\overline{\mathbf{Q}}} \cdot \nabla \times \nabla \times \overline{\mathbf{P}}\right) dV = -\oiint_S \hat{\mathbf{n}} \cdot \left[\overline{\mathbf{P}} \times \nabla \times \overline{\overline{\mathbf{Q}}} + \left(\nabla \times \overline{\mathbf{P}}\right) \times \overline{\overline{\mathbf{Q}}}\right] dS$$

$$(2.6)$$

where $\hat{\mathbf{n}}$ is the unit normal outward vector on S. Concentrating firstly on the volume integral, using the shorthand notation $-\oiint_S$ to denote the right-hand side of (2.6) and substituting for $\overline{\mathbf{P}}$ and $\overline{\overline{\mathbf{Q}}}$ from (2.5), we obtain

$$\iiint_V \left[\overline{\mathbf{E}}(\overline{\mathbf{R}}) \cdot \nabla \times \nabla \times \overline{\overline{\mathbf{G}}}_e\left(\overline{\mathbf{R}}|\overline{\mathbf{R}}'\right) - \overline{\overline{\mathbf{G}}}_e\left(\overline{\mathbf{R}}|\overline{\mathbf{R}}'\right) \cdot \nabla \times \nabla \times \overline{\mathbf{E}}(\overline{\mathbf{R}})\right] dV = -\oiint_S \qquad (2.7)$$

26
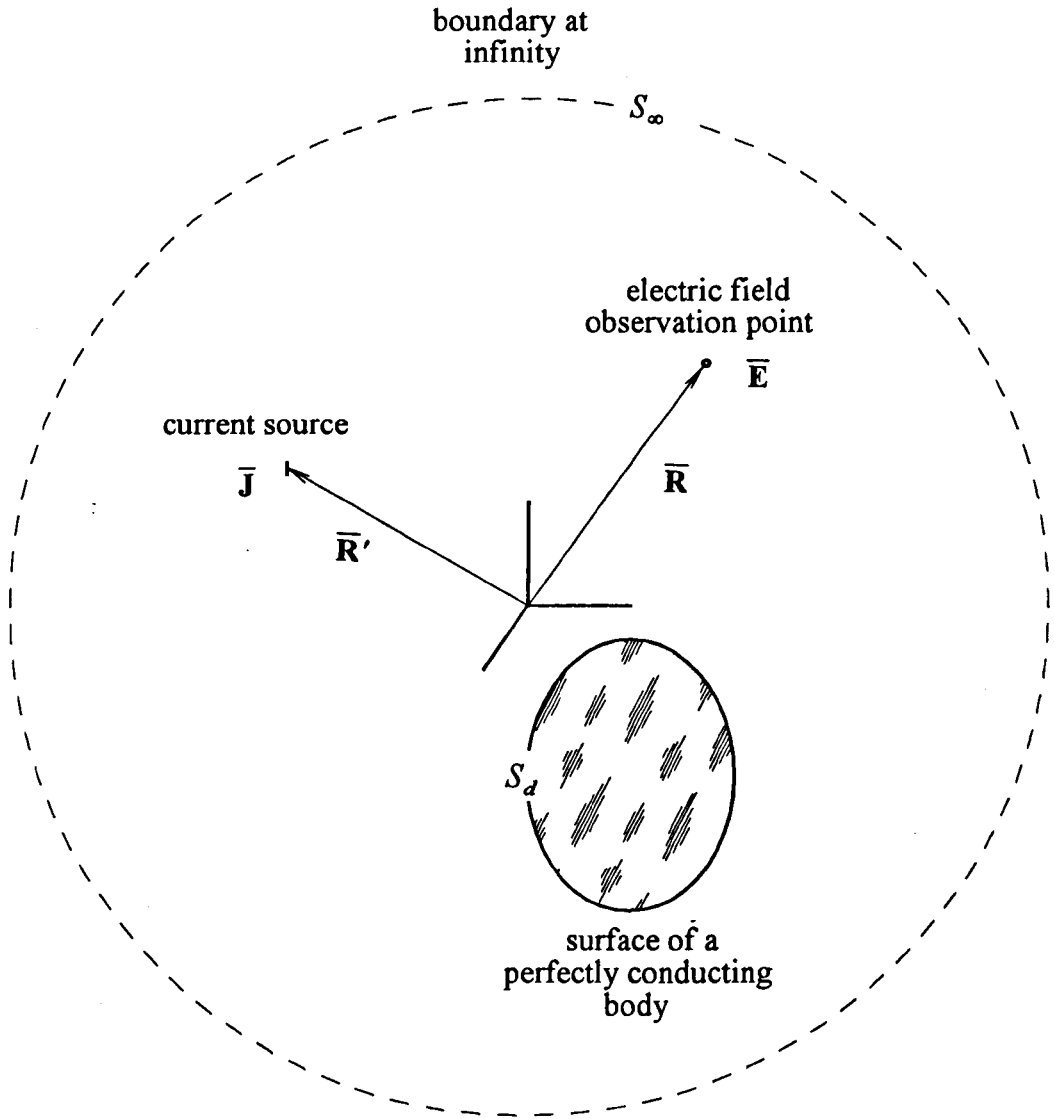
Figure 2.3 Radiation from a current source in the presence of a perfectly conducting scattering body.

Now $\overline{\mathbf{E}}(\overline{\mathbf{R}})$ and $\overline{\overline{\mathbf{G}}}_e(\overline{\mathbf{R}}|\overline{\mathbf{R}}')$ satisfy (2.3) and (2.4) by definition. Using the symmetry property of $\overline{\overline{\mathbf{G}}}_e$ to exchange the primed and unprimed position vectors in the right-hand side of (2.4) and rearranging gives

$$\nabla \times \nabla \times \overline{\mathbf{E}}(\overline{\mathbf{R}}) = j\omega\mu_0\overline{\mathbf{J}}(\overline{\mathbf{R}}') + \beta^2\overline{\mathbf{E}}(\overline{\mathbf{R}}) \tag{2.8}$$

$$\nabla \times \nabla \times \overline{\overline{\mathbf{G}}}_e(\overline{\mathbf{R}}|\overline{\mathbf{R}}') = \overline{\overline{\mathbf{I}}}\delta(\overline{\mathbf{R}}' - \overline{\mathbf{R}}) + \beta^2\overline{\overline{\mathbf{G}}}_e(\overline{\mathbf{R}}|\overline{\mathbf{R}}') \tag{2.9}$$

Substituting (2.8) and (2.9) in (2.7) and gathering terms,

$$\iiint_V \overline{\mathbf{E}}(\overline{\mathbf{R}})\cdot\overline{\overline{\mathbf{I}}}\delta(\overline{\mathbf{R}}' - \overline{\mathbf{R}})dV - \iiint_V \overline{\overline{\mathbf{G}}}_e(\overline{\mathbf{R}}|\overline{\mathbf{R}}')\cdot j\omega\mu_0\overline{\mathbf{J}}(\overline{\mathbf{R}}')dV = -\oiint_S \tag{2.10}$$

Using the properties of the idem dyadic and the Dirac delta function, the first volume integral reduces to

$$\iiint_V \overline{\mathbf{E}}(\overline{\mathbf{R}})\cdot\overline{\overline{\mathbf{I}}}\delta(\overline{\mathbf{R}}' - \overline{\mathbf{R}}) = \overline{\mathbf{E}}(\overline{\mathbf{R}}) \tag{2.11}$$

Rearranging (2.10) using (2.11), (2.6) and applying the vector-dyadic identity $\overline{\mathbf{A}}\cdot(\overline{\mathbf{B}}\times\overline{\overline{\mathbf{C}}}) = (\overline{\mathbf{A}}\times\overline{\mathbf{B}})\cdot\overline{\overline{\mathbf{C}}} = -\overline{\mathbf{B}}\cdot(\overline{\mathbf{A}}\times\overline{\overline{\mathbf{C}}})$ gives

$$\overline{\mathbf{E}}(\overline{\mathbf{R}}) = j\omega\mu_0\iiint_V \overline{\overline{\mathbf{G}}}_e(\overline{\mathbf{R}}|\overline{\mathbf{R}}')\cdot\overline{\mathbf{J}}(\overline{\mathbf{R}}')dV - \oiint_S \left[(\hat{\mathbf{n}}\times\overline{\mathbf{P}})\cdot\nabla\times\overline{\overline{\mathbf{Q}}} - (\nabla\times\overline{\mathbf{P}})\cdot(\hat{\mathbf{n}}\times\overline{\overline{\mathbf{Q}}})\right]dS$$

$$\tag{2.12}$$

Substituting for $\overline{\mathbf{P}}$ and $\overline{\mathbf{Q}}$ from (2.5) and using V' to denote the volume in which the current source $\overline{\mathbf{J}}(\overline{\mathbf{R}}')$ is non-zero, we obtain

$$\overline{\mathbf{E}}(\overline{\mathbf{R}}) = j\omega\mu_0 \iiint\limits_V \overline{\overline{\mathbf{G}}}_e(\overline{\mathbf{R}}|\overline{\mathbf{R}}') \cdot \overline{\mathbf{J}}(\overline{\mathbf{R}}') dV'$$

$$+ \oiint\limits_{S_d, S_\infty} \left\{ [\nabla \times \overline{\mathbf{E}}(\overline{\mathbf{R}})] \cdot \left[\hat{\mathbf{n}} \times \overline{\overline{\mathbf{G}}}_e(\overline{\mathbf{R}}|\overline{\mathbf{R}}') \right] \right\} dS - \oiint\limits_{S_d, S_\infty} \left\{ [\hat{\mathbf{n}} \times \overline{\mathbf{E}}(\overline{\mathbf{R}})] \cdot \left[\nabla \times \overline{\overline{\mathbf{G}}}_e(\overline{\mathbf{R}}|\overline{\mathbf{R}}') \right] \right\} dS$$

$$(2.13)$$

For the surface S_∞, the radiation condition for an electromagnetic field in free space imposes the condition that

$$\lim_{|\overline{\mathbf{R}}| \to \infty} \left\{ \nabla \times \overline{\mathbf{E}}(\overline{\mathbf{R}}) - j\beta\hat{\mathbf{n}} \times \overline{\mathbf{E}}(\overline{\mathbf{R}}) \right\} = 0 \tag{2.14}$$

and $\overline{\overline{\mathbf{G}}}_e$ must also satisfy this condition, so that

$$\lim_{|\overline{\mathbf{R}}| \to \infty} \left\{ \nabla \times \overline{\overline{\mathbf{G}}}_e(\overline{\mathbf{R}}|\overline{\mathbf{R}}') - j\beta\hat{\mathbf{n}} \times \overline{\overline{\mathbf{G}}}_e(\overline{\mathbf{R}}|\overline{\mathbf{R}}') \right\} = 0 \tag{2.15}$$

The surface integrals evaluated on S_∞ in (2.13) therefore approach zero and only the contribution at S_d remains. Since the diffracting body is perfectly conducting, $\hat{\mathbf{n}} \times \overline{\mathbf{E}}(\overline{\mathbf{R}}) = 0$ on S_d. Thus if a function $\overline{\overline{\mathbf{G}}}_{e1}$ can be found such that $\hat{\mathbf{n}} \times \overline{\overline{\mathbf{G}}}_{e1}(\overline{\mathbf{R}}|\overline{\mathbf{R}}') = 0$ on S_d, the entire surface integral in (2.13) vanishes. Such a function is called the *electric dyadic Green's function of the first kind*. In terms of $\overline{\overline{\mathbf{G}}}_{e1}$, the electric field at $\overline{\mathbf{R}}$ due to a current source at $\overline{\mathbf{R}}'$ is given by

$$\overline{\mathbf{E}}(\overline{\mathbf{R}}) = j\omega\mu_0 \iiint\limits_V \overline{\overline{\mathbf{G}}}_{e1}(\overline{\mathbf{R}}|\overline{\mathbf{R}}') \cdot \overline{\mathbf{J}}(\overline{\mathbf{R}}') dV' \tag{2.16}$$

Together with the geometry specific Green's functions given in Sections 2.4 and 2.5, (2.16) provides the starting point for an analysis of the electromagnetic waves excited by PD in the hollow cylindrical and coaxial configurations.

2.4 Hollow Cylindrical Waveguide

Consider an infinite circular waveguide of internal radius a in the cylindrical co-ordinate system having unit vectors $(\hat{r}, \hat{\phi}, \hat{z})$ as shown in Figure 2.4. Let the position at which we require the electric field $\overline{E}$ be defined by the vector

$$\overline{R} = \left(r\hat{r}, \phi\hat{\phi}, z\hat{z} \right) \tag{2.17}$$

and the position of the current source $\overline{J}$ be defined by the vector

$$\overline{R}' = \left(r'\hat{r}, \phi'\hat{\phi}, z'\hat{z} \right) \tag{2.18}$$

Free space properties are assumed for the propagation medium inside the waveguide. Orthogonality proofs for the vector wave functions and the evaluation process for the normalisation integrals are described in [42]. The Green's function for the hollow cylindrical waveguide can be defined in terms of the orthogonal electric field patterns of the TE and TM modes. The full expression for the $\overline{\overline{G}}_{e1}$ type function [42] is

$$\overline{\overline{G}}_{e1}\left(\overline{R} | \overline{R}' \right) = -\frac{1}{\beta_0^2} \hat{z}\hat{z}\delta\left(\overline{R} - \overline{R}' \right)$$

$$+ \sum_{n,m} \left\{ c_u \left[\overline{M}_{nm}^e\left(\overline{R}, \pm\beta_u \right) \overline{M}_{nm}^e\left(\overline{R}', \mp\beta_u \right) + \overline{M}_{nm}^o\left(\overline{R}, \pm\beta_u \right) \overline{M}_{nm}^o\left(\overline{R}', \mp\beta_u \right) \right] \right.$$

$$\left. + c_v \left[\overline{N}_{nm}^e\left(\overline{R}, \pm\beta_v \right) \overline{N}_{nm}^e\left(\overline{R}', \mp\beta_v \right) + \overline{N}_{nm}^o\left(\overline{R}, \pm\beta_v \right) \overline{N}_{nm}^o\left(\overline{R}', \mp\beta_v \right) \right] \right\}, \quad z \gtrless z'$$
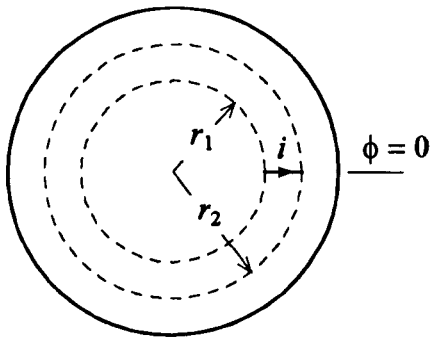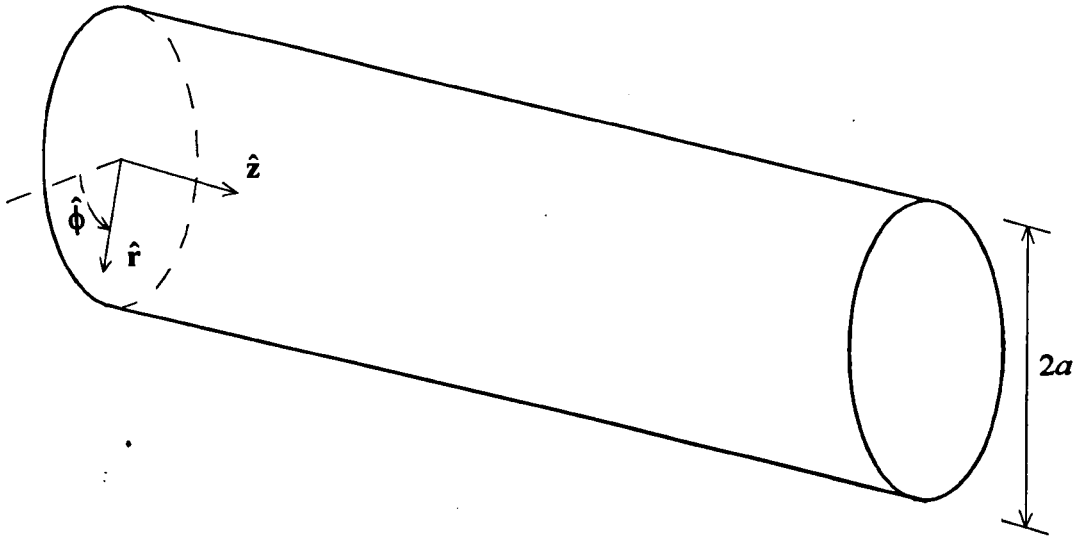
$$\tag{2.19}$$

Transverse plane containing the current source, located at $z' = 0$.
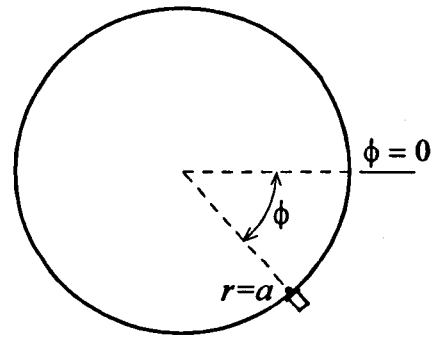
Transverse plane containing the UHF coupler, at a distance z from the plane of the current source.

Figure 2.4 Co-ordinate system for the infinite circular cylindrical waveguide, showing the current source and the electric field observation position.

The remainder of this section will be concerned with defining the terms involved in (2.19) and simplifying this expression to a useful form that relates directly to the particular problem with which we are concerned. The vector wave functions satisfying the Dirichlet boundary condition at $r = a$ are [42]:

$$\overline{M}_{nm}^{e}\left(\overline{R}, \beta_u\right) = \nabla \times \left[J_n(ur)\cos(n\phi) e^{j\beta_u z} \, \hat{z} \right] \qquad (2.20)$$

$$\overline{M}_{nm}^{o}\left(\overline{R}, \beta_u\right) = \nabla \times \left[J_n(ur)\sin(n\phi) e^{j\beta_u z} \, \hat{z} \right] \qquad (2.21)$$

$$\overline{N}_{nm}^{e}\left(\overline{R}, \beta_v\right) = \frac{1}{\beta_0} \nabla \times \nabla \times \left[J_n(vr)\cos(n\phi) e^{j\beta_v z} \, \hat{z} \right] \qquad (2.22)$$

$$\overline{N}_{nm}^{o}\left(\overline{R}, \beta_v\right) = \frac{1}{\beta_0} \nabla \times \nabla \times \left[J_n(vr)\sin(n\phi) e^{j\beta_v z} \, \hat{z} \right] \qquad (2.23)$$

The eigenvalues that ensure the boundary conditions are satisfied by these equations are

$$u = q_{nm}/a \qquad (2.24)$$

$$v = p_{nm}/a \qquad (2.25)$$

where

$$q_{nm} \text{ is the } m\text{th root of } J'_n(q) = 0 \qquad (2.26)$$

and

$$p_{nm} \text{ is the } m\text{th root of } J_n(p) = 0 \qquad (2.27)$$

The integers n and m identify the mode numbers according to the particular eigenvalue by which they are generated [45]. Note that the double subscript nm is implied for the eigenvalues u and v to improve legibility of the equations. The functions $\overline{M}$ describe the electric field of the TE$_{nm}$ modes and the $\overline{N}$ functions

describe the electric field of the TM_{nm} modes. β_u and β_v are the propagation constants for TE and TM modes respectively, given by

$$\beta_u = \sqrt{\beta_0^2 - u^2} \qquad (2.28)$$

and

$$\beta_v = \sqrt{\beta_0^2 - v^2} \qquad (2.29)$$

The sine and cosine terms in (2.20) - (2.23) are required to represent a completely general field, which is the reason for the even and odd mode designation using the superscripts e and o. The expression within the square brackets in (2.20) - (2.23) is called the *generating function*, and the designation of a mode as even or odd is based on its generating function. Following the differentiation steps invoked by the curl operator, the vector wave functions can be written as

$$\overline{\mathbf{M}}_{nm}^{e}\left(\overline{\mathbf{R}}, \beta_u\right) = \left[-\frac{n J_n(ur)}{r} \sin(n\phi)\, \hat{\mathbf{r}} - u J_n'(ur) \cos(n\phi)\, \hat{\boldsymbol{\phi}} \right] e^{j\beta_u z} \qquad (2.30)$$

$$\overline{\mathbf{M}}_{nm}^{o}\left(\overline{\mathbf{R}}, \beta_u\right) = \left[\frac{n J_n(ur)}{r} \cos(n\phi)\, \hat{\mathbf{r}} - u J_n'(ur) \sin(n\phi)\, \hat{\boldsymbol{\phi}} \right] e^{j\beta_u z} \qquad (2.31)$$

$$\overline{\mathbf{N}}_{nm}^{e}\left(\overline{\mathbf{R}}, \beta_v\right) =$$

$$\frac{1}{\beta_0}\left[jv\beta_v J_n'(vr)\cos(n\phi)\, \hat{\mathbf{r}} - \frac{jn\beta_v}{r} J_n(vr)\sin(n\phi)\, \hat{\boldsymbol{\phi}} + v^2 J_n(vr)\cos(n\phi)\, \hat{\mathbf{z}} \right] e^{j\beta_v z}$$

$$(2.32)$$

$$\overline{\mathbf{N}}_{nm}^{o}\left(\overline{\mathbf{R}}, \beta_v\right) =$$

$$\frac{1}{\beta_0}\left[jv\beta_v J_n'(vr)\sin(n\phi)\, \hat{\mathbf{r}} + \frac{jn\beta_v}{r} J_n(vr)\cos(n\phi)\, \hat{\boldsymbol{\phi}} + v^2 J_n(vr)\sin(n\phi)\, \hat{\mathbf{z}} \right] e^{j\beta_v z}$$

$$(2.33)$$

Note that in differentiating the Bessel functions, notation of the form $aJ_n'(ax)$ has been used for $\frac{\partial}{\partial x}J_n(ax)$. Substitution of the eigenvalues u and v into (2.30) - (2.33) for $r = a$ shows that the boundary condition at the waveguide wall is satisfied. For example, by definition $J_n(va) = J_n(p_{nm}) = 0$, so that the tangential components of the $\overline{N}$ functions (terms in $\hat{\phi}$ and $\hat{z}$) vanish. Only the radial component is non-zero at the surface of the waveguide wall. By inspection, the same condition is met by the $\overline{M}$ functions, since $J_n'(ua) = 0$.

The coefficients c_u and c_v in (2.19) are given by

$$c_u = \frac{j(2 - \delta_0^n)}{2\pi\beta_u(u^2a^2 - n^2)J_n^2(ua)} \qquad (2.34)$$

$$c_v = \frac{j(2 - \delta_0^n)}{2\pi a^2 v^2 \beta_v [J_n'(va)]^2} \qquad (2.35)$$

To reduce the complexity of the completely general expression for $\overline{\overline{G}}_{e1}$ given in (2.19), we consider the contribution of a particular mode and obtain the Green's function appropriate to its excitation. Let us also choose the relative positions of the source and observer so that propagation is in the positive z-direction, $(z > z')$. The observation position is defined to lie outside the source region, so that the first term in (2.19) can be omitted, since $\delta(\overline{R} - \overline{R}') = 0$ in this case. Selecting the term involving the TE_{nm} field and using the odd $\overline{M}$ functions, (2.19) reduces to

$$\overline{\overline{G}}_{TEnm}(\overline{R}|\overline{R}') = c_u\overline{M}_{nm}^o(\overline{R},\beta_u)\overline{M}_{nm}^o(\overline{R}',-\beta_u) \qquad (2.36)$$

The vector function of the source co-ordinates, $\overline{M}^o_{nm}\left(\overline{R}',-\beta_u\right)$ is obtained by replacing r,ϕ,z and β_u with r',ϕ',z' and $-\beta_u$ respectively. Substituting the expression for $\overline{M}$ from (2.31) in (2.36) yields the following four term dyadic:

$$\overline{\overline{G}}_{TEnm}\left(\overline{R}\big|\overline{R}'\right)=$$

$$c_u\left[\frac{n^2 J_n\left(ur\right)J_n\left(ur'\right)}{rr'}cos\left(n\phi\right)cos\left(n\phi'\right)\hat{r}\hat{r} - \frac{nJ_n\left(ur\right)uJ'_n\left(ur'\right)}{r}cos\left(n\phi\right)sin\left(n\phi'\right)\hat{r}\hat{\phi}\right.$$

$$\left.- \frac{nJ_n\left(ur'\right)uJ'_n\left(ur\right)}{r'}sin\left(n\phi\right)cos\left(n\phi'\right)\hat{\phi}\hat{r} + u^2 J'_n\left(ur\right)J_n\left(ur'\right)sin\left(n\phi\right)sin\left(n\phi'\right)\hat{\phi}\hat{\phi}\right]e^{-j\beta_u\left(z'-z\right)}$$

(2.37)

The term containing the dyad $\hat{r}\hat{r}$ relates the radial component of electric field to the radial component of the current source. The dyadic term in $\hat{r}\hat{\phi}$ relates the $\hat{r}$ component of electric field to the $\hat{\phi}$ component of current, etc. There are no terms involving $\hat{z}$ in (2.37), since by definition the TE modes have no component of electric field in the direction of propagation.

Some practical considerations are now appropriate to further simplify (2.37) by identifying the most important term. UHF couplers are normally mounted close to the outer conductor of a GIS, so that the risk of flashover due to electric field enhancement is not increased. We have seen that only the radial electric field exists at the outer conductor, so this will be the most significant component affecting the coupler response. We also note that the predominant component of a PD current will also be radial, following the direction of the applied HV field. Therefore, we are mainly concerned with radial currents exciting radial fields and the analysis will be restricted to developing $\hat{r}\hat{r}$ term relating these components. However, the method that is used could equally be applied to any other orientation of source and coupler, if required. Note that for TM modes, the product of the vector functions for the

35

electric field leads to nine dyadic terms in the Green's function. A total of 26 terms would therefore be required for a completely general solution when both even and odd mode types are included.

The reason for choosing the odd functions $\overline{\mathbf{M}}$ to obtain (2.37) can now be explained. If the current source is restricted to a radial direction, then ϕ' is constant for all points on the current source. We can therefore choose the arbitrary plane $(\phi' = 0, z' = 0)$ to coincide with the source. Having made this choice, the radiated fields can be fully represented using only the electric field patterns having a radial component that varies with $cos(n\phi)$, and these are the odd $\overline{\mathbf{M}}$ functions (2.31) and the even $\overline{\mathbf{N}}$ functions (2.32). To determine the radial TE$_{nm}$ electric field at the outer conductor $(r = a)$, a distance z along the waveguide from a radial current source in the plane $(\phi' = 0, z' = 0)$, (2.37) simplifies to

$$\overline{\overline{\mathbf{G}}}_{TEnm}\left(a,\phi,z\,\middle|\,r',0,0\right) = \frac{j\left(2 - \delta_0^n\right)n^2}{2\pi a\left(q_{nm}^2 - n^2\right)J_n\left(q_{nm}\right)} \frac{J_n\left(q_{nm}r'/a\right)}{r'} cos(n\phi) \frac{e^{j\beta_u z}}{\beta_u}\hat{\mathbf{r}}\hat{\mathbf{r}}$$

(2.38)

where expressions for u and c_u from (2.24) and (2.34) have been used. The corresponding Green's dyadic for the radial TM$_{nm}$ electric field is found using (2.19), (2.25), (2.32) and (2.35), giving

$$\overline{\overline{\mathbf{G}}}_{TMnm}\left(a,\phi,z\,\middle|\,r',0,0\right) = \frac{j\left(2 - \delta_0^n\right)}{2\pi a^2 J_n'\left(p_{nm}\right)} J_n'\left(p_{nm}r'/a\right)cos(n\phi)\frac{\beta_v e^{j\beta_v z}}{\beta_0^2}\hat{\mathbf{r}}\hat{\mathbf{r}}$$ (2.39)

The next step is to define the current source density $\overline{\mathbf{J}}$ in a form suitable for use in (2.16) so that the electric field can be determined. Let the path of the PD current source be from $r' = r_1$ to $r' = r_2$ in the plane $\phi' = 0, z' = 0$ as shown in Figure 2.4.

36

If the diameter of the current filament is negligible compared with the waveguide dimensions, the conduction current density function can be written as:

$$\overline{J}(\overline{R}') = \delta(\phi')\delta(z')\big[U(r'-r_1)-U(r'-r_2)\big]I(\omega)\hat{r} \qquad (2.40)$$

where $\delta(x)$ is the Dirac impulse function, $U(x)$ is the Heaviside step function and $I(\omega)$ is the frequency-domain representation of the current pulse $i(t)$. Equation (2.16) is now evaluated to obtain the radial electric field Er at the coupler position $\overline{R} = (a,\phi,z)$ as shown in Figure 2.4. For TE modes, using (2.38),

$$Er_{TEnm}(a,\phi,z) = j\omega\mu_0 \int\limits_{-\infty}^{\infty} \int\limits_{-\pi}^{\pi} \int\limits_{0}^{a} \left\{ \frac{j\big(2-\delta_0^n\big)n^2}{2\pi a\big(q_{nm}^2-n^2\big)J_n\big(q_{nm}\big)} \frac{J_n\big(q_{nm}r'/a\big)}{r'} cos(n\phi)\frac{e^{j\beta_u z}}{\beta_u} \right.$$

$$\times \left. \delta(\phi')\delta(z')\big[U(r'-r_1)-U(r'-r_2)\big]I(\omega) \right\} dr'\, d\phi'\, dz'$$

$$(2.41)$$

The integrals in the ϕ' and z' co-ordinates are trivial, due to properties of the Dirac functions, and (2.41) simplifies to

$$Er_{TEnm}(a,\phi,z) = -\frac{\omega\mu_0\big(2-\delta_0^n\big)n^2}{2\pi a\big(q_{nm}^2-n^2\big)J_n\big(q_{nm}\big)}cos(n\phi)\frac{e^{j\beta_u z}}{\beta_u}I(\omega)\int\limits_{r_1}^{r_2}\frac{J_n\big(q_{nm}r'/a\big)}{r'}dr'$$

$$(2.42)$$

Implicit in (2.42) is the condition that the excitation current $i(t)$ is constant over the length of the current filament at any instant in time. When $i(t)$ varies over (r_1,r_2) as $i(t,r')$, a term of the form $I(\omega,r')$ should be taken inside the integral in (2.42).

Making the substitutions $\beta_0 = 2\pi/\lambda_0$ and $u = 2\pi/\lambda_{nm}$ in (2.28), where λ_0 is the free space wavelength and λ_{nm} is the cut-off wavelength for the TE_{nm} mode in the waveguide, (2.28) can be written as

$$\beta_u = \frac{1}{c}\sqrt{\omega^2 - \omega_{nm}^2} \qquad (2.43)$$

where ω_{nm} is the radian cut-off frequency of the TE_{nm} mode, related to the corresponding eigenvalue by

$$\omega_{nm} = cu \qquad (2.44)$$

Rearranging (2.42) and gathering terms, we can express the radial electric field as

$$Er_{TEnm} = K_{TEnm} \int_{r_1}^{r_2} \frac{J_n(q_{nm}r'/a)}{r'} dr' \cos(n\phi) I(\omega) F_{TEnm}(\omega) \qquad (2.45)$$

where K_{TEnm} is a constant dependent on the waveguide dimensions and mode numbers,

$$K_{TEnm} = \frac{n^2 Z_0 \left(2 - \delta_0^n\right)}{2\pi a J_n(q_{nm})\left(q_{nm}^2 - n^2\right)} \qquad (2.46)$$

and the frequency dependent effects of propagation in the z-direction are contained in the function

$$F_{TEnm}(\omega) = \frac{-\omega}{\sqrt{\omega^2 - \omega_{nm}^2}} e^{j\frac{z}{c}\sqrt{\omega^2 - \omega_{nm}^2}} \qquad (2.47)$$

The free space impedance $Z_0 = 377\Omega$ appears in (2.46) from the relationship $Z_0 = \mu_0 c$. The cut-off frequencies ω_{nm} are given by

$$\omega_{nm} = cq_{nm}/a \qquad (TE\ modes) \qquad (2.48)$$

Following a similar development for the TM modes, using (2.19), (2.29), (2.39) and (2.40), we arrive at the analogous expressions

$$Er_{TMnm} = K_{TMnm} \left[J_n(p_{nm}r_2/a) - J_n(p_{nm}r_1/a) \right] cos(n\phi) I(\omega) F_{TMnm}(\omega)$$

(2.49)

where

$$K_{TMnm} = \frac{Z_0 \left(2 - \delta_0^n\right)}{2\pi a \, J_n'(p_{nm}) p_{nm}}$$

(2.50)

$$F_{TMnm}(\omega) = \frac{-\sqrt{\omega^2 - \omega_{nm}^2}}{\omega} e^{j\frac{z}{c}\sqrt{\omega^2 - \omega_{nm}^2}}$$

(2.51)

and

$$\omega_{nm} = c \, p_{nm}/a \qquad (TM\ modes)$$

(2.52)

2.5 Coaxial Waveguide

The Green's functions appropriate to coaxial waveguide were derived from results given by Freeman [48,49]. Although Green's functions are not explicitly mentioned, expansion of the electric field excited by a current source is given in terms of the normal waveguide modes. By comparing these expressions with (2.19), the Green's functions can be deduced. A careful comparison of Freeman's equations for the excitation of circular cylindrical waveguide and the expressions obtained in Section 2.4 revealed them to be identical. However, in the coaxial case there are a number of typographical errors in [48] and in Tai's analysis [42]. Freeman's result is the more accessible, as the treatment given by Tai is rather brief . Comparison of the two sets of coaxial equations showed that they were not the same, even after all the obvious mistakes had been corrected. However, the TEM mode electric field derived on the basis of [42] was clearly incorrect, because a dispersive term appeared when only a time delay should be present. Also, the electric field strengths predicted by [42] were an order of magnitude lower than those predicted by [48] and measured during preliminary experiments. Therefore, Freeman's work forms the foundation for the coaxial analysis that follows.

Figure 2.5 shows a coaxial line with an inner conductor of radius a and an outer conductor of radius b. The three classes of propagating modes in a coaxial line will be considered separately and the $\overline{\overline{G}}_{e1}$ type functions for these modes are presented below. The TEM mode is unique, but an infinite number of higher order modes exist, designated by the subscripts TE_{nm} and TM_{nm}.
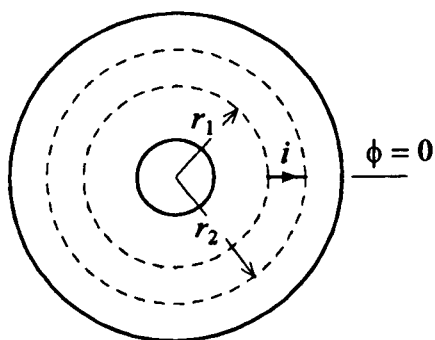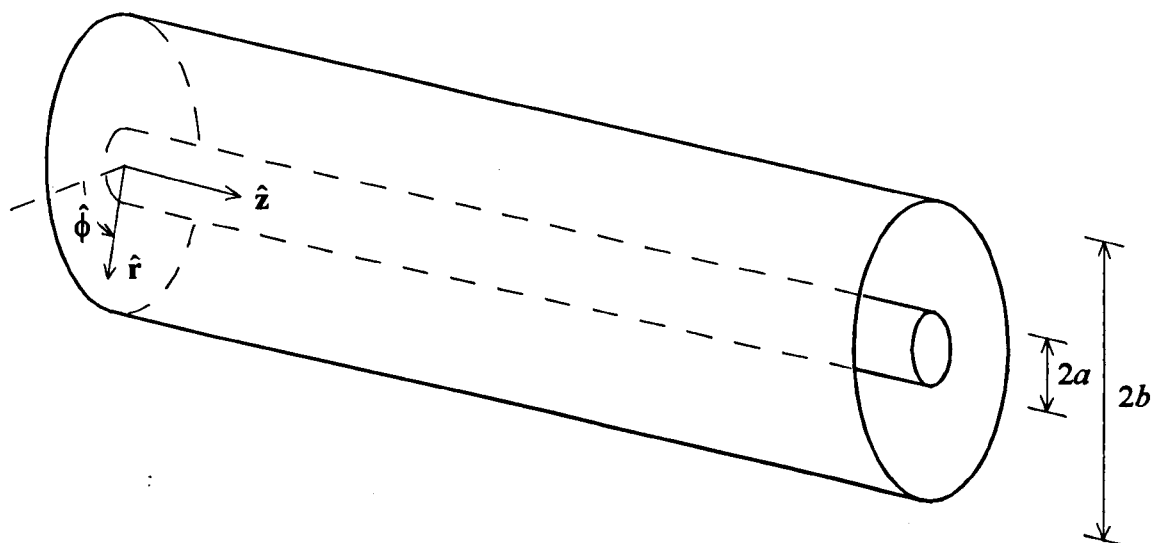
Transverse plane containing the current source, located at $z' = 0$.
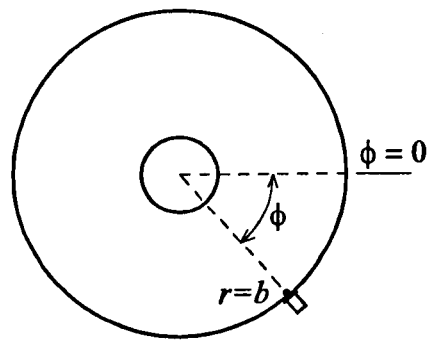
Transverse plane containing the UHF coupler, at a distance z from the plane of the current source.

Figure 2.5 Co-ordinate system for the infinite coaxial waveguide, showing the current source and the electric field observation position.

41

TEM mode:

In this case, the only term that exists is the one relating radial components, because Er is the only non-zero electric field component.

$$\overline{\overline{G}}_{TEM}\left(\mathbf{R}\,|\,\mathbf{R}'\right)= \frac{Z_0}{4\pi\,ln\left(\dfrac{b}{a}\right)}\,\frac{1}{j\omega\mu_0}\,\frac{e^{-j\beta_0\left(z-z'\right)}}{r\,r'}\,\hat{r}\,\hat{r} \qquad (2.53)$$

TE modes:

The general expression is

$$\overline{\overline{G}}_{TE}\left(\overline{R}\,|\,\overline{R}'\right)=$$

$$\frac{j\pi}{8}\sum_{n=0}^{\infty}\sum_{m=1}^{\infty}\frac{\left(2-\delta_0^n\right)J_n'^2(ub)\overline{M}_{nm}\left(\overline{R}'\right)\overline{M}_{nm}\left(\overline{R}\right)}{\left[J_n'^2(ua)\left(1-\dfrac{n^2}{u^2b^2}\right)-J_n'^2(ub)\left(1-\dfrac{n^2}{u^2a^2}\right)\right]\beta_u}\,e^{j\beta_u\left(z-z'\right)}$$

$$(2.54)$$

The $\overline{M}$ functions can be derived from the even or odd mode generating function. For the reasons discussed in Section 2.4, only the odd mode functions are necessary, and these are

$$\overline{M}_{nm}^o\left(\overline{R}\right)=\frac{n}{r}cos(n\phi)\,Z_n(ur)\,\hat{r}-u\,sin(n\phi)\,Z_n'(ur)\,\hat{\phi} \qquad (2.55)$$

where

$$Z_n(ur)=J_n(ur)\,Y_n'(ua)-Y_n(ur)\,J_n'(ua) \qquad (2.56)$$

$$Z_n'(ur)=J_n'(ur)\,Y_n'(ua)-Y_n'(ur)\,J_n'(ua) \qquad (2.57)$$

and

$$\beta_u = \sqrt{\beta_0^2 - u^2}$$ (2.58)

The mode eigenvalue u is the mth root of the equation

$$J_n'(ua) Y_n'(ub) - Y_n'(ua) J_n'(ub) = 0$$ (2.59)

which ensures that the tangential electric field components of the TE mode function $\overline{M}$ vanish at the surfaces of both conductors $(r = a, r = b)$.

TM modes:

The general expression is

$$\overline{\overline{G}}_{TM}(\overline{R}|\overline{R}') = \frac{j\pi}{8\beta_0^2} \sum_{n=0}^{\infty} \sum_{m=1}^{\infty} \frac{(2-\delta_0^n) v^2 J_n^2(vb)}{J_n^2(va) - J_n^2(vb)} \left[\frac{\beta_v}{v^2} \overline{N}_{nm}(\overline{R}') \overline{N}_{nm}(\overline{R}) \right.$$

$$\left. + j\overline{N}_{nm}(\overline{R}') \overline{P}_{nm}(\overline{R}) - j\overline{P}_{nm}(\overline{R}') \overline{N}_{nm}(\overline{R}) + \frac{v^2}{\beta_v} \overline{P}_{nm}(\overline{R}') \overline{P}_{nm}(\overline{R}) \right] e^{j\beta_v(z-z')}$$

(2.60)

where only the even mode generating functions will be included,

$$\overline{N}_{nm}^e(\overline{R}) = -v\cos(n\phi) X_n'(vr)\hat{r} + \frac{n}{r}\sin(n\phi) X_n(vr)\hat{\phi}$$ (2.61)

$$\overline{P}_{nm}^e(\overline{R}) = \cos(n\phi) X_n(vr)\hat{z}$$ (2.62)

where

$$X_n(vr) = J_n(vr) Y_n(va) - Y_n(vr) J_n(va) \qquad (2.63)$$

$$X_n'(vr) = J_n'(vr) Y_n(va) - Y_n'(vr) J_n(va) \qquad (2.64)$$

and

$$\beta_v = \sqrt{\beta_0^2 - v^2} \qquad (2.65)$$

The mode eigenvalue v is the mth root of the equation

$$J_n(va) Y_n(vb) - Y_n(va) J_n(vb) = 0 \qquad (2.66)$$

which ensures that the tangential electric field components of the TM mode function $\overline{N}$ vanish at both conductor surfaces.

The relationship between the radial components of PD current and the electric field can now be determined by following the procedure used in Section 2.4. First the Green's functions are reduced to the single term involving $\hat{r}\hat{r}$. If the path of the PD current source is from $r' = r_1$ to $r' = r_2$ in the plane $(\phi' = 0, z' = 0)$, as shown in Figure 2.5, the current density function given in (2.40) can again be used. Equation (2.19) can then be evaluated to determine Er at the outer conductor $\overline{R} = (b, \phi, z)$ due to a current source at $\overline{R}' = (r', 0, 0)$.

TEM mode:

No simplification of the Green's dyadic is required in this case, as only the $\hat{r}\,\hat{r}$ coupling term exists. Substituting (2.53) and (2.40) in (2.19) gives

$$Er_{TEM}(b,\phi,z) = j\omega\mu_0 \int_{r'=a}^{b} \int_{\phi'=-\pi}^{+\pi} \int_{z'=-\infty}^{+\infty} \frac{Z_0}{4\pi j\omega\mu_0 \, ln(b/a)} \frac{e^{-j\beta_0(z-z')}}{b\,r'}$$

$$\times \, \delta(\phi')\delta(z')\big[U(r'-r_1)-U(r'-r_2)\big]I(\omega)\hat{r}\,dz'\,d\phi'\,dr'$$

(2.67)

which simplifies to

$$Er_{TEM} = \frac{Z_0}{4\pi b\,ln(b/a)}\,ln\!\left(\frac{r_2}{r_1}\right)I(\omega)\,e^{-j\omega z/c}$$

(2.68)

TE modes:

The term in $\hat{r}\,\hat{r}$ for the TE_{nm} mode in (2.54) is

$$\overline{\overline{G}}_{TEnm}\big(b,\phi,z\mid r',0,0\big)=$$

$$\frac{j\pi n^2}{8b}\;\frac{\big(2-\delta_0^n\big)J_n'^2(ub)Z_n(ub)\cos(n\phi)}{J_n'^2(ua)\!\left(1-\dfrac{n^2}{u^2 b^2}\right)-J_n'^2(ub)\!\left(1-\dfrac{n^2}{u^2 a^2}\right)}\;\frac{Z_n(ur')}{r'}\,\frac{e^{j\beta_u z}}{\beta_u}\,\hat{r}\,\hat{r}$$

(2.69)

Substituting (2.69) and (2.40) in (2.19) gives the radial electric field,

$$Er_{TEnm} =$$

$$\frac{-\omega\mu_0\pi n^2}{8b} \frac{\left(2-\delta_0^n\right)J_n'^2(ub)Z_n(ub)\cos(n\phi)I(\omega)}{J_n'^2(ua)\left(1-\dfrac{n^2}{u^2b^2}\right)-J_n'^2(ub)\left(1-\dfrac{n^2}{u^2a^2}\right)} \frac{e^{j\beta_u z}}{\beta_u}\int_{\eta}^{r_2}\frac{Z_n(ur')}{r'}dr'$$

$$(2.70)$$

and substituting for β_u from (2.43) yields

$$Er_{TEnm} = K_{TEnm}\int_{\eta}^{r_2}\frac{Z_n(ur')}{r'}dr'\cos(n\phi)I(\omega)F_{TEnm}(\omega) \qquad (2.71)$$

where K_{TEnm} is a function of the waveguide dimensions,

$$K_{TEnm} = \frac{n^2 Z_0\pi}{8b} \frac{\left(2-\delta_0^n\right)J_n'^2(ub)Z_n(ub)}{J_n'^2(ua)\left(1-\dfrac{n^2}{u^2b^2}\right)-J_n'^2(ub)\left(1-\dfrac{n^2}{u^2a^2}\right)} \qquad (2.72)$$

and the terms involving ω have been gathered into the function

$$F_{TEnm}(\omega) = \frac{-\omega}{\sqrt{\omega^2 - \omega_{nm}^2}}e^{j\frac{z}{c}\sqrt{\omega^2 - \omega_{nm}^2}} \qquad (2.73)$$

In (2.73), ω_{nm} is the radian cut-off frequency of the TE_{nm} mode,

$$\omega_{nm} = cu \qquad (2.74)$$

46

TM modes:

The appropriate term from (2.60) is

$$\overline{\overline{G}}_{TMnm}\left(b,\phi,z\,|\,r',0,0\right)=$$

$$\frac{j\pi v^2}{8}\frac{\left(2-\delta_0^n\right)J_n^2(vb)\,X_n'(vb)\cos(n\phi)}{J_n^2(va)-J_n^2(vb)}\;X_n'(vr')\frac{\beta_v}{\beta_0^2}\,e^{j\beta_v z}\,\hat{r}\hat{r}$$

(2.75)

Substituting (2.75) and (2.40) in (2.19) gives

$$Er_{TMnm}=K_{TMnm}\int_{\eta}^{r_2}X_n'(vr')\,dr'\cos(n\phi)\,I(\omega)\,F_{TMnm}(\omega)$$

(2.76)   .

where

$$K_{TMnm}=\frac{v^2 Z_0\pi}{8}\frac{\left(2-\delta_0^n\right)J_n^2(vb)\,X_n'(vb)}{J_n^2(va)-J_n^2(vb)}$$

(2.77)

and

$$F_{TMnm}(\omega)=\frac{-\sqrt{\omega^2-\omega_{nm}^2}}{\omega}\,e^{j\frac{z}{c}\sqrt{\omega^2-\omega_{nm}^2}}$$

(2.78)

In (2.77), ω_{nm} is the radian cut-off frequency of the TM_{nm} mode,

$$\omega_{nm}=cv$$

(2.79)

2.6 Summary

The general Green's functions for hollow circular cylindrical and coaxial waveguides have been presented. Representation of the PD current by a one-dimensional filament enabled the integral for the electric field to be solved in both cases. To keep the equations to a manageable size, some restrictions have been placed on the configuration and these can be summarised as follows:

Restriction

Justification

1. The PD current filament should be sufficiently thin (compared to the waveguide dimensions) that the current density can be represented by a one-dimensional function.

PD sources are usually small particles or protrusions, and the ionisation filaments in the SF_6 are also small. Gross defects are of less interest for this work because they are easily detected. Our attention will be focused on small defects at or near the limits of detection.

2. The PD current flows in the radial direction.

The electric field that causes PD is predominantly radial in GIS. In some cases there can be significant components of current in other directions, e.g. when a particle is lodged on the sloping surface of a gas barrier. However, the radial component of current is likely to be common to the majority of defects. If required, the signals generated by other components of the PD current can be analysed using the same methods demonstrated in this work.

3. The electric field is observed at the outer conductor, where only the radial component exists.

This is the most useful location for which to derive the electric field. UHF couplers are usually mounted close to the outer wall of the GIS, where the power frequency field is at its weakest and the UHF signal can be easily extracted from the GIS chamber through a sealed coaxial connector. Often the coupler is mounted in a recess at the outer conductor, but provided this is shallow, the field strength normal to the outer wall will be similar to that calculated for the continuous waveguide.

4. The coupler is located outside the source volume.

The source volume is the volume in which the current density $\bar{J}$ is non-zero. Unless the PD is taking place at the coupler, this restriction is of no consequence.

5. Propagation is in the positive z-direction.

For each signal path between PD source and coupler, choice of the positive z-direction is arbitrary, so this condition can always be satisfied.

6. The waveguide is uniform and infinitely long.	Although a GIS is not a uniform coaxial line, this has to be the starting point for the analysis because the majority of a GIS has a coaxial cross-section. Analysis of the effects of discontinuities is a further task of no small proportions. However, total reflections can be accounted for and this technique will be used in the simulation of UHF signals in a GIS chamber of finite length.
7. The waveguide walls are perfectly conducting.	Ohmic losses in the waveguide walls are discussed in Section 5.3.3 and are shown to be quite small. Over the duration of the simulations carried out in this work, they are insignificant and need not be included for an accurate prediction of the initial UHF signal amplitude.

Before using the expressions developed in this chapter to model actual experiments, it is appropriate to describe the experimental apparatus and some measurement techniques that are required. This is covered in Chapter 3, which also outlines the construction of an HV test cell containing a needle PD source to generate current pulses typical of protrusion-type defects in SF_6.

3. TEST EQUIPMENT AND THE PD CELL

3.1 Introduction

In Chapter 2 we have seen how the electric field inside cylindrical waveguides can be determined from a known distribution of excitation current. In this chapter, a test cell that allows PD current pulses to be recorded is described. The intention is to design a PD source that will be of use in subsequent experiments to investigate the excitation of UHF signals in the test chamber. The measurement techniques used are described and results are included showing typical current pulses for PD at a needle tip (equivalent to a protrusion on GIS conductor).

Before introducing the PD cell, two important items of equipment will be described. These are the transient digitiser used for recording high frequency signals and the computer/software used in the simulation process, implementing the mathematical model of UHF signal excitation.

3.2 The Transient Digitiser and Preamplifer

The Tektronix SCD1000 transient digitiser is designed for capturing single-shot events in the time-domain with a high sampling rate. The signal is acquired using a scan converter tube in which an electron beam is swept across a diode matrix target, with the vertical deflection being driven by the input signal. The diodes in the matrix are charged prior to the scan, and the electron beam depletes the charge on the diodes over which it sweeps. The post-scan charge levels on the diodes are measured by a slower reading beam, from which the vertical deflection, and hence the input voltage, is determined. The maximum number of samples on the horizontal scale is fixed at 1024 by the density of the diode matrix, although 512 and 256 sample records can also be selected. The smallest time window is 5ns in length, giving a maximum equivalent sampling rate of 204.8 Gsamples/s.

The SCD1000 transient digitiser has a specified 3dB upper cut-off frequency of 1000MHz. For most instruments the step response rise time t_r (measured from 10% to 90% of final amplitude) can be obtained from the analogue bandwidth using the formula [50]:

$$t_r = \frac{0.35}{f_{3dB}}$$ (3.1)

where f_{3dB} is the cut-off frequency in Hz. The actual risetime of the SCD1000 is faster than the 350ps predicted by this equation because the scan converter attenuates the high frequency components of the signal less than would be expected given a Gaussian response [50]. The risetime was estimated by using an HP5082-0151 step recovery diode to generate a very fast voltage step (quoted risetime $\approx$ 100ps [51]). When this waveform was recorded on the digitiser, the measured risetime of the signal on the display was 300ps. This value was used as the step response risetime for the digitiser required in Chapter 4.

The UHF signal levels from couplers (typically <1mV peak-to-peak) are usually too small for direct recording on the digitiser, which has a maximum vertical sensitivity of 10mV/div. A broadband preamplifier was therefore required to increase the signal amplitude. The HP8447D amplifier used for this purpose has a gain of 26dB and a 3dB passband from 75kHz to 1.7GHz, with a gain flatness of ±1.5dB over frequencies in the range 100kHz to 1.3GHz. The frequency response thus extends well beyond that of the digitiser, so the measurement bandwidth is not compromised. The voltage gain factor of 20 results in a satisfactory signal-to-noise ratio for the digitised signals.

3.3 Computer and Software

A PC equipped with a GPIB card was used to store the signals captured by the digitiser. The Labview graphical programming environment [52] was used to manage the data transfer using an instrument driver supplied with the software. However, the primary use of the PC was in performing simulations of the UHF signals in the experimental configurations described in Chapters 4 and 5. The Mathcad PLUS 6.0 software package [53] was used for this purpose because the relevant expressions from Chapter 2 can be typed into the Mathcad worksheet with little modification. This results in a very clear mathematical model that is capable of generating numerical results and allows all the parameters to be varied readily. Most importantly, the FFT processing required in Chapter 5 is also available. The time taken to accomplish the simulation is dependent on the computer specification. The PC contained an Intel 486 processor operating at 50MHz. A maths co-processor was also fitted and the system had 8MB of RAM.

3.4 PD Cell and Current Pulse Measurements

3.4.1 Description of the cell

The PD cell shown in Figure 3.1 contains a needle mounted on the centre conductor of a 50Ω N-type connector in a gas-tight envelope filled with SF_6. The electric field at the needle tip is enhanced by the small radius of curvature, over-stressing the SF_6 insulation so that PD occurs. The 1mm diameter needles were manufactured by Ogura. Needles having a tip radius of $5\mu m$ were selected for use in the experiments, as these were the sharpest available and should therefore give the lowest PD inception voltage. A lower voltage is advantageous because it minimises the likelihood of unwanted PD occurring elsewhere in the apparatus, and reduces the risk of electrical breakdown in the cell.
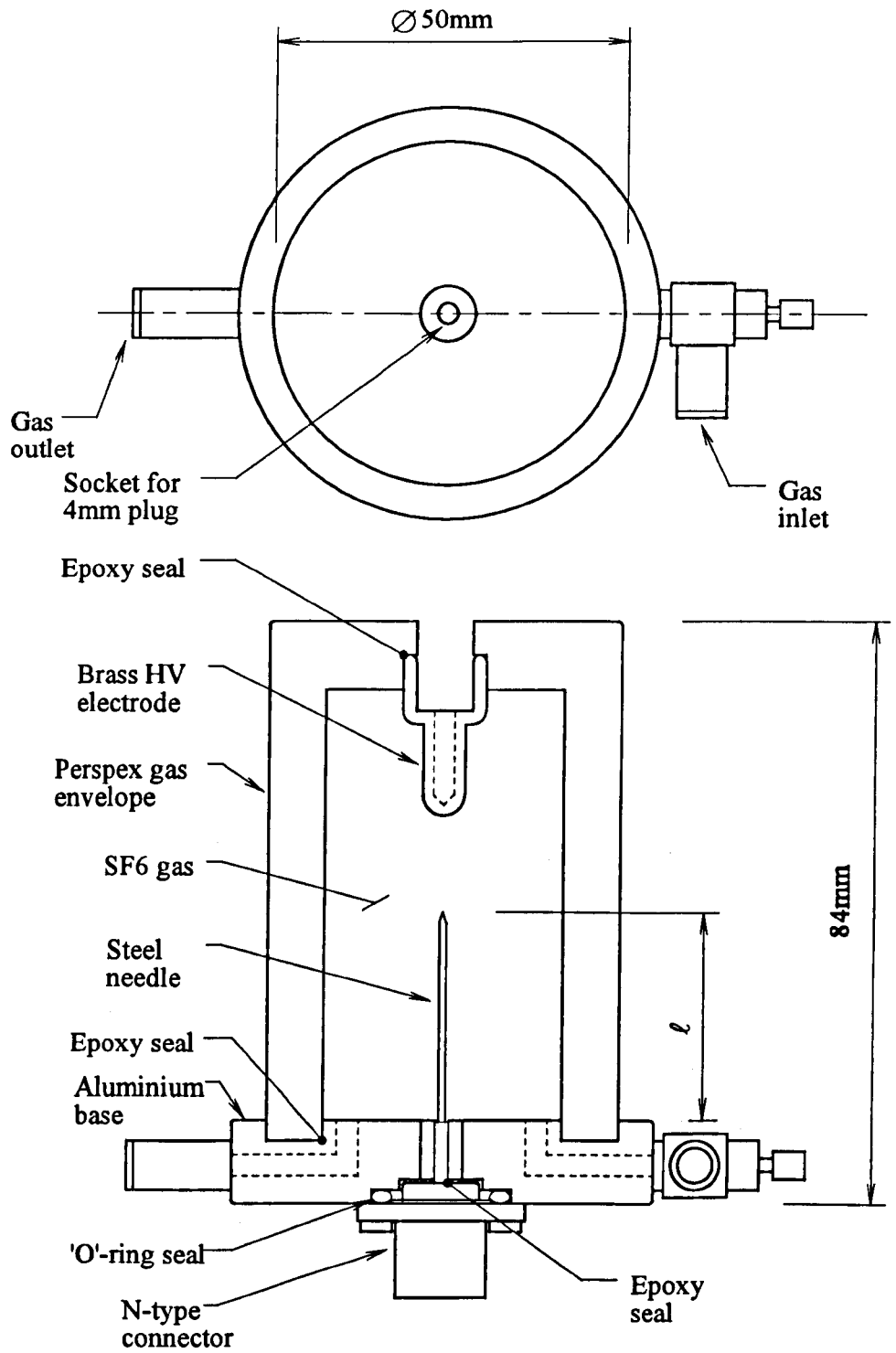
Figure 3.1 Test cell containing a needle PD source with a connector to facilitate external measurement of PD current pulses.

The base of the cell is made of aluminium, and the diameter of the central hole through which the connector stub passes is designed to maintain a 50Ω impedance level to the base of the needle. This is necessary to minimise any mismatch that would cause multiple reflections of the pulse. An 'O'-ring is used to form a seal around the flange of the N-type connector. Other joints in the gas envelope were sealed using epoxy adhesive, as shown in Figure 3.1. Nylon screws were used to hold the Perspex cover firmly in place. This choice of material for the cover permits viewing of the needle. However, the primary reason for using a dielectric is to approximate the actual situation of a protrusion in GIS, where the gas envelope immediately surrounding the defect would not be present. The greater the number of metallic components used in the test cell, the more extraneous reflections and induced currents may perturb the pattern of the radiated field away from that predicted by theory.

The gas inlet fittings on the cell are designed for use with 4mm O.D. Nylon tube, commonly used in pneumatic systems. SF_6 gas is admitted to the cell through a self-sealing flow regulator inlet. To avoid trapping a large quantity of air inside the cell, a gas outlet is also provided. The cell is first purged by passing a slow stream of SF_6 through it while the base is held uppermost. A small pressure gauge was then connected to the outlet to seal the cell and monitor its pressure. Pressurisation of the Perspex envelope was not possible for safety reasons. Therefore only a slight positive pressure (up to 1.2 bar absolute) was admitted to ensure that if a slight leak was present, ingress of air would be unlikely. The main purpose of the pressure gauge is to indicate any gas leakage. After filling, the cell was left to stand for 30 minutes to ensure that the SF_6 was not escaping at a rate that would risk a damaging flashover should the insulation be weakened through dilution of the SF_6.

3.4.2 Energising the cell

The HV electrode is located at the top of the test cell and contains a shielded socket for a 4mm plug. During measurements the cell was mounted inside the cylindrical aluminium chamber, as shown in Figure 3.2. This arrangement ensures that the cell is safely screened by the earthed chamber while it is energised. The cell is retained in position by the N-connector, which protrudes through a hole in the chamber wall and allows the base of the cell to be clamped to the wall. An additional earth wire connects the base of the cell to the test chamber wall.

The 50Hz AC HV supply to the test cell was obtained using an 8KVA single phase Ferranti step-up transformer. The transformer has two primary windings that can be connected in series to give a 220V : 40,000V step-up ratio. A variac was used to adjust the mains input voltage level, thereby controlling the transformer output voltage. The HV cable was fed into the test chamber through a 100mm diameter hole in the centre of the adjacent endplate (Figure 3.2). More compact feedthrough arrangements using ceramic bushings and coaxial cables were tested, but were hampered by the generation of unwanted PD in the air around the HV conductor.

3.4.3 Measurement precautions

Should breakdown occur between the HV electrode and the needle, the digitiser input will effectively be connected to the output of the HV transformer. Protection measures were considered, but none were deemed suitable to meet the requirements of a very fast (sub-nanosecond) response time and high current capacity without severely restricting the measurement bandwidth. For example, semiconductor devices such as Transzorbs could provide adequate protection, but the junction capacitance is too high for them to be connected across the digitiser input without severely distorting the PD current pulses. To afford some measure of protection for the digitiser, a 10dB SMA attenuator was connected between the cable and the
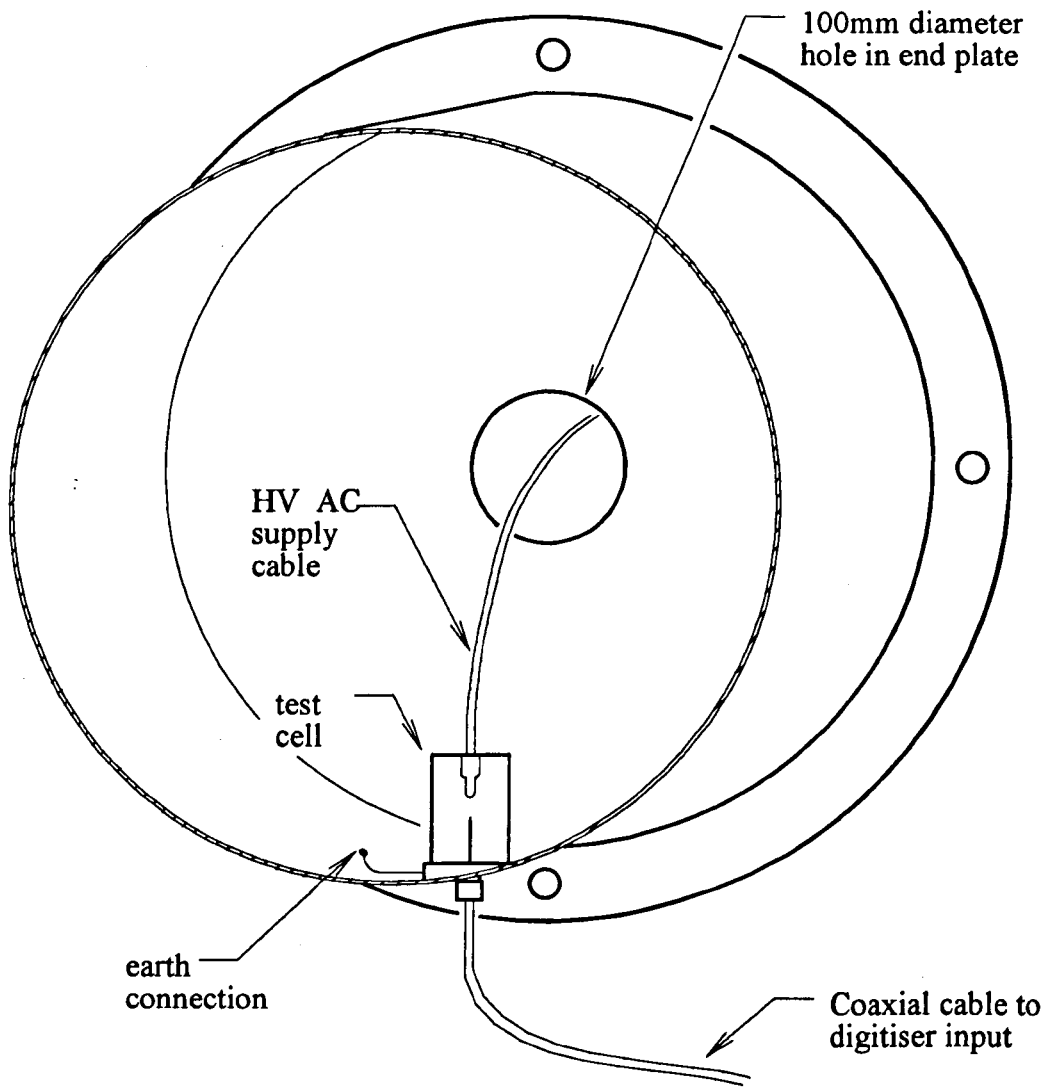
Figure 3.2 Cut-away view of the aluminium chamber showing connections to the needle test cell.

digitiser input. The risk of damage was reduced by only connecting the digitiser to the test cell for the minimum period required to record a single PD pulse. The attenuator remained permanently connected to the cable, providing a low impedance (50Ω) path to ground. This prevents capacitive charging of the cable to a high voltage level capable of damaging the digitiser at the moment of reconnection. As a further precaution against flashover occurring during pulse measurement the HV supply to the cell was always increased to a voltage 50% above the intended measurement voltage prior to connecting the cable. If flashover does not occur under these conditions, a safe measurement should be ensured at the lower measurement voltage.

3.4.4 Current pulse measurements

The arrangement of the measurement equipment is shown in Figure 3.3. A length of RG316/U micro-coaxial cable fitted with SMA connectors was used to link the test cell to the digitiser. Captured pulse waveforms were transferred to data files on computer disk through the GPIB interface. A spectrum analyser displaying the signal from a UHF disc coupler [20] mounted on the cover plate at the far end of the chamber was used to detect the inception of PD in the cell as the applied voltage was increased. This avoids the need to connect the cell to the digitiser until stable operation has been established.

The digitiser timebase was triggered on the rising edge of the voltage pulse developed across its 50Ω input impedance. As the measurement system is impedance matched between the base of the needle and the digitiser input, the pulse shape is maintained. The amplitude of the voltage pulses must be corrected for the losses in the cable and 10dB attenuator. Using a pulse generator to supply pulses comparable with typical PD pulses, a correction factor of 3.64 was determined by measuring the reduction in amplitude caused by introducing the cable and attenuator between the pulse generator and the digitiser. This factor allows the voltage at the base of the
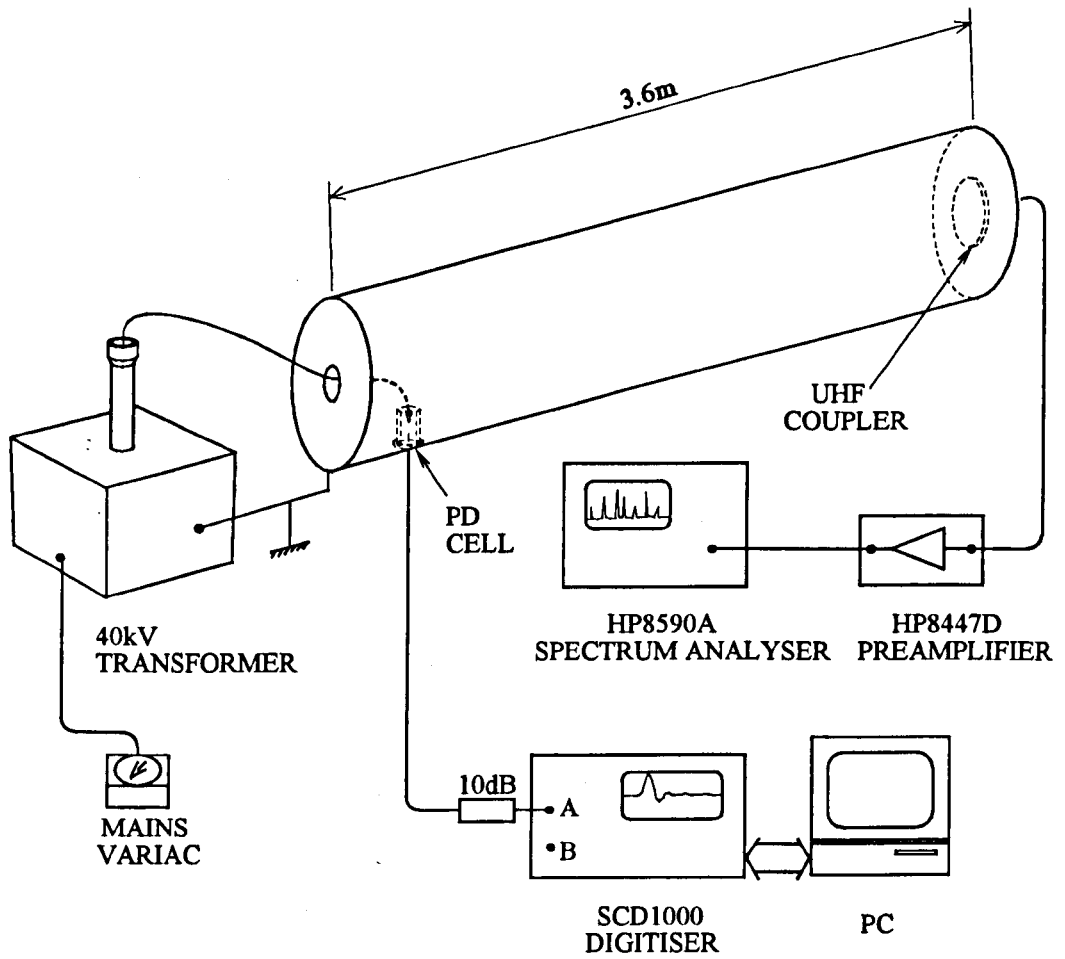
Figure 3.3 Experimental configuration used to monitor PD inception
in the needle test cell and record the current pulses.

needle to be obtained by scaling the voltage waveform accordingly. The current pulse is obtained by dividing this voltage by the 50Ω input impedance of the measurement system.

Needles of lengths ℓ=15mm and ℓ=30mm were tested, and the PD inception voltage was about 18kV in both cases. Some typical current pulses measured at an applied voltage of 20kV are shown in Figure 3.4. The charge levels assigned to the current pulses were determined by integrating the main lobe of the current pulse in each case. The half-amplitude pulse widths are in the region of 500ps. As the pulse widths and risetimes are close to the step response risetime of the digitiser, the actual current pulse shape may not be fully represented. Appropriate correction techniques are introduced in Chapters 4 and 5 to obtain a better measure of the pulse shape.

No attempt has been made in this work to investigate variations in PD pulse shape with parameters such as gas pressure, defect geometry and applied field. The purpose of developing the cell is simply to obtain a PD source that meets the following requirements:

- the PD current flows along a radially directed path.

- the location of the current path inside the test chamber is clearly defined.

- the PD current pulses can be recorded accurately.

These criteria are satisfied by the needle test cell. The current pulse records can be used to define the input to a computer simulation of the electric field which the pulse would be expected to excite within the test chamber. This procedure will be described in Chapter 4.
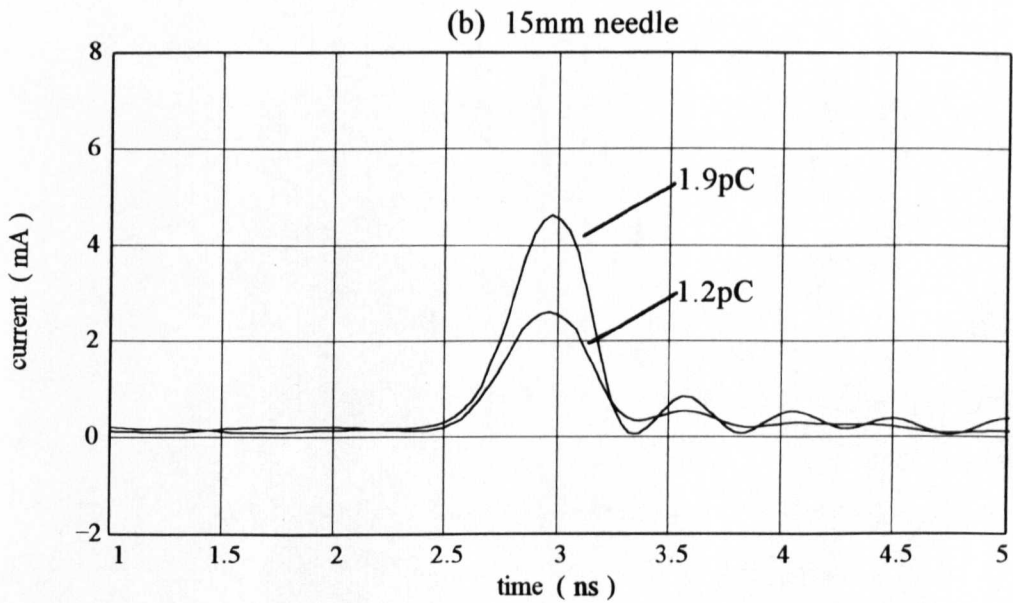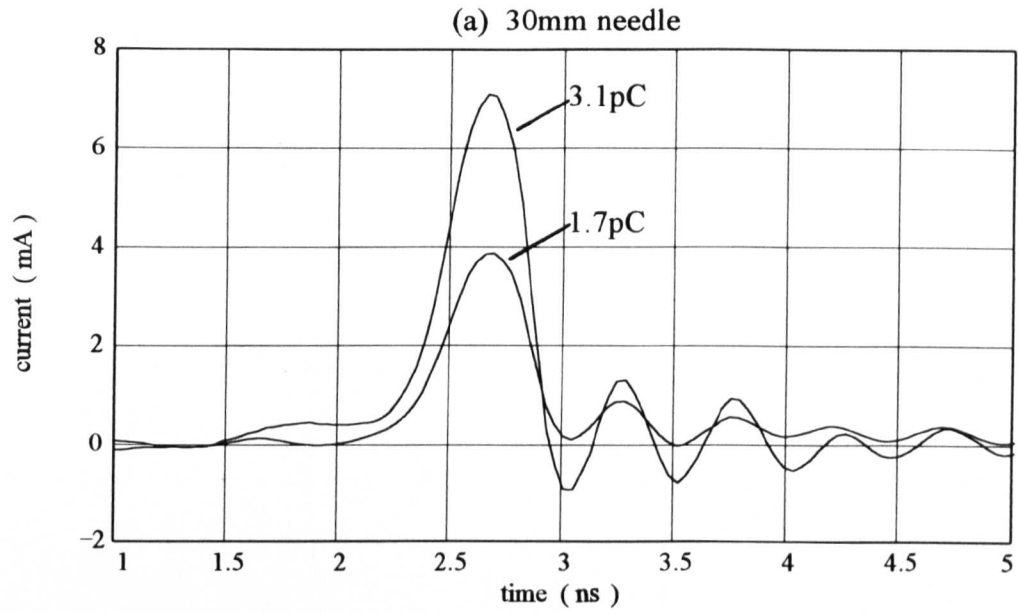
Figure 3.4   Typical PD current pulses from the needle test cell, showing the charge
levels associated with the main lobe of each pulse. (a) 30mm needle,
(b) 15mm needle.

4. CYLINDRICAL CONFIGURATION

4.1 Introduction

This chapter deals with the excitation of UHF signals in a hollow circular cylindrical chamber, using both real and simulated PD sources. At the time this work was carried out, the aim was to obtain an analytical expression for the UHF signal in the time-domain. This was achieved by first deriving the impulse response of each mode from the transfer functions determined in Chapter 2. By using a Gaussian shape for the PD current pulse, an approximate expression for the response was found. Comparison with numerical results based on convolution of a Gaussian pulse with the waveguide impulse response shows that the analytical expression is very accurate, except during the initial part of the response for a period equal to the width of the excitation pulse.

Simulation of the UHF signal is achieved by generating the time-domain signal records for each mode separately, accounting for reflections at the ends of the chamber. These records are then summed with appropriate weightings according to the relative positions of the source and coupler. While the results are not as accurate as those subsequently obtained for the coaxial configuration by using FFT processing, they served to validate the theoretical approach. The results also show that the method used for simulating PD on a probe is comparable with real PD. This is an important result for the subsequent coaxial experiments, in which the PD cell could not be used. By avoiding the use of numerical procedures until the final stage in this chapter, some interesting results are obtained that shed light on the nature of the time-domain UHF signals excited by PD.

4.2 Experimental Procedures

4.2.1 Description of the cylindrical chamber and test equipment

The experimental configuration is shown in Figure 4.1. The 3.6m long cylindrical chamber and its end plates are made of aluminium. UHF signals excited within the chamber take several microseconds to decay, so that over the duration of the measurements presented here (40ns maximum) the chamber walls can be considered to be perfectly conducting. Ideally the chamber would be made very long, or with fully absorbing terminations, so that no reflections occurred within the measurement period. However, because these conditions are impractical, totally reflecting endplates have been used instead. This limits the duration of the simulation, since the number of reflections which must be accounted for increases with time. UHF signals inside the chamber were monitored by means of a short monopole probe (Figure 4.2) protruding through the wall in the central plane. This type of probe was chosen because its response to an incident electric field is known. Furthermore, the probe is quite small, so that its response can be approximated as the response to the electric field at a point. The probe coupler can be mounted at various positions relative to the PD source. Signal from the probe was amplified and recorded using the transient digitiser, at an effective sampling rate of 12.8GHz (256 samples with a 20ns record length). The timebase of the digitiser was triggered by the excitation pulse, enabling both the pulse shape and the corresponding UHF signal to be captured. Although the digitiser cannot simultaneously capture two signals, it can be set to record the sum of the signals at the two input channels. Propagation delays in the test chamber and connecting cables ensure that the current pulse and the UHF signal can be separated because the UHF signal arrives after the current pulse. The sampled signal was transferred to a PC for storage and subsequent processing. At UHF, the maximum record length that can be captured without distortion by the digitiser is 20ns. When longer record lengths are used, the signal is lost because consecutive vertical deflections of the electron beam in the SCD1000 scan converter begin to merge [50].

3.6m

1.8m

0.3m

0.5m
I.D.

40kV
TRANSFORMER

PC

10dB

A

B

MAINS
VARIAC

SCD1000
DIGITISER

HP8447D
PREAMPLIFIER
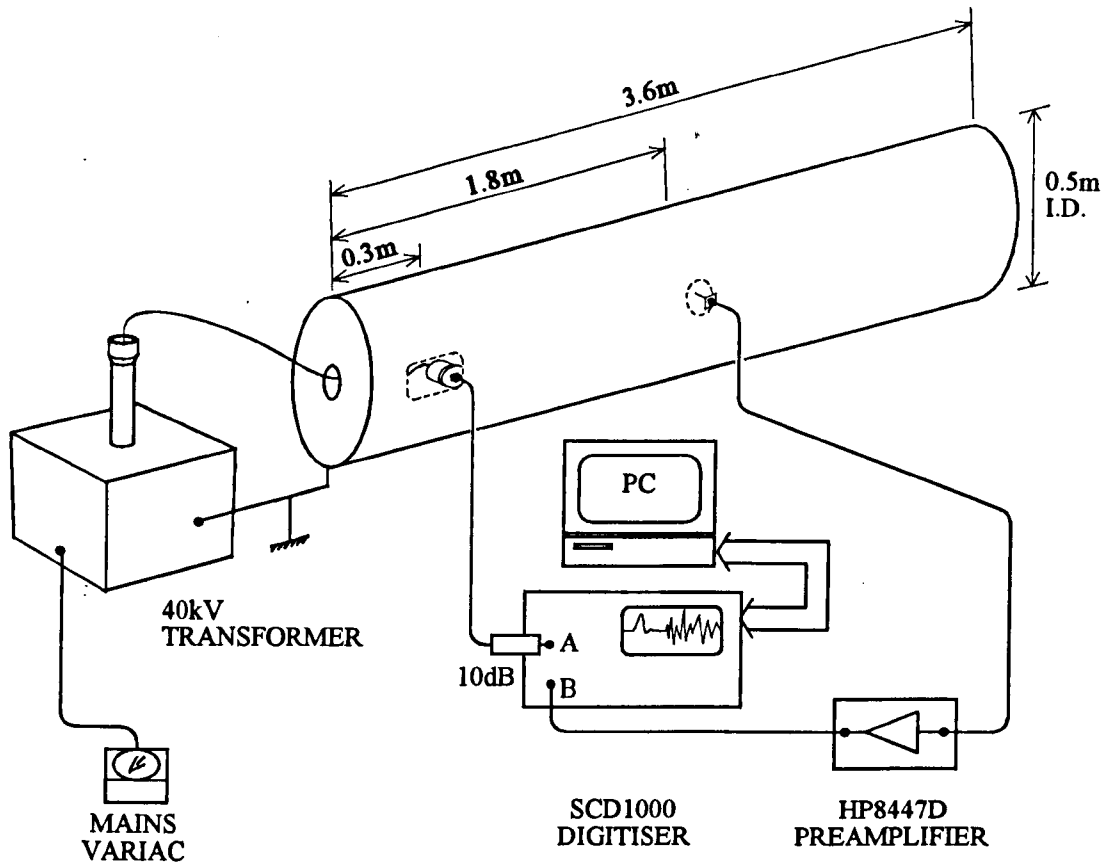
= cut-away view showing the PD cell

= cut-away view showing the probe coupler

Figure 4.1 Experimental apparatus for investigating UHF signals in the
hollow cylindrical chamber.

Probe dimensions: h=30mm, r_p=0.65mm
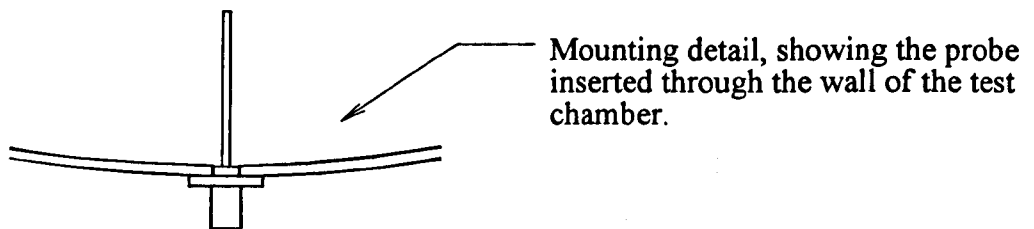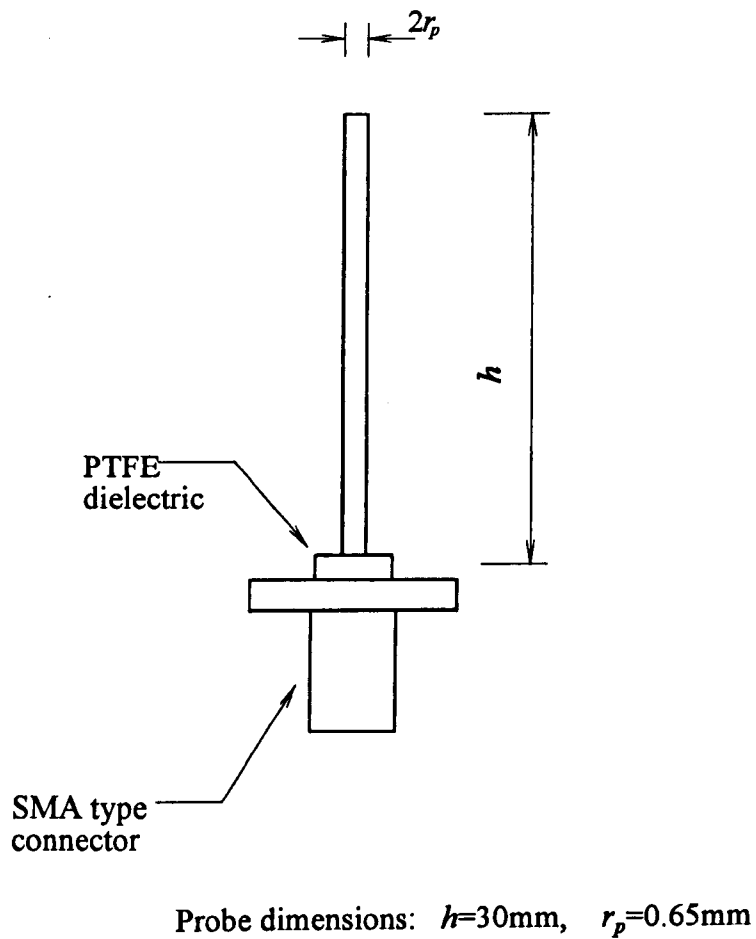
Figure 4.2 Dimensions and mounting detail for the probe used to measure the UHF electric field in the hollow cylindrical cavity.

UHF signals were excited within the chamber by a radial current pulse located in the plane 0.3m from one end. Two excitation methods were used:

- A probe identical to the output probe described above was used to inject a current pulse of constant amplitude at a repetition frequency of 1kHz. Longer records of the response could then be built up by delaying the digitiser triggering in 20ns steps.

- The cell containing a needle PD source (Figure 3.1) was mounted in the chamber and connected to an HV transformer by bringing the cable through a hole of diameter 100mm in the centre of the adjacent end plate. Needles of lengths $\ell = 30$mm and $\ell = 15$mm were used, each having a tip radius of 5μm. The cell was filled with SF_6 at 10% above atmospheric pressure, and an AC voltage in the range 18 - 20kV was applied to the HV electrode. The resultant PD current pulses flow along the needle and into the 50Ω measurement system so that the discharge magnitude can be recorded. In this case successive pulses are not identical, so the maximum record length is limited to 20ns.

Simulations were then carried out using the measured current pulses and the known configuration of source and coupler. The energy delivered to the 50Ω load from the coupler was integrated over the duration of the signal record for both simulated and experimental signals, to facilitate comparison. The simulated and experimental energy levels were found to vary consistently as the parameters of the experiment were altered.

4.2.2 Measurement of the UHF electric field using a monopole probe

The probe coupler does not measure the UHF electric field strength directly, so its response must be modelled to obtain an expression for the output voltage into the measurement system impedance, $Z_L = 50$Ω. A short monopole can be regarded as an impedance Z_p in series with a voltage source $-h_e Er$ [54], where Z_p is the input impedance of the probe, h_e is its effective height and Er is the incident electric field

parallel to the probe. This equivalent circuit for a loaded monopole probe is shown in Figure 4.3. Values for h_e and Z_p were determined using published tables for dipoles [55]. The data is tabulated as a function of the parameter $\Omega = 2\ln\left(2h/r_p\right)$, where h is the dipole half-length and r_p is its radius. To use these tables for the monopole, we note that the electromagnetic fields of a monopole are equivalent to those of half a dipole when an infinite perfectly conducting sheet is located in the plane of symmetry at the dipole's centre. The height of the monopole is then equal to the half-length of the corresponding dipole, and the impedance of the monopole is half that of the dipole. The dimensions of the probe used in these experiments are h=30mm and r_p=0.65mm (Figure 4.2), giving $\Omega = 9.05$. The data in [55] is only tabulated for integral values of Ω, so the values corresponding to $\Omega = 9.0$ have been used. The effective half-height and impedance values are expressed in normalised form as a function of βh, where β is the radian wave number. After denormalising, halving the impedance values and scaling for h=30mm, the probe data of Table 4.1 is obtained. For the completely general model, both h_e and Z_p are complex quantities. Only the lowest four frequencies from the table in [55] are shown, as these adequately cover the required frequency range.

Table 4.1

Data for the 30mm monopole probe model.

frequency (MHz)	effective height (mm)		impedance (Ω)	
f	$\Re\{h_e\}$	$\Im\{h_e\}$	$\Re\{Z_p\}$	$\Im\{Z_p\}$
796	14.06	-0.03	2.5	-297.3
1114	14.54	-0.08	5.1	-189.9
1432	15.20	-0.16	9.2	-122.9
1751	16.07	-0.23	15.1	-73.3

$$V_L = -h_e Er \frac{Z_L}{Z_L + Z_p}$$
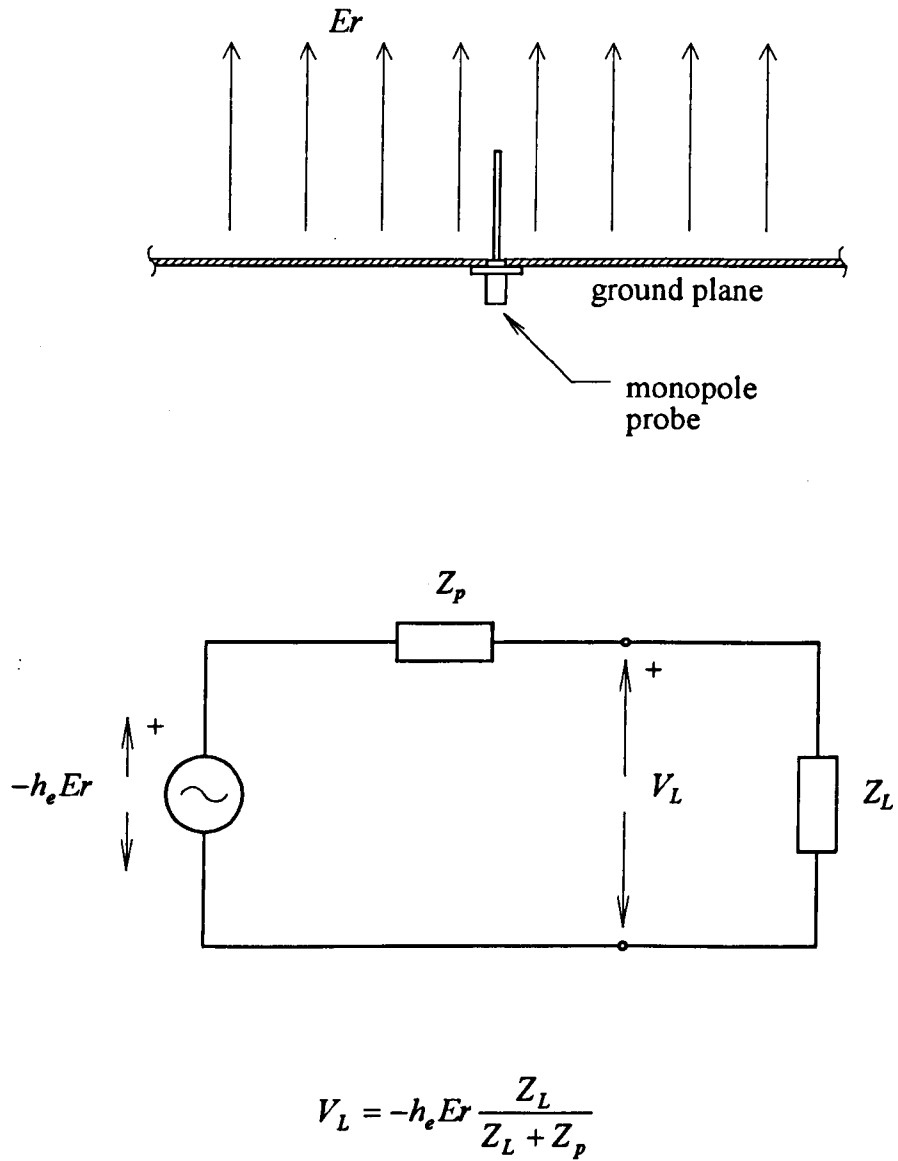
Figure 4.3 Equivalent circuit of a loaded monopole probe in a ground plane, excited by an electric field normal to the ground plane.

At frequencies for which the monopole length is small compared to the wavelength, its impedance can be approximated as purely capacitive [54]. The frequency range of interest is from 350MHz (just below the lowest cut-off frequency in the chamber) to 1500MHz. The real part of Z_p in Table 4.1 does not exceed 10% of the imaginary part in this frequency range. If the relatively small real part is neglected, the impedance can be approximated by that of an equivalent capacitance $C_e = -1/\omega \Im\{Z_p\}$, particularly at lower frequencies. The small imaginary part of h_e is neglected in this analysis. Although h_e and C_e do begin to vary in the 350 - 1500MHz range, fixed values were used so as to retain a simple model. By interpolating the data for $\Re\{h_e\}$ and $\Im\{Z_p\}$ from Table 4.1, values at the centre frequency of the measurement range (f_c=925MHz) were obtained. The results were h_e=14.2mm and $Z_p = -j249\Omega$, giving C_e = 0.69pF. The calculated capacitive impedance based on this value of C_e is compared with the tabulated values of $\Im\{Z_p\}$ in Figure 4.4.

With reference to the circuit of Figure 4.3, the output voltage of the loaded monopole can be written in Laplacian notation as

$$V_L(s) = -h_e\, Er\, \frac{Z_L}{Z_L + 1/sC_e} \qquad (4.1)$$

where $s = j\omega$. To obtain a simple time-domain expression for the output voltage, we note that at frequencies for which

$$|1/sC_e| \gg Z_L \qquad (4.2)$$

equation (4.1) can be written as

$$V_L(s) \approx -sh_e\, C_e\, Z_L Er \qquad (4.3)$$
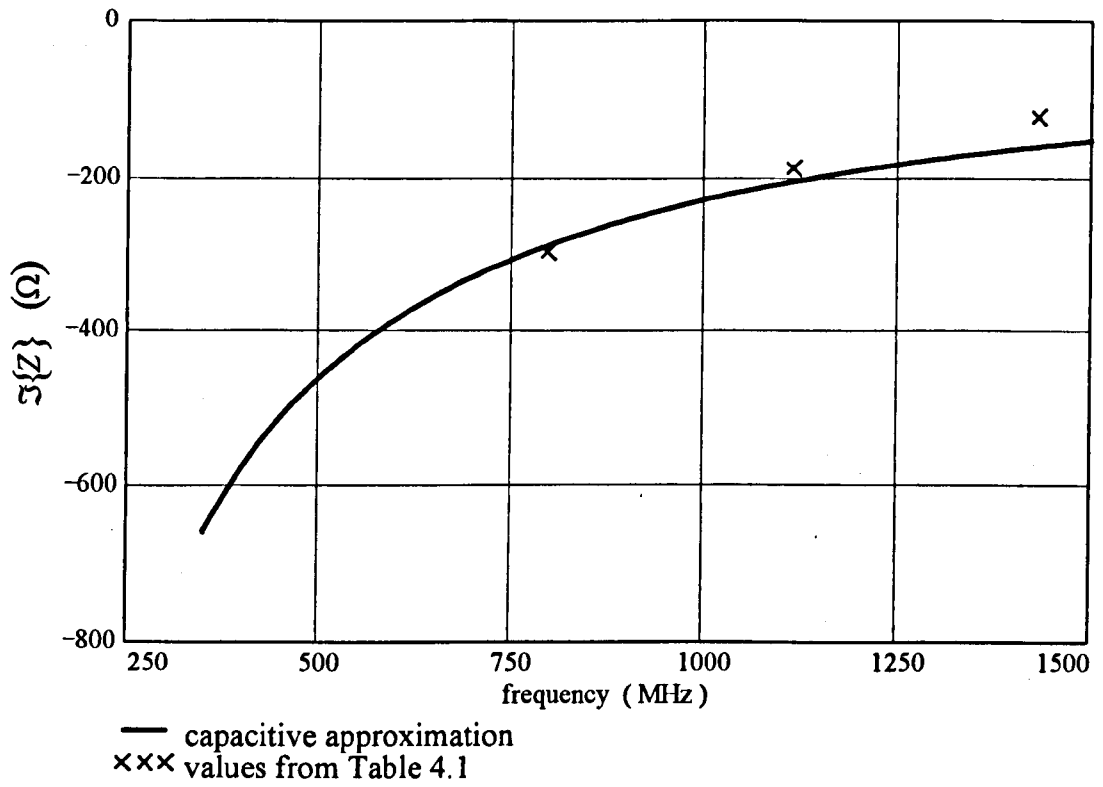
Figure 4.4 Comparison of the tabulated impedance values for the 30mm probe and the impedance of the capacitive approximation using $C_e = 0.69$pF.

Inverse Laplace transformation gives the probe output voltage as being proportional to the time derivative of the incident field:

$$v_L(t) \approx -h_e\, C_e Z_L\, \frac{dEr}{dt} \qquad (4.4)$$

Examination of Figure 4.4 indicates that $|1/j\omega C_e|$ lies in the range $13Z_L \to 5Z_L$, so that condition (4.2) is not strictly satisfied at higher frequencies in the range of interest. However, this approximation is tolerated to avoid overcomplicating the model.

4.2.3 Current pulse injection technique

Pulsing techniques have been used previously to simulate PD [23,40,41], but only in the qualitative sense of exciting similar resonances in a GIS chamber. To permit comparison with theory, a controlled and quantifiable current pulse is required. When a short positive voltage pulse is applied to a monopole the resulting current that flows on the probe is first positive and then negative as its capacitance with respect to the ground plane is charged and discharged. Thus a bipolar current pulse flows on the probe, as shown in Figure 4.5(a), radiating fields of opposite polarity in quick succession. The correct technique for generating a unipolar current pulse on a short monopole probe in a ground plane is to drive it with a single rising voltage waveform as shown in Figure 4.5(b).

The circuit used to generate the fast rising voltage waveform required to drive the probe is shown in Figure 4.6. CMOS logic gates of the 74AC family were used because of their sub-nanosecond transition times. A resistive microstrip matching circuit in the output stage divides the signal between a 50Ω cable feeding the probe and the 50Ω input of the digitiser. The measurement circuit forms a simple time-domain reflectometer, and the voltage waveform reflected from the probe can be recorded. Using the simple capacitive probe model, the shape of the current pulse i_b
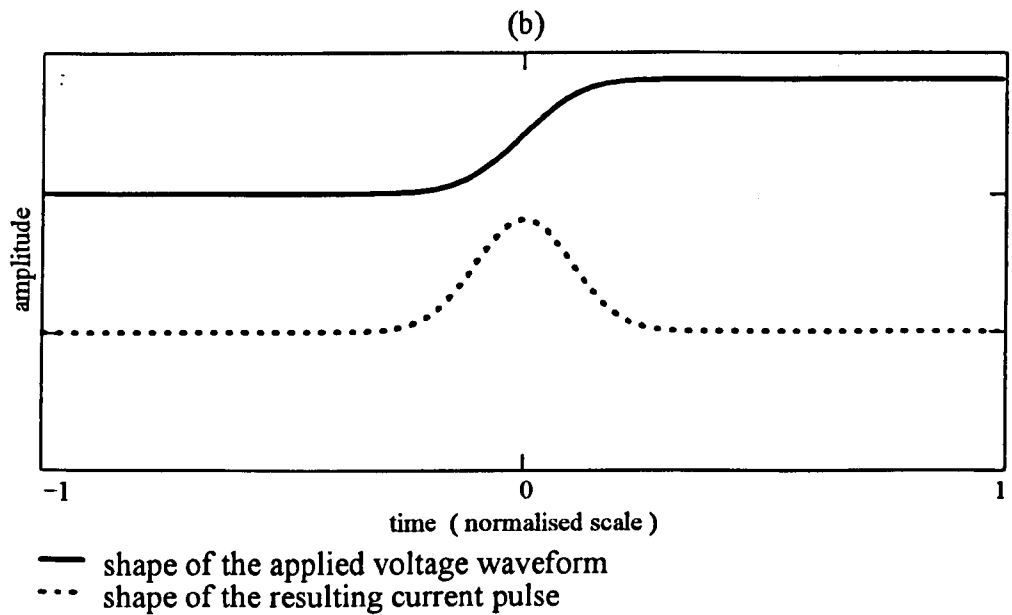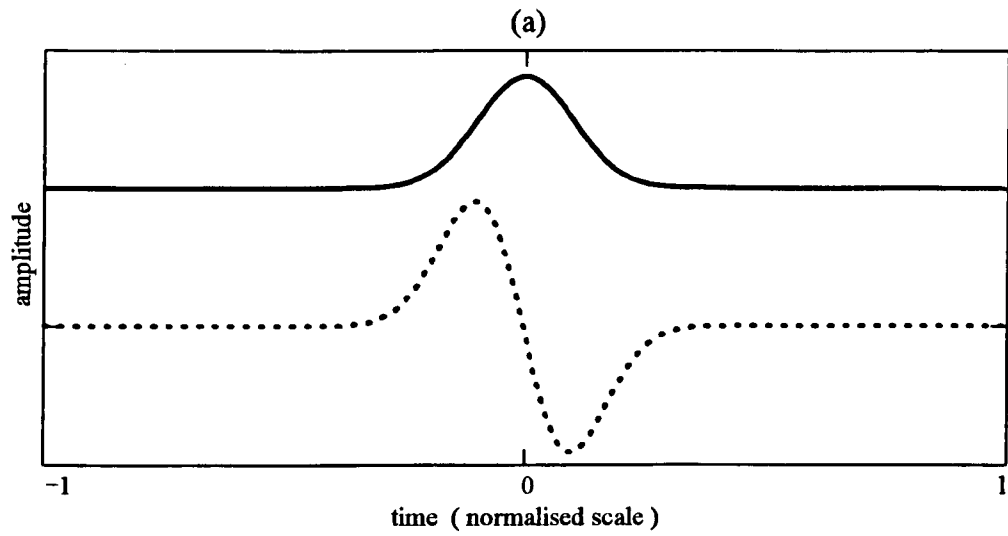
Figure 4.5   Generating current pulses on the capacitive monopole probe, (a) by applying a voltage pulse and (b) by applying a voltage step.
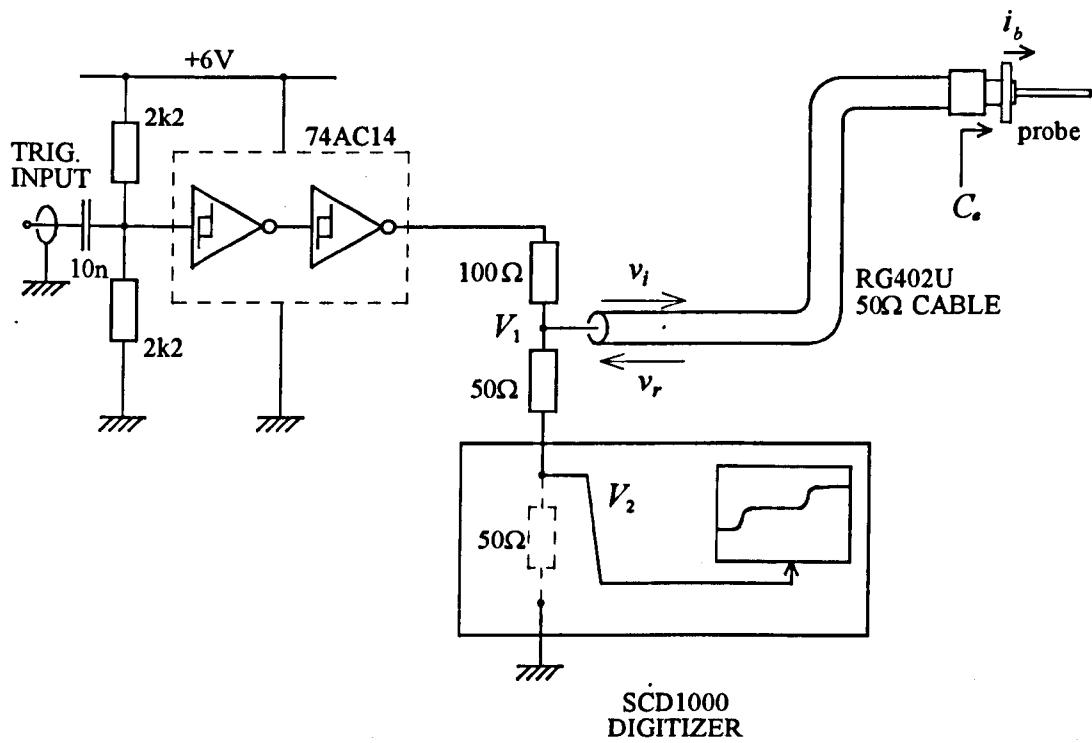
Figure 4.6 CMOS driver and monitoring circuit for generating controlled current pulses on the monopole probe.

flowing into the base of the probe was obtained from the reflected voltage v_r using the equation

$$i_b = C_e \frac{dv_r}{dt} \qquad (4.5)$$

The apparent risetime t_a of the waveform is longer than the true risetime t_r due to the finite step response risetime of the digitiser, t_0=300ps. An estimate of the true risetime can be obtained from the formula [50]:

$$t_r = \sqrt{t_a^2 - t_o^2} \qquad (4.6)$$

This correction was made by compressing the timescale of the voltage waveform to give the corrected risetime before differentiating v_r as required by (4.5). The process of determining the current pulse is illustrated in Figure 4.7. The voltage recorded by the digitiser must be amplitude scaled to correct for the voltage division that occurs in the potential divider at the output of the pulse circuit of Figure 4.6. The scaling factor (V_1/V_2) was found to be 2.016, based on the steady-state voltages. The amplitude scaled waveform shown in Figure 4.7(a) corresponds to the voltage $V_1 = v_i + v_r$ in Figure 4.6, where v_i is the waveform flowing into the coaxial cable and v_r is the waveform reflected from the probe. Two rising edges are visible, but only the second is required to determine the probe current. The risetime of the second edge was t_a=550ps. Correcting for the digitiser risetime using (4.6) gives t_r = 460ps. The reflected rising edge is shown in Figure 4.7(b), in which the timescale has been compressed by the factor $t_r/t_a = 0.836$. Although v_r is superimposed on v_i, this does not affect the determination of the current pulse shape because v_i is has stabilised by this time and the voltage offset is eliminated by the differentiation process. The current pulse $i_b(t)$ determined using (4.5) is shown in Figure 4.7(c) and compared with a Gaussian pulse for which I_0=1.79mA and σ=175ps (see equation 4.19).
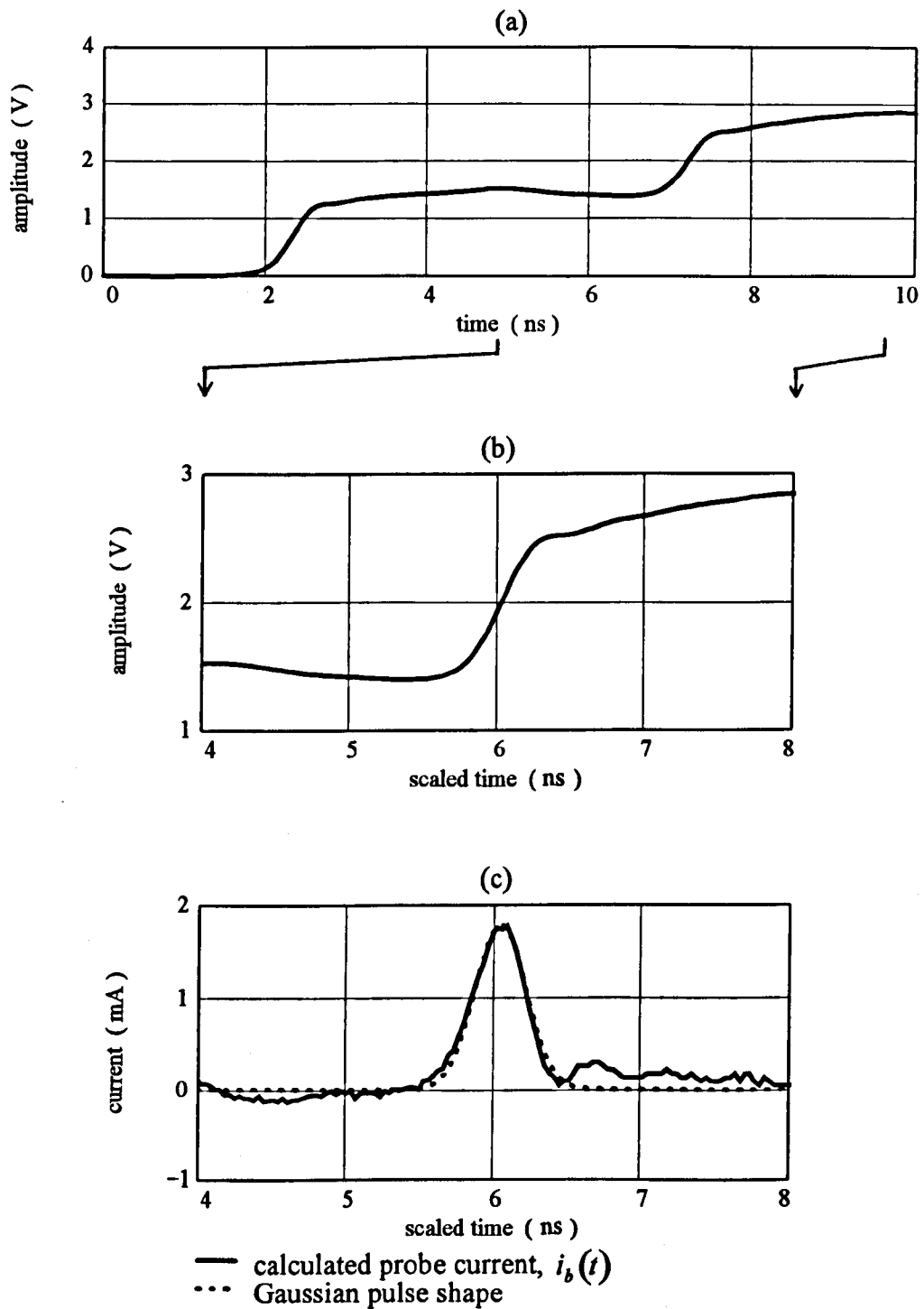
Figure 4.7   Illustration of the steps involved in determining the current flowing into the base of the monopole probe. (a) The recorded voltage V_1 in the circuit of Figure 4.6, (b) the edge reflected from the probe, following scaling to correct for the digitiser risetime, and (c) the current pulse determined using (4.5).

The current i_b cannot be constant over the length of the probe as it must fall smoothly to zero at the tip. A good approximation to the current distribution, often used in the analysis of monopoles [56], is a cosine function falling to its first zero at the probe tip:

$$i(x) = i_b \cos\left(\frac{\pi}{2}\frac{x}{\ell}\right) \quad , \qquad x = 0 \rightarrow \ell \qquad (4.7)$$

The average value of current over the probe length at any instant is then

$$i = 2i_b/\pi \qquad (4.8)$$

4.3 Time-Domain Simulation

4.3.1 Derivation of the waveguide impulse response

The study of pulse propagation in a waveguide is complicated by the mathematical form of the impulse response which makes it difficult to obtain an analytical expression for the response. Recent publications have presented some asymptotic expressions for the single mode waveguide response to certain input pulse shapes [57,58]. However, these works assume that the source pulse is a plane-wave electric field, and result in different expressions for the impulse response to those developed below for a current source.

All modes that have a radial component of electric field and a cut-off frequency below 1500MHz in a hollow circular cylindrical waveguide of internal radius 0.25m are listed in Table 4.2. To generate this data, equations (2.26) and (2.27) were first solved using the Mathcad software package. Equations (2.48) and (2.52) were then used to calculate the corresponding cut-off frequencies.

Table 4.2

Higher order modes in a hollow circular waveguide of internal radius 0.25m.

Mode designation	Mode eigenvalues		Cut-off frequency (MHz)
	q_{nm}	p_{nm}	
TE_{11}	1.8412	-	351.4
TM_{01}	-	2.4048	459.0
TE_{21}	3.0542	-	582.9
TM_{11}	-	3.8317	731.3
TE_{31}	4.2012	-	801.8
TM_{21}	-	5.1356	980.2
TE_{41}	5.3176	-	1014.9
TE_{12}	5.3314	-	1017.5
TM_{02}	-	5.5201	1053.5
TM_{31}	-	6.3802	1218.5
TE_{51}	6.4156	-	1225.3
TM_{12}	-	7.0156	1339.9
TE_{22}	6.7061	-	1280.8
TE_{61}	7.5013	-	1432.6
TM_{41}	-	7.5883	1449.3

The frequency-domain transfer functions relating the electric field at a point on the outer conductor of a hollow circular waveguide to a PD current source given by (2.45) and (2.49) are repeated here for ease of reference:

$$Er_{TEnm} = K_{TEnm} \int_{r_1}^{r_2} \frac{J_n(q_{nm}r'/a)}{r'} dr' \, cos(n\phi) \, I(\omega) F_{TEnm}(\omega) \tag{4.9}$$

$$Er_{TMnm} = K_{TMnm} \left[J_n(p_{nm}r_2/a) - J_n(p_{nm}r_1/a) \right] cos(n\phi) I(\omega) F_{TMnm}(\omega) \tag{4.10}$$

The overall response to a current pulse is obtained by superposition of all modes that make a significant contribution within the bandwidth of the measurement system. Three common elements are present in these equations:

- A normalisation constant K that is dependent on the waveguide dimensions.

- A function of the source geometry and the relative positions of the source and coupler in the transverse (r, ϕ) plane.

- The product of $I(\omega)$ with the frequency-domain transfer function of the mode in question, $F(\omega)$.

The effect of the z co-ordinate is contained in $F(\omega)$, leading to the dispersive nature of the propagation. The response to a unit current impulse $i(t) = \delta(t)$ (corresponding to a theoretical instantaneous charge transfer of 1 Coulomb) can be found by setting $I(\omega) = 1$. Making the Laplacian substitution $s = j\omega$ in (2.47) and (2.51), we obtain

$$F_{TEnm}(s) = s \frac{e^{-\frac{z}{c}\sqrt{s^2 + \omega_{nm}^2}}}{\sqrt{s^2 + \omega_{nm}^2}} \tag{4.11}$$

$$F_{TMnm}(s) = \left[s + \frac{\omega_{nm}^2}{s} \right] \frac{e^{-\frac{z}{c}\sqrt{s^2 + \omega_{nm}^2}}}{\sqrt{s^2 + \omega_{nm}^2}} \tag{4.12}$$

The following term common to both these equations is a standard form for inverse Laplace transformation [59],

$$\frac{e^{-k\sqrt{s^2+a^2}}}{\sqrt{s^2+a^2}} \Leftrightarrow J_0\left(a\sqrt{t^2-k^2}\right)U(t-k), \qquad k \geq 0 \qquad (4.13)$$

The factors s and $1/s$ in (4.11) and (4.12) transform to differentiation and integration operations respectively. The corresponding time-domain responses are therefore

$$f_{TEnm}(t) = \delta(t-z/c) - \omega_{nm} t\, U(t-z/c) \frac{J_1\left(\omega_{nm}\sqrt{t^2-z^2/c^2}\right)}{\sqrt{t^2-z^2/c^2}} \qquad (4.14)$$

$$f_{TMnm}(t) = \delta(t-z/c) - \omega_{nm} t\, U(t-z/c) \frac{J_1\left(\omega_{nm}\sqrt{t^2-z^2/c^2}\right)}{\sqrt{t^2-z^2/c^2}}$$

$$+\omega_{nm}^2 \int_0^t U(\tau-z/c) J_0\left(\omega_{nm}\sqrt{\tau^2-z^2/c^2}\right) d\tau \qquad (4.15)$$

Note that the first two terms in these equations are identical, and only the extra integral term in the TM mode response distinguishes it from the TE mode. To generate the response plots at distances of z=1, 2, 4 and 8m shown in Figure 4.8, equations (4.14) and (4.15) have been normalised to a cut-off frequency of 1Hz ($\omega_{nm} = 2\pi$) with a propagation velocity 1m/s substituted for c. The initial Dirac impulse terms are not shown. The integral in (4.15) was evaluated numerically, and its effect is to cause the TM mode response to decrease in amplitude more rapidly than the TE mode.
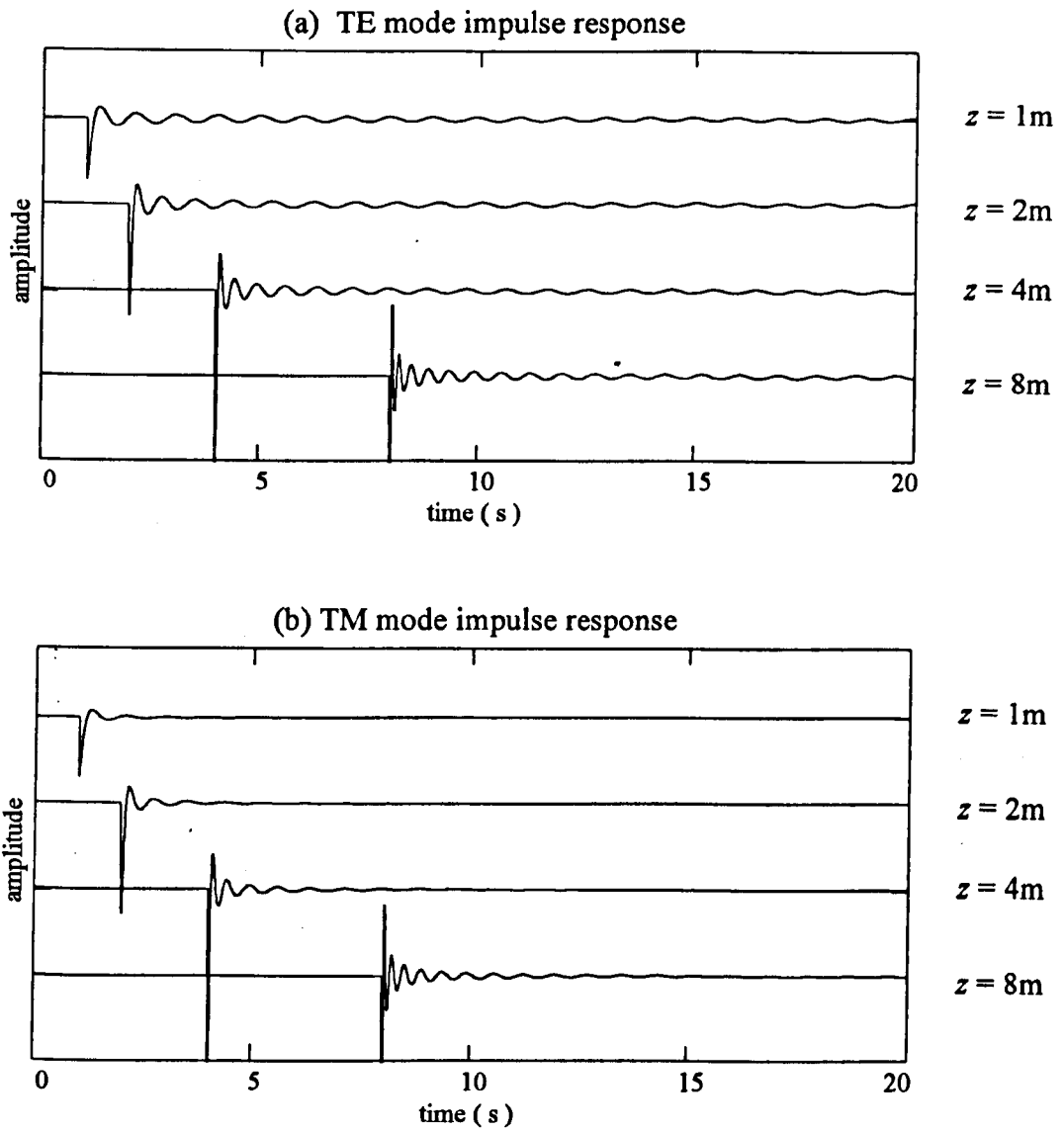
Figure 4.8   Normalised electric field responses to a current impulse in the
waveguide at various distances *z* from the source.
(a) TE mode, and (b) TM mode types.

The functions are well behaved except when $t = z/c$. At this instant the first term is a positive impulse and the second term contributes a step from zero to a negative value, since $\lim\limits_{x \to 0} \{J_1(kx)/x\} = k/2$. In practice this discontinuity does not appear in the output signal and this can be explained as follows. The group velocity of propagation in a waveguide for a signal of instantaneous frequency ω in a mode with cut-off frequency ω_{nm} is

$$v_g = c\sqrt{1 - \left(\omega_{nm}/\omega\right)^2} \qquad (4.16)$$

so that only signals of infinite frequency can propagate over a distance z in time $t = z/c$. In any real bandlimited system, the maximum frequency is finite, so that the response to a pulse will always begin a short time after $t = z/c$.

The instantaneous frequency of the impulse responses defined by (4.14) and (4.15) begins at a high value and decays towards the mode cut-off frequency. The signal arriving after the initial wavefront is therefore tending towards an entirely transverse resonance in the waveguide at its cut-off frequency. For a detailed analysis of the instantaneous frequency, refer to [60].

4.3.2 Sensitivity functions

The amplitude of the radial electric field *Er* at the coupler is dependent on the location of the PD source in the transverse plane. This can be demonstrated by defining a small PD source of constant path length Δr and plotting the variation of those terms in the transfer functions (4.9) and (4.10) which do not depend on ω. These functions will be referred to as the *sensitivity functions* for the waveguide

modes. By setting $r_1 = r - \Delta r/2$ and $r_2 = r + \Delta r/2$ we can define the following sensitivity functions for TE and TM modes:

$$S_{TEnm}(r, \phi) = K_{TEnm} \int_{r - \Delta r/2}^{r + \Delta r/2} \frac{J_n(q_{nm} r'/a)}{r'} dr' \cos(n\phi) \qquad (4.17)$$

$$S_{TMnm}(r, \phi) = K_{TMnm} \left[J_n\left(\frac{p_{nm}(r + \Delta r/2)}{a}\right) - J_n\left(\frac{p_{nm}(r - \Delta r/2)}{a}\right) \right] \cos(n\phi) \qquad (4.18)$$

The effect of PD source location can be displayed as a three-dimensional plot of S in the (r, ϕ) plane. Two examples are shown in Figure 4.9, generated by setting $\Delta r = 0.01$m for the TE_{11} and TM_{21} modes. The cross-section through the circular waveguide can be used to select a location for the PD source, and the height of the surface at that point gives the relative amplitude of the radial electric field at the coupler due to mode in question. The sensitivity functions should not be used to compare the contributions from different modes because the cut-off frequencies also affect the field strength.

4.3.3 Response to a Gaussian pulse

To simulate the chamber response to a real current pulse, the fast component of the PD pulse can be approximated by a Gaussian shape, defined in the time- and frequency-domains by

$$i(t) = I_0 e^{-t^2/2\sigma^2} \qquad (4.19)$$

$$I(\omega) = I_0 \sigma \sqrt{2\pi} e^{-\sigma^2 \omega^2/2} \qquad (4.20)$$

respectively, where I_0 is the peak value of the current occurring at $t=0$, and the pulse width is defined by the parameter σ. The form of the impulse response expressions given by (4.14) and (4.15) precludes analytical solution of the convolution integral

(a) S_{TE11}
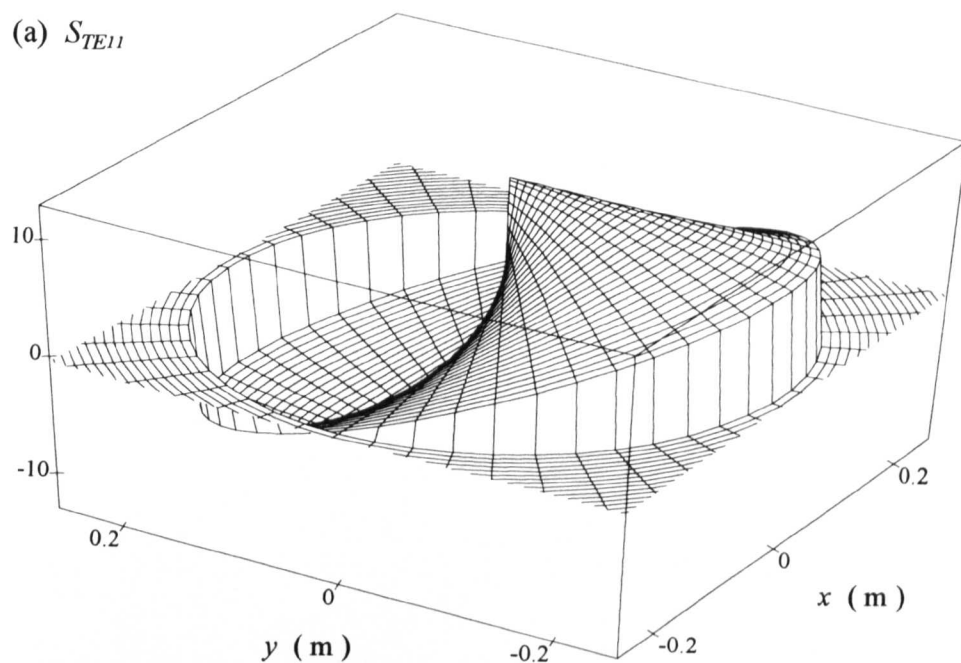
(b) S_{TM21}
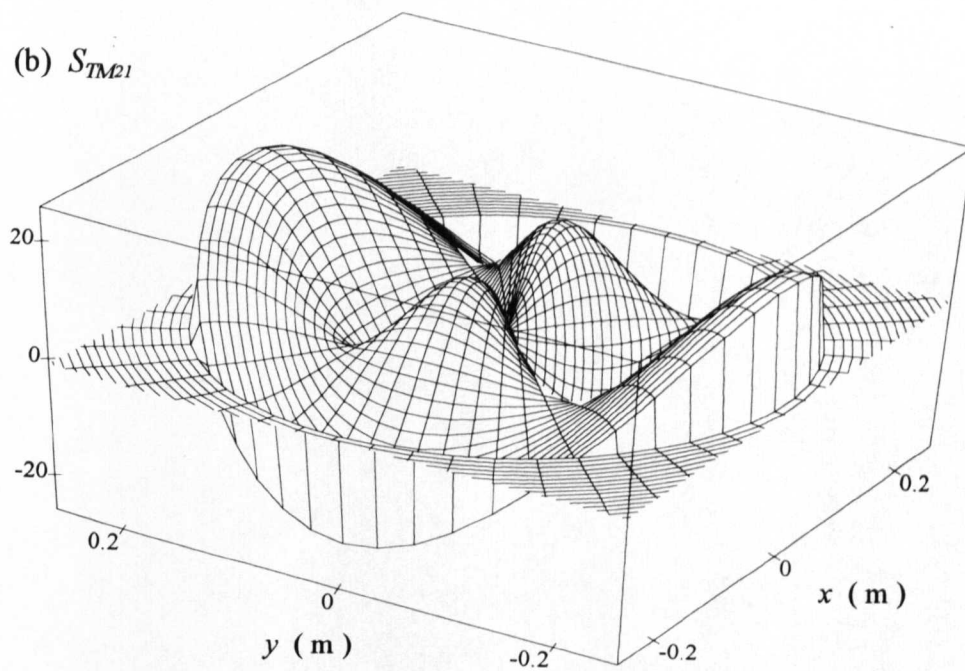
Figure 4.9   Variation of the sensitivity functions over the waveguide cross-
section. The polar co-ordinates r and ϕ have been mapped onto a
Cartesian x-y plane to produce these plots. The line corresponding to
$\phi=0$ is defined as the positive y-axis.   (a) TE_{11} mode,   (b) TM_{21} mode.

with $i(t)$ to determine the response to a Gaussian pulse. Similar difficulties arise with inverse Fourier transformation of the frequency-domain product $I(\omega)F(\omega)$. Therefore an alternative method was used to arrive at a reasonable expression for the Gaussian response. The time taken for a signal of instantaneous frequency ω to travel a distance z along the waveguide is found from (4.16) to be

$$t = \frac{z}{c\sqrt{1 - (\omega_{nm}/\omega)^2}} \tag{4.21}$$

Rearranging, the instantaneous frequency of the signal arriving at distance z can be expressed as a function of time by

$$\omega^2 = \frac{\omega_{nm}^2}{1 - (z/ct)^2} \qquad \text{for } t \geq z/c \tag{4.22}$$

For a current impulse, all instantaneous frequencies have equal weighting, resulting in the impulse responses of (4.14) and (4.15). For a Gaussian pulse, however, the frequency weighting is given by (4.20). If (4.22) is substituted into (4.20), we obtain a weighting function in the time-domain,

$$W_{nm}(t) = I_0 \, \sigma \sqrt{2\pi} \, e^{-\frac{\sigma^2}{2}\left(\frac{\omega_{nm}^2}{1-(z/ct)^2}\right)} \qquad \text{for } t \geq z/c \tag{4.23}$$

which can be used to modify the envelope of the impulse response. As $t^+ \to z/c$, $W_{nm}(t) \to 0$, forcing the response to increase smoothly from zero at $t = z/c$.

As $t \to \infty$, $W_{nm}(t) \to I_0 \, \sigma \sqrt{2\pi} \, e^{-\frac{1}{2}\sigma^2 \omega_{nm}^2}$, which is a constant equal to the amplitude of the pulse spectrum at the mode cut-off frequency. $W_{nm}(t)$ is plotted in a

normalised form in Figure 4.10 for various distances from the source corresponding to those used in Figure 4.8. The proposed Gaussian pulse response expressions are

$$Erg_{TEnm}(t) = K_{TEnm} \int_{r_1}^{r_2} \frac{J_n(q_{nm}r'/a)}{r'} dr' \cos(n\phi) W_{TEnm}(t) f_{TEnm}(t) \qquad (4.24)$$

$$Erg_{TMnm}(t) = K_{TMnm} \left[J_n(p_{nm}r_2/a) - J_n(p_{nm}r_1/a) \right] \cos(n\phi) W_{TMnm}(t) f_{TMnm}(t)$$

$$(4.25)$$

for the TE and TM mode radial electric fields. To investigate the accuracy of these expressions, they can be compared with results from numerical convolution of $i(t)$ given by (4.19) and the time-domain mode impulse response. For example, in Figure 4.11(a) the TE_{11} mode response predicted by (4.24) is compared with a numerical computation of $K_{TE11} \{ i(t) \otimes f_{TE11} \}$ over a period covering the first 20ns of the signal. Agreement is very good, except in the immediate region of $t = z/c$. For times shortly after $t = z/c$ the responses cannot be distinguished. The finite sampling rate in the numerical calculation causes inaccuracy near the discontinuity in the impulse response. Figure 4.11(b) shows an expanded view of the initial response, in which the sampling rate for the convolution calculation has been increased by a factor of ten. Much of the difference evident in Figure 4.11(a) has disappeared, revealing the cause to be undersampling in the region of the discontinuity. In Figure 4.11(b) the numerical procedure correctly predicts a response occurring before $t = z/c$, since the Gaussian input pulse is non-zero before $t = 0$. The small remaining discrepancy confined to the region $t = z/c \pm \sigma\sqrt{2\pi}$ can be neglected when its duration is compared to that of the entire UHF signal. The similarity between the shape of the predicted responses (Figure 4.11) and the transients observed in waveguides [61,62] provides further support for the usefulness of the Gaussian approximations.
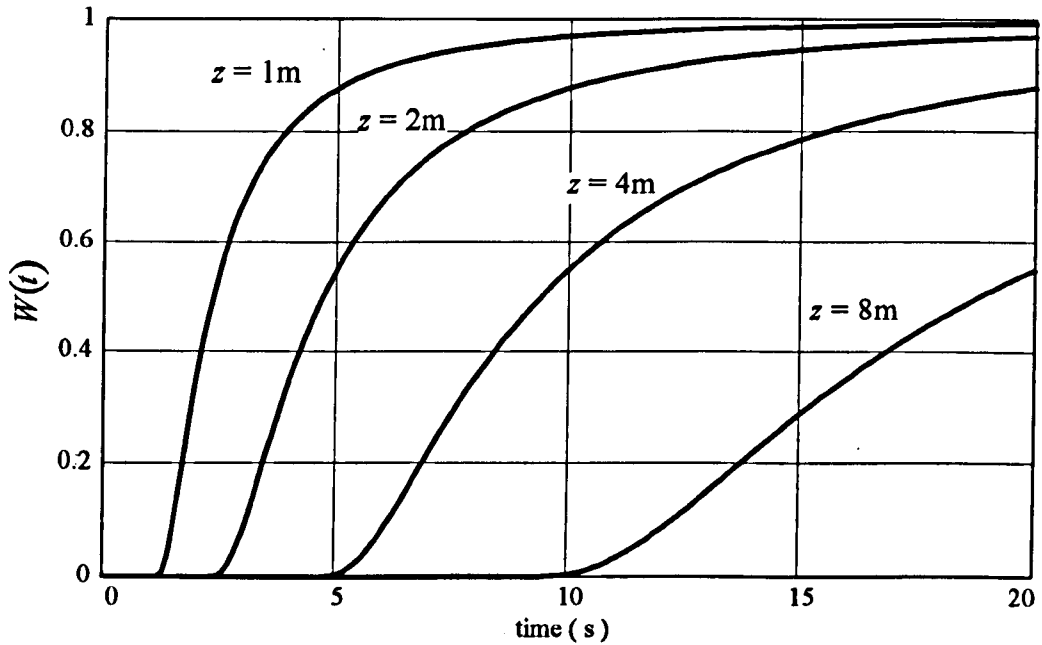
The normalised amplitude weighting function is defined by:

$$W(t) = k \, e^{-\frac{\sigma^2}{2}\left(\frac{\omega_c^2}{1-(z/ct)^2}\right)}$$

where

$$\omega_c = 2\pi \text{ radians/s,}$$

$$\sigma = 1/\sqrt{2\pi},$$

$$k = e^{\frac{1}{2}\sigma^2\omega_c^2} = e^{\pi}$$

and the velocity c has been normalised to 1m/s.

Figure 4.10   Plots of the normalised amplitude weighting function, at various propagation distances z.
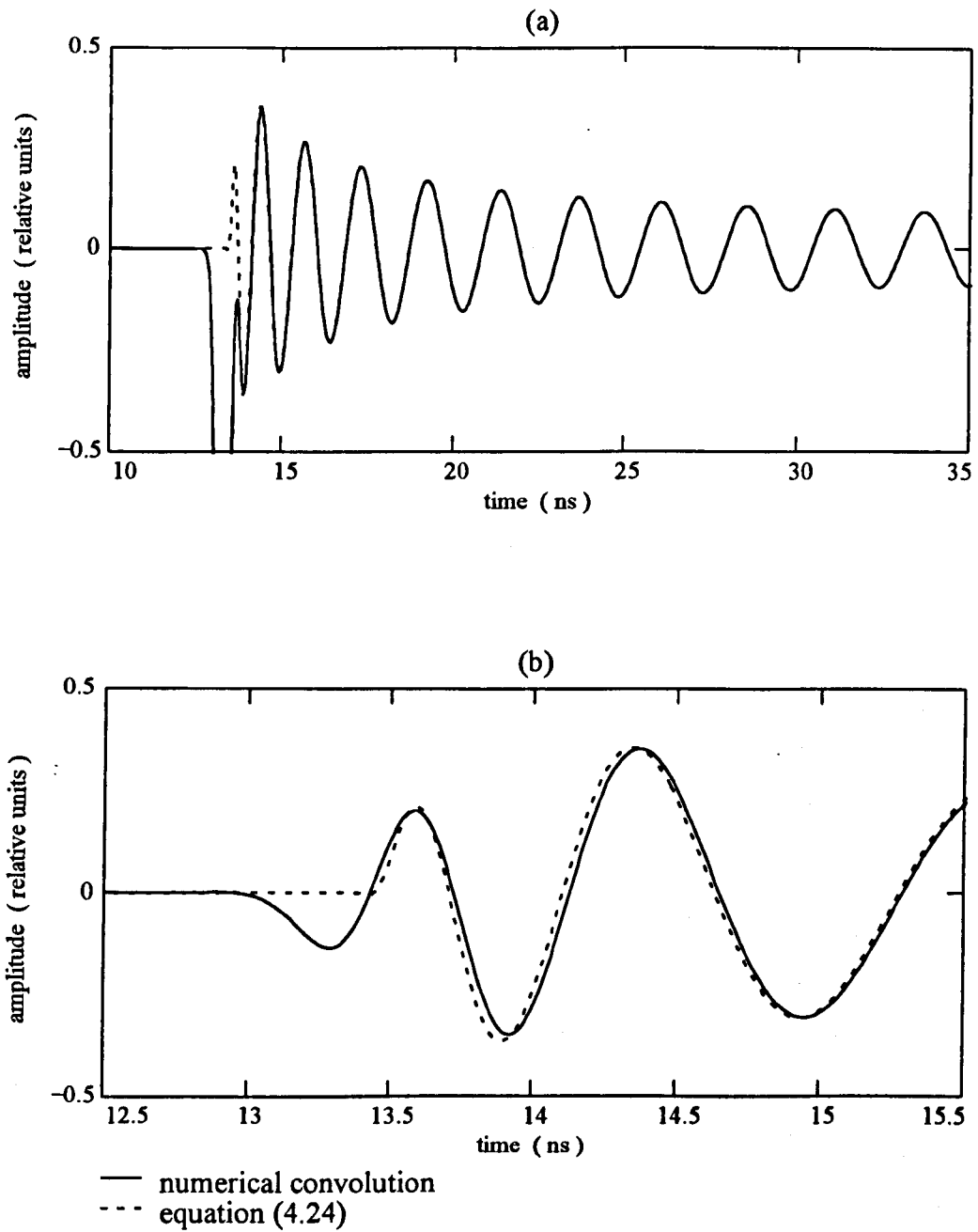
Figure 4.11 Comparison of the TE_{11} mode Gausssian pulse response predicted by numerical convolution and the analytical approximation of (4.24) at z=4m, with σ=175ps. (a) An effective sampling rate of 24 Gsamples/s used in the numerical procedure, and (b) an expanded view of the initial response using a sampling rate of 240 Gsamples/s.

4.3.4 Description of the simulation process

The contributions to the UHF electric field from each mode are generated separately using the cut-off frequencies and eigenvalues given in Table 4.2. Values for I_0 and σ are obtained by making a Gaussian approximation to the input pulse. K_{TEnm} and K_{TMnm} are calculated from the waveguide dimensions and the eigenvalues. The functions of the transverse co-ordinates in (4.24) and (4.25) are evaluated using the known endpoints r_1 and r_2 of the radial current path and the angle ϕ between the source and coupler. Finally, the propagation distance in the z-direction is defined and sampled records of the electric field at the coupler position are generated using Mathcad to implement equations (4.24) and (4.25).

Figure 4.12 shows a simple 10mm radial PD current path at the outer conductor, located at $z=0$ in an infinite uniform circular waveguide. The current pulse is Gaussian, with $\sigma=175$ps giving a half-amplitude pulse width of 460ps which is typical of the measured and simulated PD pulses. The peak current $I_0=2.28$mA was chosen to give a charge transfer of $q = \sigma I_0 \sqrt{2\pi} = 1$pC. Two positions for monitoring the resulting UHF electric field are indicated by the letters A and B, at distances of 4m and 10m from the PD source in the z-direction. The individual mode contributions to the radial electric fields at points A and B are shown in Figures 4.13 and 4.14 respectively, demonstrating how the total field is built up by superposition. Contributions from nine of the modes listed in Table 4.2 are illustrated, and the resultant signal can be seen to take on the more random appearance of typical the UHF signals observed in GIS. At point A, the combined amplitude of the electric field is about 35mV/m peak-to-peak. This value indicates the very low intensity of the UHF electric field when compared with the power frequency fields that are typically a factor of 10^8 larger.

To simulate the response of the test chamber shown in Figure 4.1, reflections at the end plates must be taken into account. If the endplates are taken to be perfectly
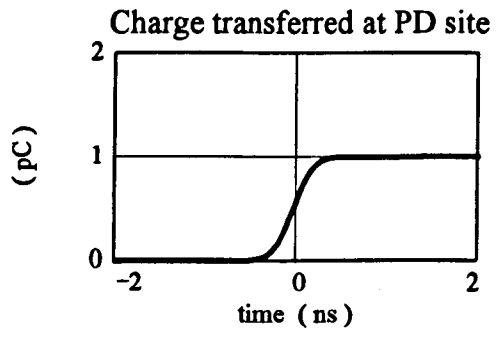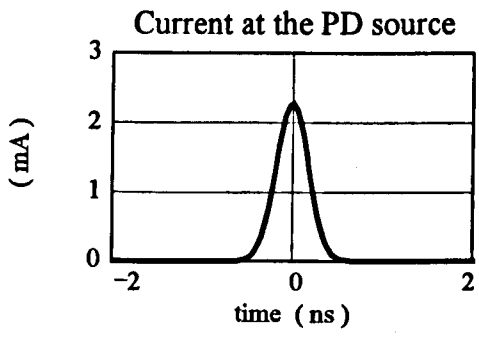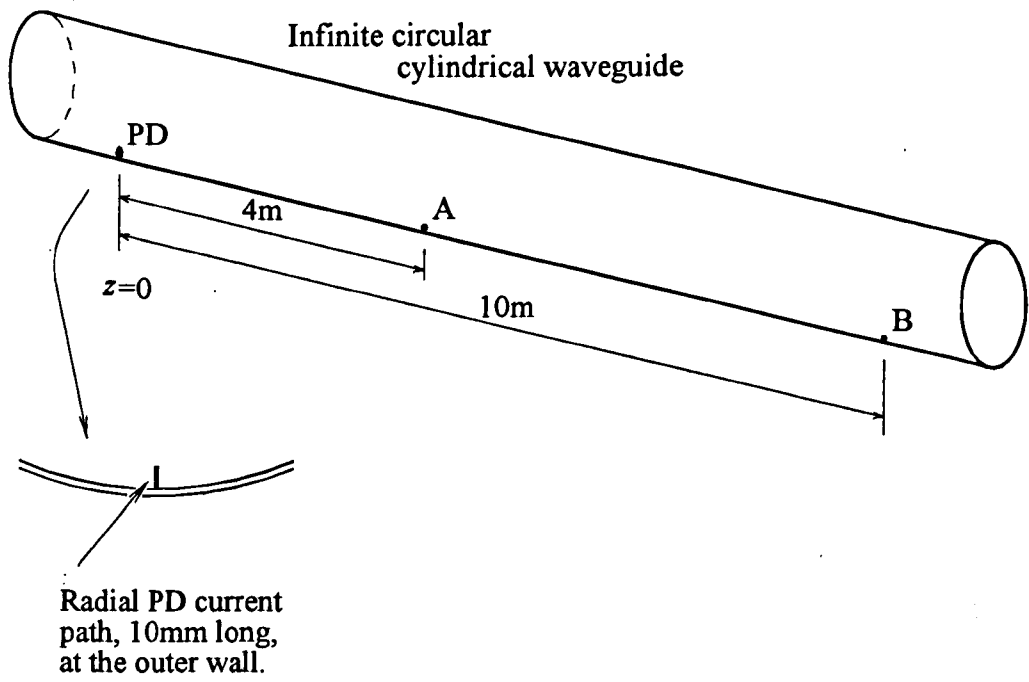
Figure 4.12   The simulated configuration and current pulse used to
generate the UHF field results shown in Figures 4.13 and 4.14.
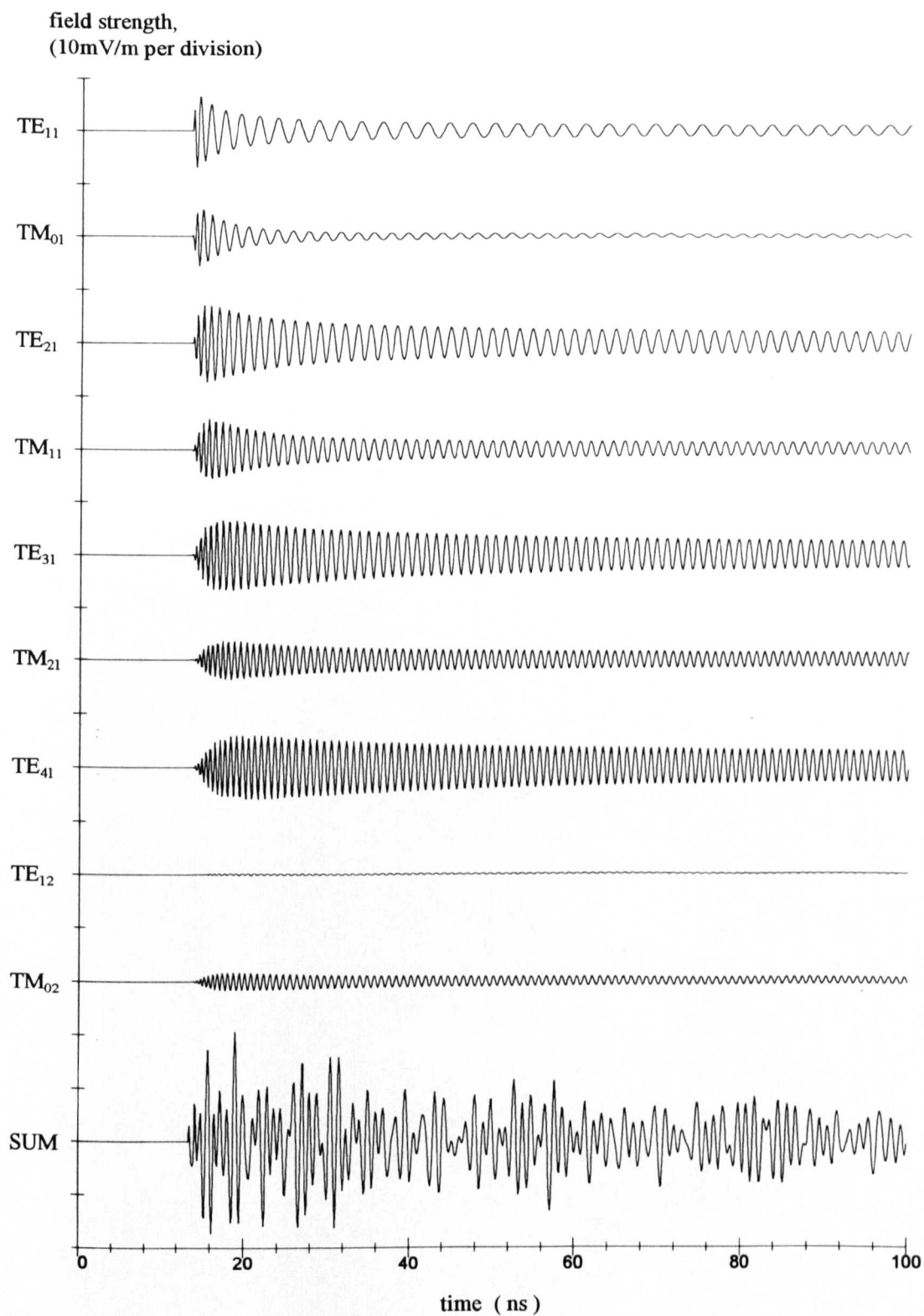
Figure 4.13 Contributions of nine modes to the radial electric field at point A in Figure 4.12, a distance of $z=4$m from the source. Calculated using the Gaussian approximation for a 1pC current pulse, a 10mm PD path at the waveguide wall, with $\sigma=175$ps and $\phi=0$.
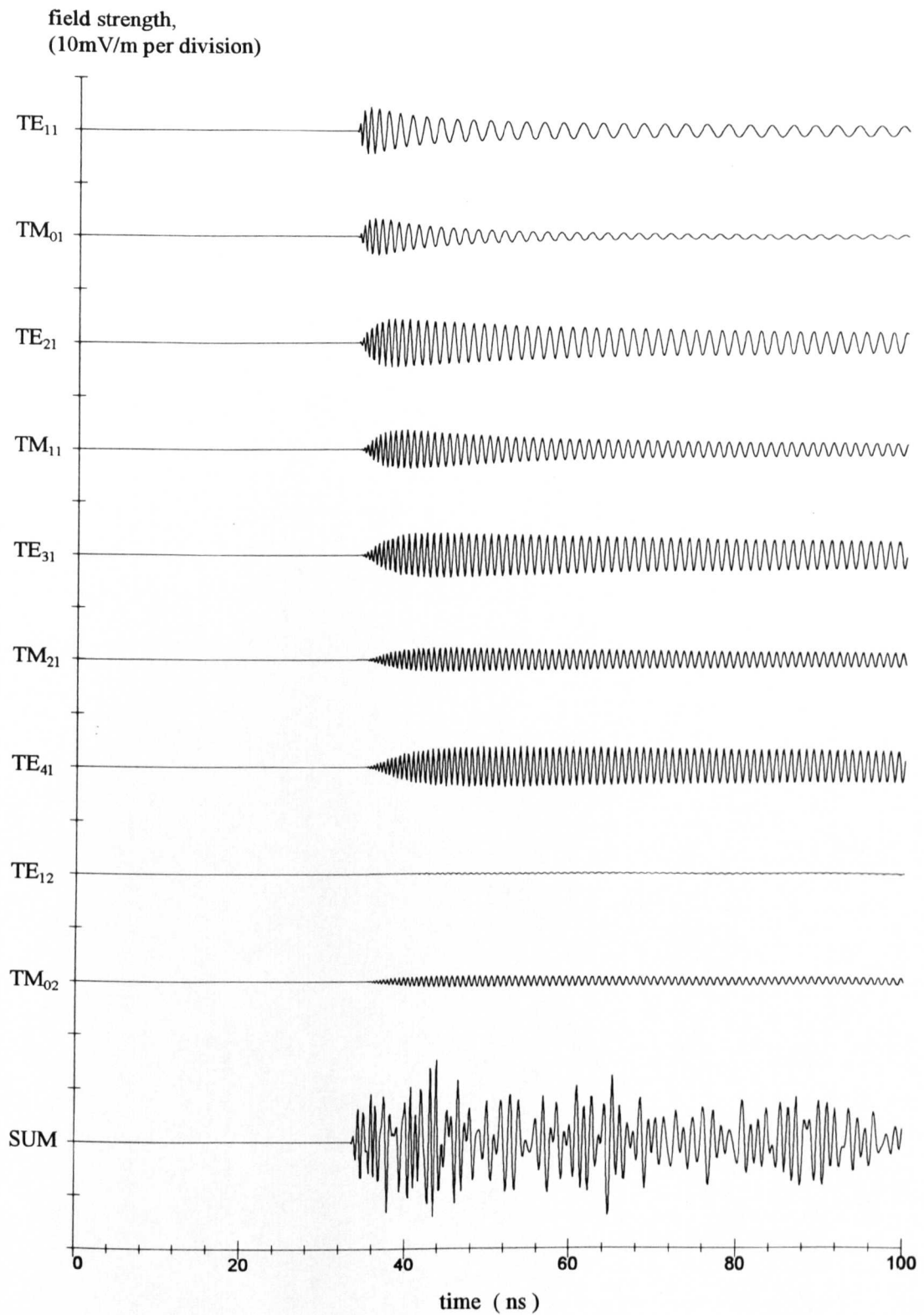
Figure 4.14 Contributions of nine modes to the radial electric field at point B in Figure 4.12, a distance of z=10m from the source. Calculated using the Gaussian approximation for a 1pC current pulse, a 10mm PD path at the waveguide wall, with σ=175ps and ϕ=0.

91

conducting, then *Er* must vanish on this surface. The reflected signal therefore has a radial field component that is reversed in polarity. The simulation period was limited to 40ns. At this time, the maximum propagation distance at velocity *c* is 12m. All the signal paths from source to coupler that are shorter than 12m are shown in Figure 4.15. The contributions to the radial field from signals that have undergone an odd number of reflections at the end plates are reversed in polarity. The propagation distances and polarities of the various signal paths used in the simulation are summarised in Table 4.3.

Table 4.3

List of the reflection paths used in the simulation of the UHF signal

in the test chamber of Figure 4.1.

Distance travelled by the signal (metres)	Polarity of the contribution to the total radial electric field
1.5	+
2.1	-
5.1	-
5.7	+
8.7	+
9.3	-

Contributions to the electric field from the fifteen modes listed in Table 4.2 at each of the six distances listed in Table 4.3 were combined and stored as a 512 point record of *Er* at an equivalent sampling rate of 12.8GHz to be comparable with the digitised experimental data. The output voltage of the probe coupler given by equation (4.4) was obtained by numerical differentiation of the *Er* record. To allow direct comparison between simulation and measurement, the signals recorded on the digitiser must be corrected for the gain of the measurement system. The measured
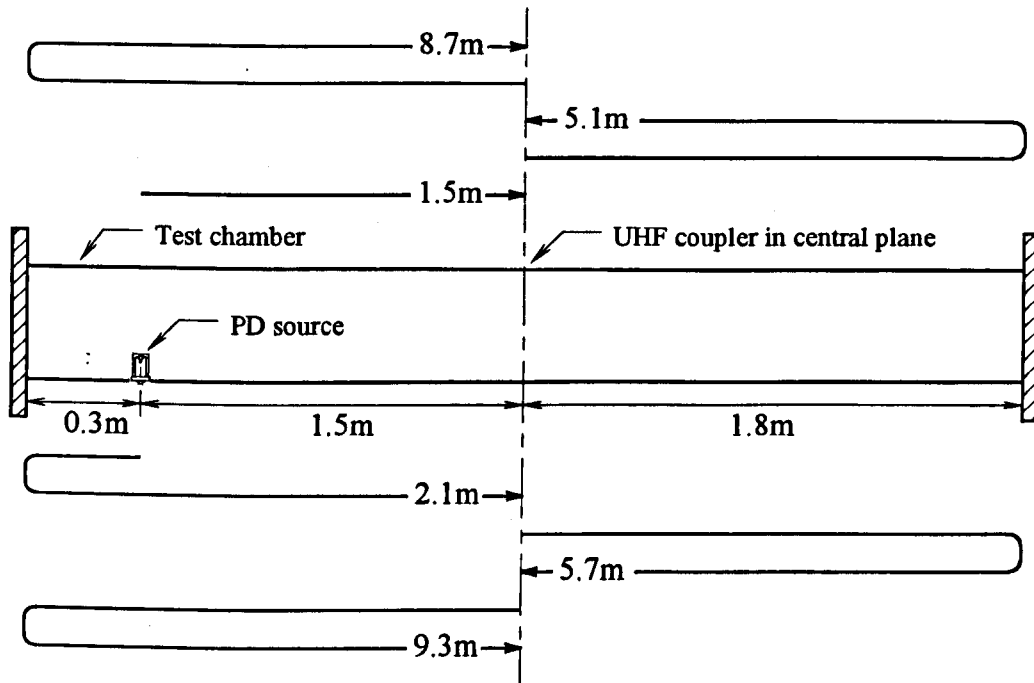
Figure 4.15   Signal paths up to 12m in length between source and coupler
in the experimental chamber. The PD source is located 0.3m
from one end of the chamber and the coupler is located in the
central plane.

voltage gain was 25 at 350MHz, decreasing to 10 at 1500MHz. As a first order approximation, the results were scaled by a frequency independent voltage gain of 20, which was the measured value at the centre of this band.

4.4 Results

4.4.1 Simulated PD on a probe

As described in Section 4.2.3, the corrected half-amplitude width of the current pulse on the probe is 460ps, giving a value of σ=175ps for the Gaussian approximation. Using (4.8) to determine the average current over the length of the probe from the peak current of 1.79mA flowing into its base gives I_0=1.14mA. Integration of this Gaussian pulse results an equivalent charge transfer along the probe of

$$q = \sigma I_0 \sqrt{2\pi} = 0.5pC \qquad (4.26)$$

This value indicates the low level of the PD simulated by the probe. Typically, a detection level of 1pC apparent charge is the best that can be achieved using conventional PD detection systems.

When the 30mm probe of Figure 4.2 is mounted at the outer conductor its endpoints are defined by r_1=0.220m and r_2=0.250m. The UHF signal from the probe coupler is compared with the simulated probe output voltage in Figure 4.16 for a coupler angle of $\phi = 0$ and in Figure 4.17 for a coupler angle of $\phi = \pi/2$. For the results shown in this section, the UHF signals have been shifted in time to ensure that the PD current pulse is always centred on t=0. With reference to Figure 4.15, the shortest path between source and coupler is seen to be 1.5m. This corresponds to a delay of 5.0ns at velocity c, which can be seen in the experimental results.
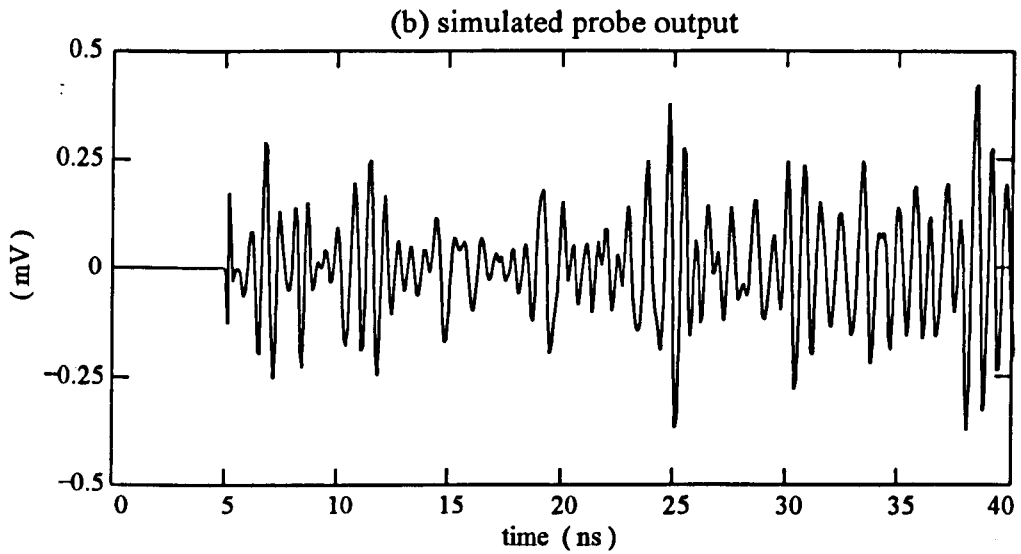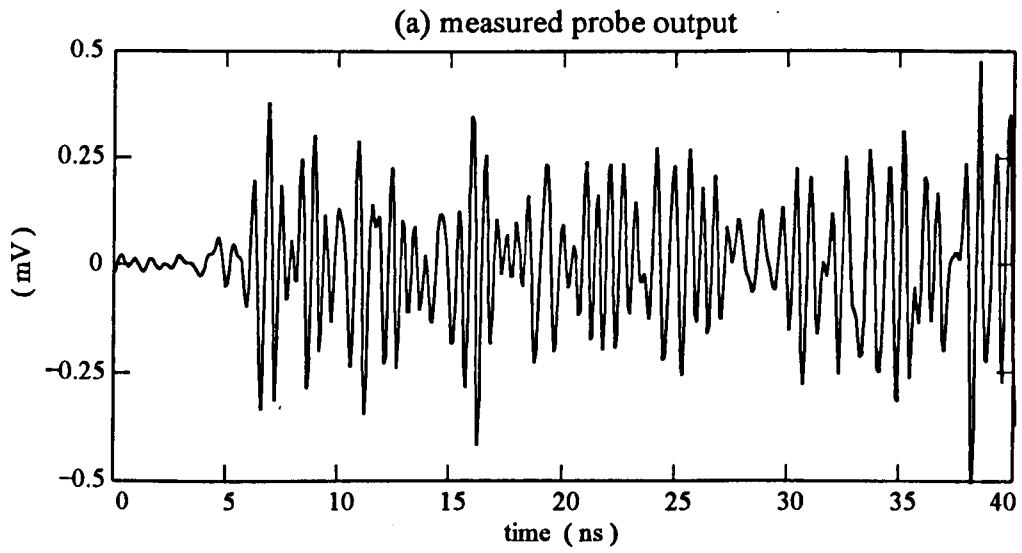
Figure 4.16   Output voltage of the probe coupler for a 0.5pC excitation of the test chamber, with φ=0.
(a) Measured voltage, (b) simulated voltage.
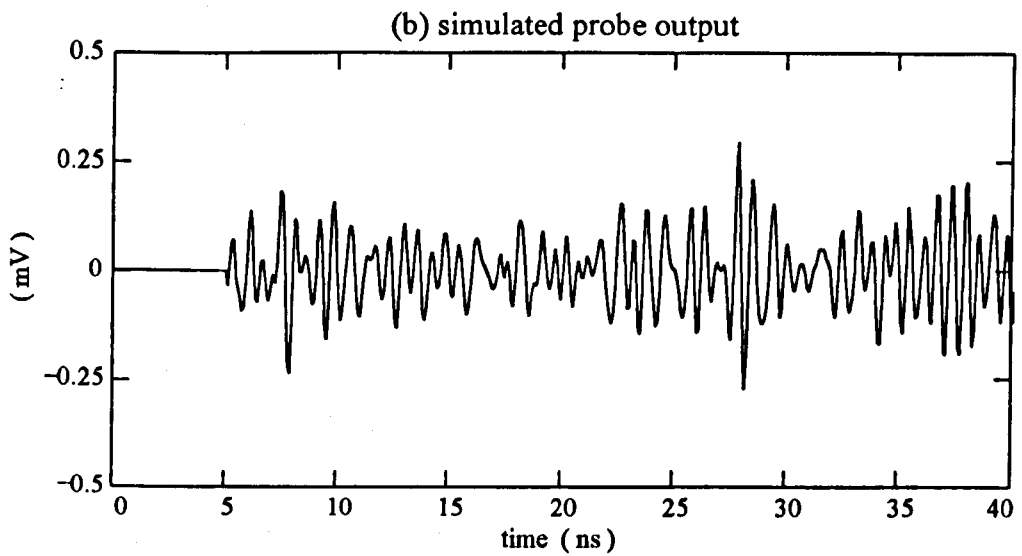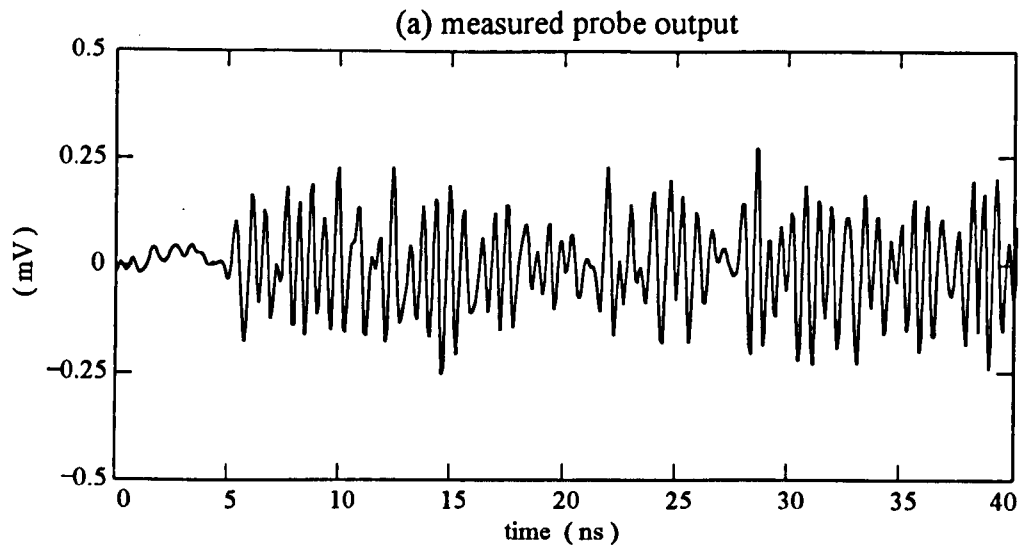
Figure 4.17   Output voltage of the probe coupler for a 0.5pC excitation of the
test chamber, with φ=π/2.
(a) Measured voltage, (b) simulated voltage.

Exact agreement between individual cycles of the UHF signal cannot be expected, due to the number of approximations used in the model, particularly those relating to the frequency responses of the probe coupler and measurement equipment. However, UHF monitoring of PD is usually achieved by detecting the signals using a high frequency rectifier and integrating to obtain the pulse envelope. This system is essentially responsive to the energy level of the UHF signal, which corresponds to the integral of its power. Therefore a useful alternative method for comparing measured and simulated signals is that shown in Figure 4.18, where the cumulative energy delivered to the load Z_L=50Ω calculated according to

$$e(t) = \frac{1}{Z_L} \int_0^t v^2(\tau) d\tau \qquad (4.27)$$

is plotted against t. By comparing the calculated energy levels for the measured and simulated signals over the same time interval, the level of agreement can be assessed. This method of comparison will be used for the remainder of the results presented in this chapter. At the end of the 40ns period in Figure 4.18, the simulated energy is 64% of the measured energy when $\phi = 0$ and 67% when $\phi = \pi/2$.

Changing the amplitude of the current pulse produced a variation in the UHF signal level that was directly proportional to I_0, as predicted by the theory. This is an inevitable consequence of the system linearity that has been observed previously [41], so the results are not included here.

4.4.2 PD on the needle

For the PD cell (Figure 3.1), the length of the current filament in the gas is small compared to the needle lengths used. The excitation current has a constant amplitude along the needle so there is no need to make a correction for the average current in
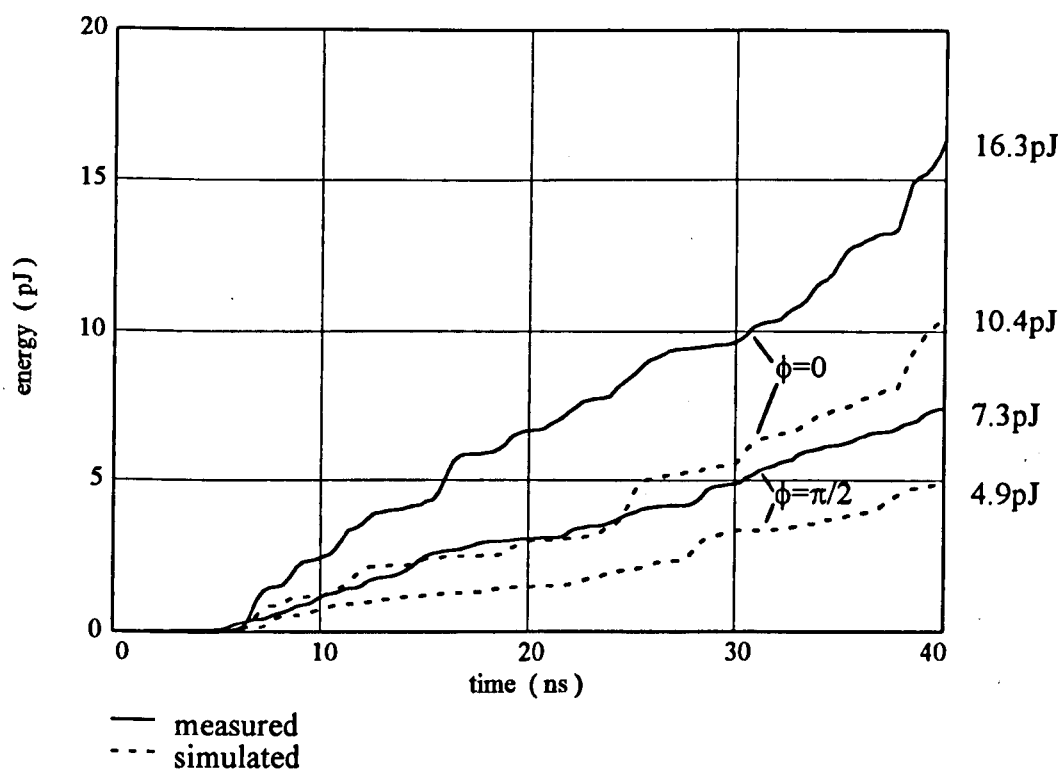
Figure 4.18   Comparison of the measured and simulated UHF energies at two angles for the 0.5pC pulsed probe excitation results of Figures 4.16 and 4.17.

this case. PD is recorded as a voltage generated across the input impedance of the measurement system, from which the current pulse is derived after correction for the limiting effect of the digitiser step response. Values for I_0 and σ are then assigned to the Gaussian model of the pulse. A value of $\sigma=175$ps was used for all the results presented here. This allowed a good match to the pulse shapes while avoiding the need to generate separate sets of mode simulation data for each pulse. When the PD cell is mounted in the chamber, the metal base raises the needle 15mm above the chamber wall. The endpoints of the current path are therefore $r_1=0.205$m, $r_2=0.235$m for the 30mm needle and $r_1=0.220$m, $r_2=0.235$m for the 15mm needle.

The total charge transferred along the needle during the pulse will be referred to as the PD magnitude q, and is calculated using (4.26). The following results illustrate the effects of q, the needle length ℓ and the coupler angle ϕ on the UHF signal. Simulated and measured energies are compared in each case. The records of the measured signals shown are less than 20ns in duration because the first part of the trace was used to capture the PD pulse, although this is not shown in the figures. After time shifting so that the pulse is centred on $t=0$, the UHF signal record ends at around $t=18$ns.

- Figure 4.19 compares UHF energies for two different PD pulses on the 30mm needle of magnitudes 1.2pC and 4.5pC.

- Figure 4.20 compares UHF energies for similar PD pulses of magnitude 1.2pC on the 15mm and 30mm needles.

- Figure 4.21 compares UHF energies for similar PD pulses of magnitude 1.6pC on the 15mm needle for coupler angles $\phi = 0$ and $\phi = \pi/2$.
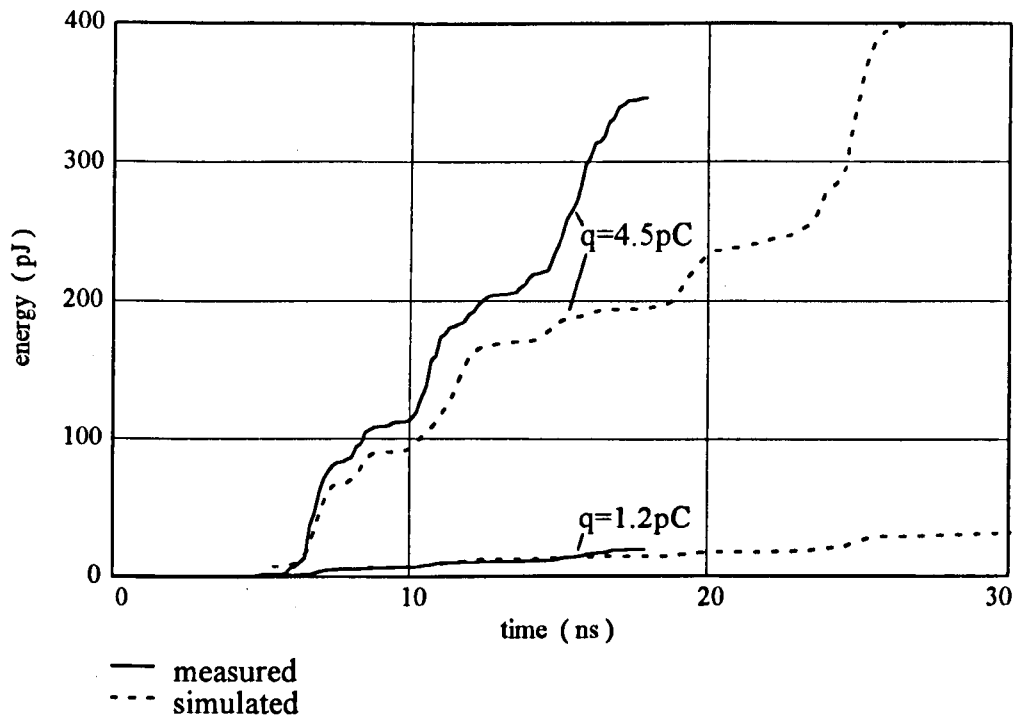
Figure 4.19   Measured and simulated UHF energies for PD pulses of
different magnitudes on the 30mm needle.
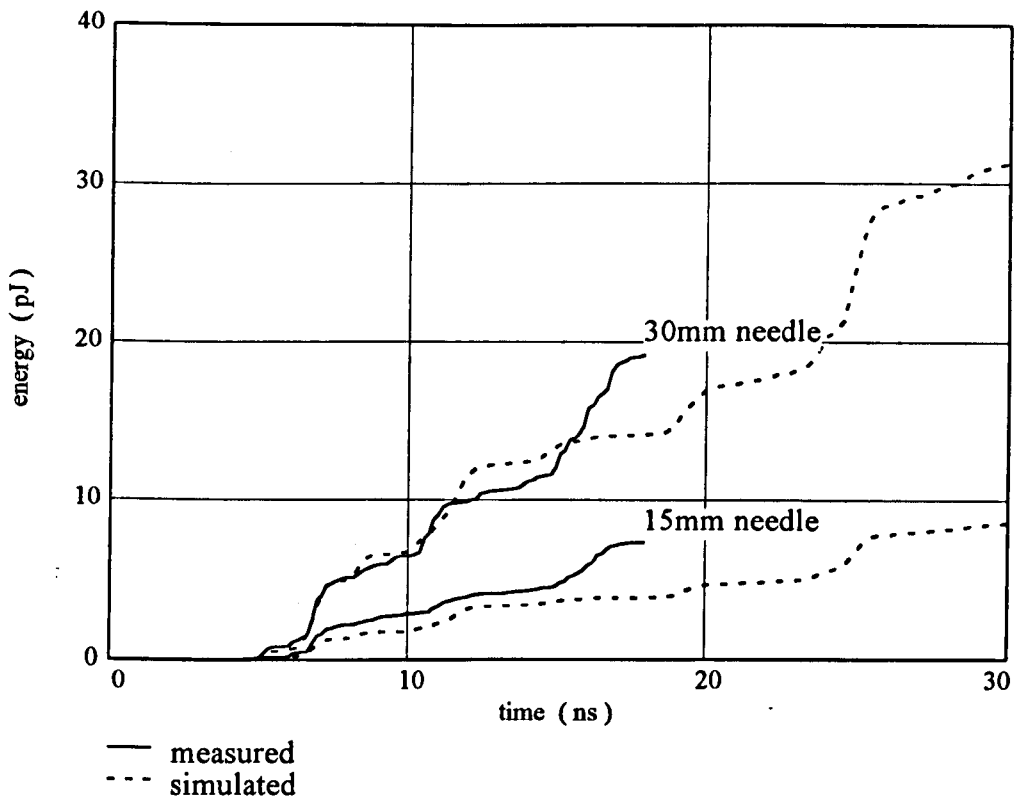
Figure 4.20   Measured and simulated UHF energies for PD pulses on
the 30mm and 15mm needles.
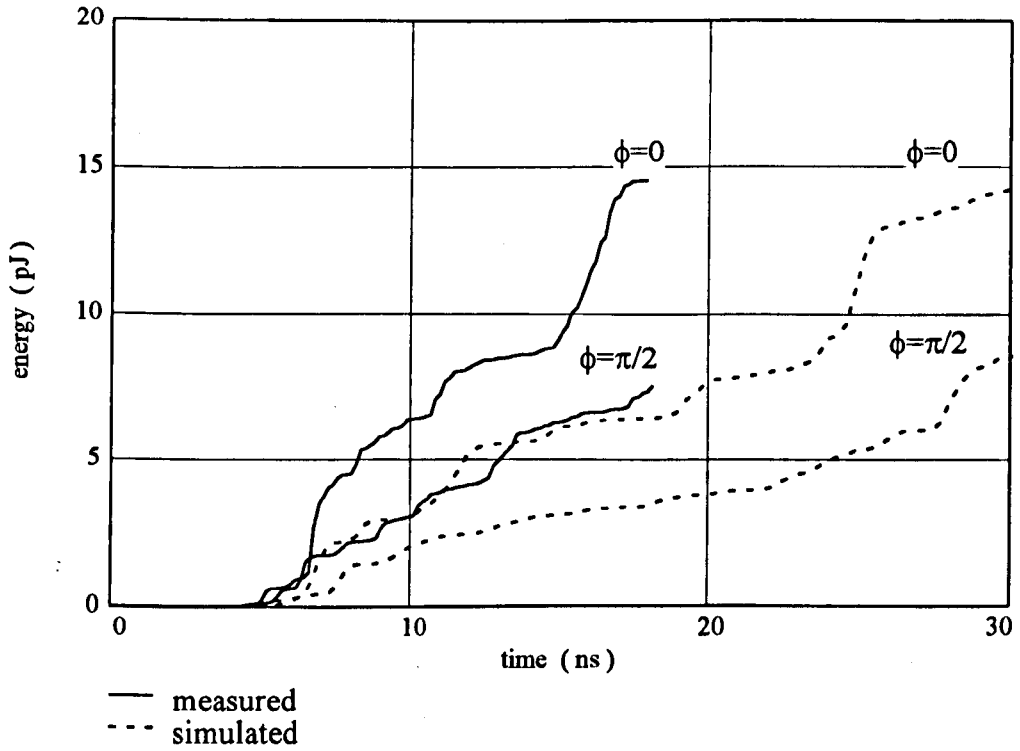
Figure 4.21   Measured and simulated UHF energies at two coupler angles relative to the 15mm needle PD source.

4.5 Discussion

4.5.1 Accuracy of results

Closest agreement between predicted and measured changes in the UHF signal occurred with the simulated PD. When the needle PD cell was used, the current pulse shape was never exactly maintained as the other parameters were varied. The possibility of additional excitation of UHF signals by coupling of the PD pulse onto the HV cable was considered. However, an RF blocking coil connected between the cable and the HV electrode made no difference to the UHF signal. This is because the capacitance between the needle tip and the HV electrode is so small that capacitive coupling of the pulse is negligible. Nevertheless, the cable may act as a transducer within the chamber, coupling energy from one mode to another, and the cell itself is a more significant intrusion into the ideal hollow chamber than the simple monopole.

The UHF energy determined by the simulation process is proportional to C_e^2 and is therefore very sensitive to inaccuracy in this quantity. The value of C_e used was obtained from data relating to a monopole protruding through a flat ground plane. When mounted in the cylinder, curvature of the walls must increase this capacitance, so the value used in the model will be smaller than the actual capacitance. On average, the results show a simulated energy that is 60% of the measured energy. An underestimation of 23% in the value of C_e would be required to cause this discrepancy. Together with the simplified model of the measurement equipment response, this is sufficient to account for the difference between simulated and measured energies apparent in Figures 4.18 - 4.21. The more important aspect of these results is the accuracy with which relative changes in the UHF signal level are predicted when the parameters of the experiment are varied. This information is summarised in Table 4.4, based on the results presented above.

Table 4.4

Summary of the measured and simulated effects on the UHF energy

of changes in the experimental parameters.

Results shown in Figure	Parameter altered	Range of variation	Simulated variation in energy Δ_1	Measured variation in energy Δ_2	Ratio $\sqrt{\dfrac{\Delta_1}{\Delta_2}}$	Difference between simulation and measurement
4.18	Coupler angle ϕ, simulated PD	$0 \rightarrow \pi/2$	0.48	0.46	1.02	+2%
4.19	Pulse magnitude q, real PD	$\times 3.7$	13.80	17.50	0.89	-11%
4.20	Needle length ℓ, real PD	$\times 2.0$	3.64	2.63	1.18	+18%
4.21	Coupler angle ϕ, real PD	$0 \rightarrow \pi/2$	0.59	0.52	1.07	+ 7%

4.5.2 Evaluation of the simulation technique

The time-domain technique has been used to simulate the UHF signals excited by PD within a waveguide structure. While the measured and simulated UHF signals are not identical, the energy levels are closely comparable, and differences can be explained by the considerable simplifications involved in deriving the analytical time-domain model. The amplitude of the simulated signal was, on average, only 23% less than the measured signal when calculated as the square root of the energy ratio. Furthermore, the effects of changes in PD pulse amplitude, path length and coupler angle on the UHF signal predicted using the theory were found to be within 20% of experimental observation. Given that the differences between simulation and experiment are primarily due to simplifications in the field measurement model, the

following effects of the PD source parameters on the UHF signal are predicted by the theory:

- The UHF signal is proportional to the charge q transferred during the PD pulse if all other factors remain constant.

- The amplitude of each mode is dependent on the radial location of the PD current path in a non-linear manner.

- The amplitude of each mode also varies non-linearly with the length of the current path. However, for path lengths that are small compared to the waveguide radius, the Bessel functions that define the mode sensitivity functions will change little over the PD path. Under these conditions, the amplitude of the UHF signal is proportional to the length ℓ of the PD current path. This suggests that for small PD sources, the UHF signal amplitude is proportional to the product $q\ell$ for a fixed pulse shape and defect location.

- The effect of the angle between the source and the coupler is to alter the ratio in which the modes are combined, due to the $cos(n\phi)$ amplitude variations. For example, signals propagating in even order modes will be in phase at diametrically opposing locations, whereas signals in odd order modes will be in antiphase.

The correct method for simulation of PD pulses on a protrusion has been demonstrated, and compares well with measurements of real PD on the needle both in terms of the current pulse shape and the UHF signals that it excites. This technique will be used exclusively for the coaxial chamber experiments described in Chapter 5.

Time-domain simulation using (4.24) and (4.25) is a lengthy process because a full set of time-domain data for every mode must be generated. For each mode, six separate records are required to allow for the signal paths between source and

coupler shown in Figure 4.15. Contributions from TM modes are particularly time consuming to generate because of the integral term in (4.15) that must be evaluated numerically, requiring several hours for a 40ns record. However, this work has shown that the Green's function technique can be applied to PD in a waveguide of size comparable to that of 400kV GIS. In Chapter 5, a more rigorous analysis for the coaxial configuration is presented. With improved modelling and the use of FFT processing, a considerable improvement in simulation accuracy is achieved. By working in the frequency-domain, the computation time required is considerably reduced and the resulting model is more readily adapted to different configurations.

5. COAXIAL CONFIGURATION

5.1 Introduction

In this chapter, a rigorous study of the coaxial configuration that is of greatest importance for GIS is undertaken. The relevant theory was developed in Chapter 2, and the principles of the approach were introduced in Chapter 4, where the response to a Gaussian pulse was determined by summation of mode responses in the time-domain. In addition to applying the theory for a coaxial configuration, many of the simplifications made in Chapter 4 have been eliminated. Consequently, closer agreement between the simulated and measured UHF signals has been achieved. This is largely due to the use of FFT processing, which allows the summation of a greater number of propagating modes, better modelling of the measurement system, and use of the actual PD pulse shape in the simulation, rather than a Gaussian approximation to it. Accuracy of the resulting model is tested by comparing simulated and measured results for a variety of test configurations. Results confirm that the relationship between the PD current pulse and the UHF signal has been successfully established. The model is a useful tool because it allows the UHF electric field strength at the coupler location to be predicted for a wide range of defect sizes, locations and PD pulse shapes. The effects of varying these parameters are investigated and the significance for UHF PD measurements is discussed.

5.2 Experimental Procedures

5.2.1 Description of the coaxial chamber and test equipment

The simplest configuration for comparing measured and simulated UHF signals would be a very long, uniform section of GIS, or one with broadband, matched terminations. In either case, reflections could be eliminated within the measurement

period. These requirements are impractical, therefore we have again resorted to using a shorter chamber with totally reflecting endplates, as shown in Figure 5.1. Each reflection causes a reversal in the direction of the radial field and, provided the simulation time is limited, all reflection paths taken by the signal between source and coupler can be incorporated. The purpose of the experiment is to excite and record UHF signals, in a controlled manner, inside a coaxial chamber of dimensions comparable to those of a 400kV GIS. The UHF coupler used must have a known response to a varying electric field, so that its output voltage is a valid measurement of the electric field at the coupler location. The excitation source must also be fully defined in terms of its location in the chamber and the current pulse that it carries. For these reasons, monopole probes were used both to inject a simulated PD pulse and to couple the UHF signal out of the chamber. The probes were reduced in length from the 30mm used in the hollow cylindrical chamber work of Chapter 4. This improves the accuracy of the impedance model by diminishing the effects of chamber wall curvature and helps to localise the electric field measurement of the coupling probe. However, as the length of the probes is reduced, the UHF signal levels decrease quite rapidly. A length of 25mm was found to give a reasonable compromise between these conflicting requirements. The probe used to excite the chamber can be mounted at the outer or inner conductor (see Figure 5.2). Mounting at the inner conductor was achieved by feeding the 50Ω semi-rigid cable inside the hollow tube that forms the inner conductor. The coupler probe was always mounted on the outer conductor during the experiments, as this would be the normal location of a UHF coupler.

The chamber length is 3.6m and the inner and outer conductor radii are 0.05m and 0.25m respectively. A set of holes in the chamber wall allows the position of the source and coupler probes to be altered. Signals from the coupler are amplified and then recorded using the transient digitiser. Digitised records of the UHF signal are transferred to a PC for storage and subsequent processing.

End plate

P1

3.6m

0.5m I.D.

P2

0.1m O.D.

COAXIAL CHAMBER

Trigger source (1kHz)

CMOS

PULSE CIRCUIT

A

B

PREAMPLIFIER   **DIGITISER**   **PC**
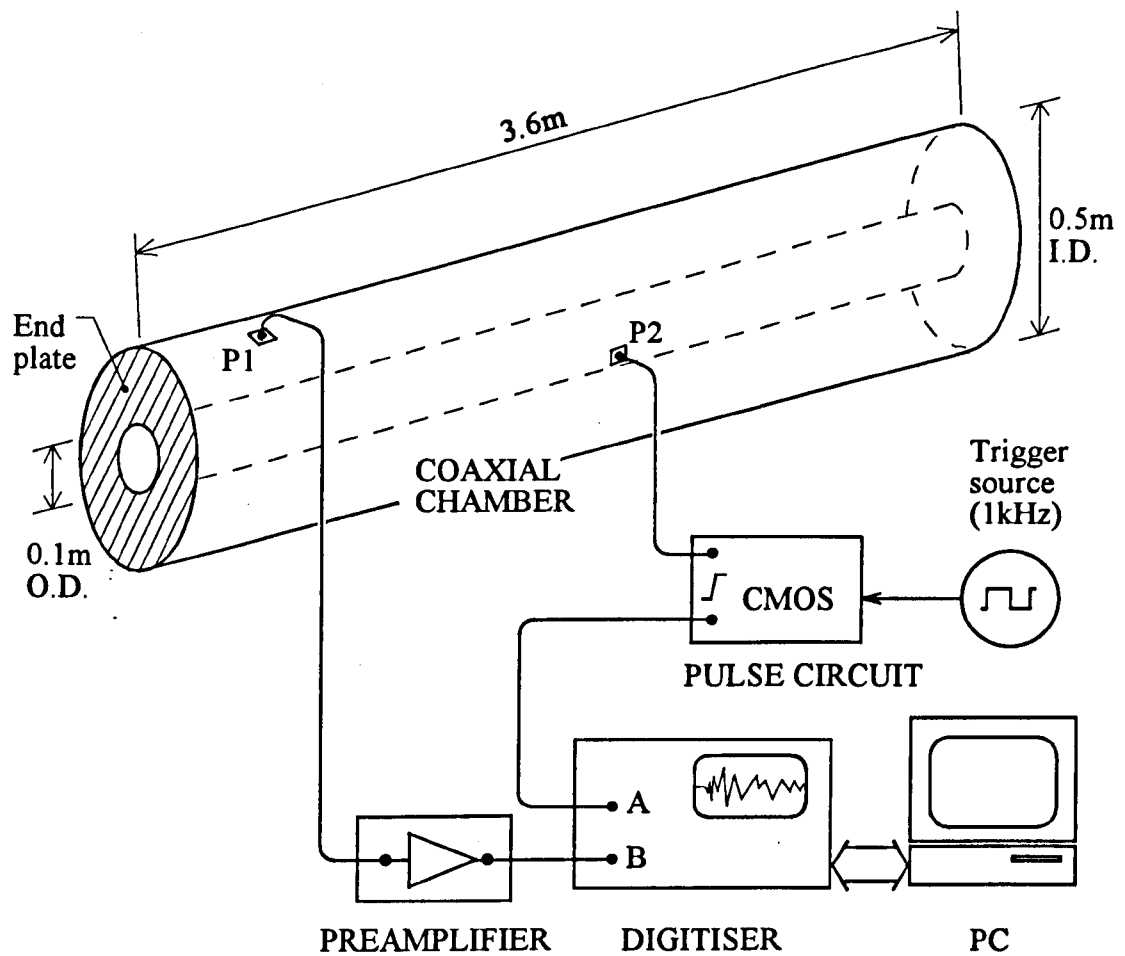
P1=Probe coupler

P2=Source probe

Figure 5.1 Coaxial test chamber and measurement equipment.

1.3mm

(a)

25mm

SMA TYPE
CONNECTOR

(b)

(c)
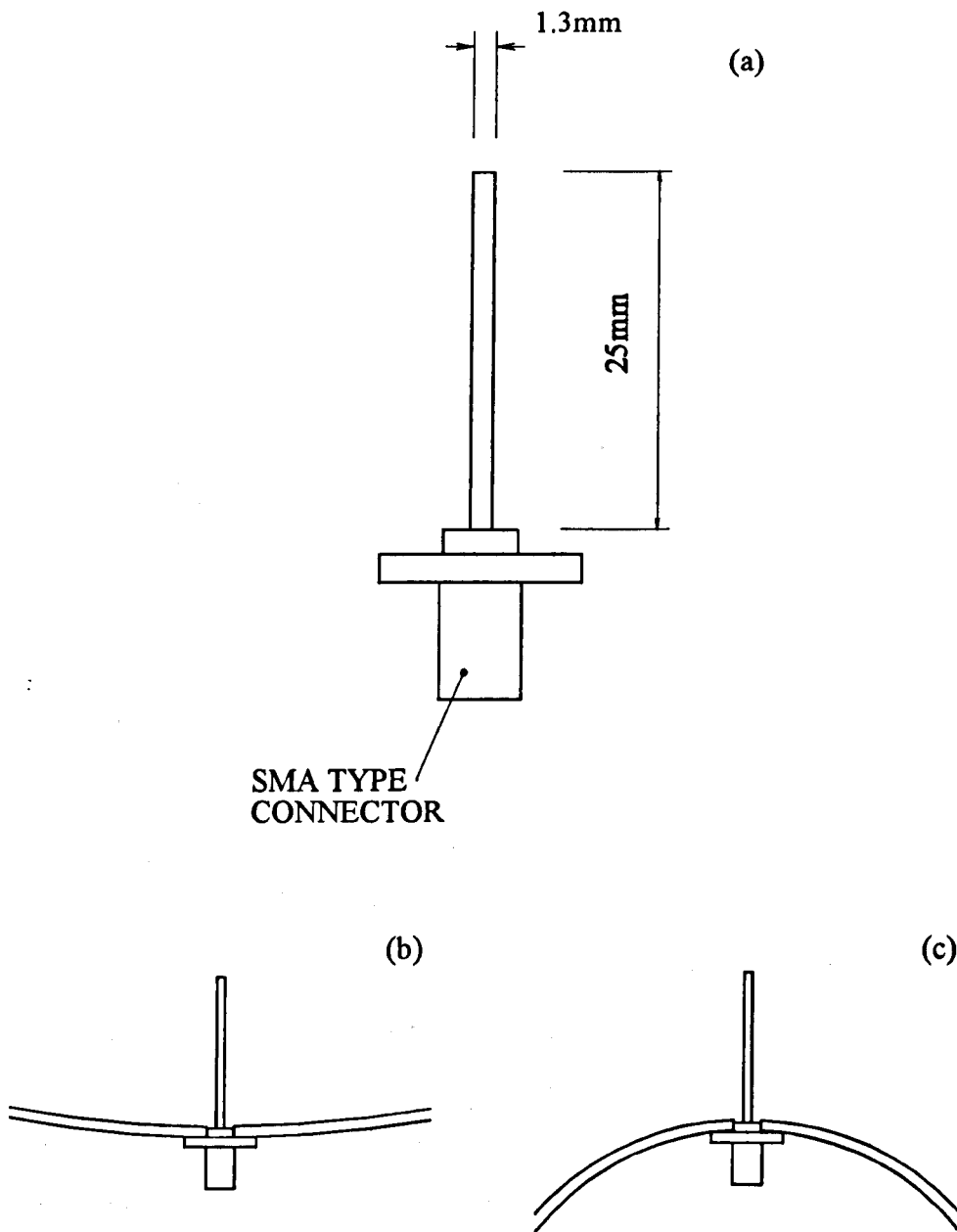
Figure 5.2 (a) Dimensions of the monopole probe, (b) mounting detail at the
outer conductor of the coaxial test chamber, and (c) mounting
detail at the inner conductor.

The CMOS circuit used to drive the current injection probe is shown in Figure 5.3. While the circuit is unchanged from that described in Chapter 4, different parameters have been specified for the more rigorous analysis that follows. In Chapter 4, the input probe was modelled as a lumped capacitance so that the current flowing into it could be obtained by differentiating the applied voltage waveform. However, a more accurate result can be obtained by using the complex input impedance of the probe, $Z_p(\omega)$.

The probe impedance Z_p and its effective height h_e are both frequency dependent and can be determined from published tables [55]. The effective height will be required later for modelling the probe as a coupler and it is convenient to introduce this data here. The tables in [55] list the effective half-length and input impedance for dipole antennas of length $2h$ and radius r_p. To obtain the corresponding monopole results, the half-length figures can be used directly for h_e, while the impedance values must be halved to obtain Z_p. The tables contained in [55] are a function of the parameter $\Omega = 2\,ln(2h/r_p)$. The probe dimensions h=25mm and r_p=0.65mm give Ω=8.686. This figure lies between two of the tables, so the required values were obtained by linear interpolation of the data in adjacent tables as a function of Ω. The resulting information pertaining to the 25mm monopole probe is given in Table 5.1. At frequencies below those for which data is available, the monopole was modelled as a simple capacitive probe, with the effective height fixed at h_e=11.6mm and the capacitance at C_e=0.596pF, to interpolate smoothly with the first set of data in Table 5.1.
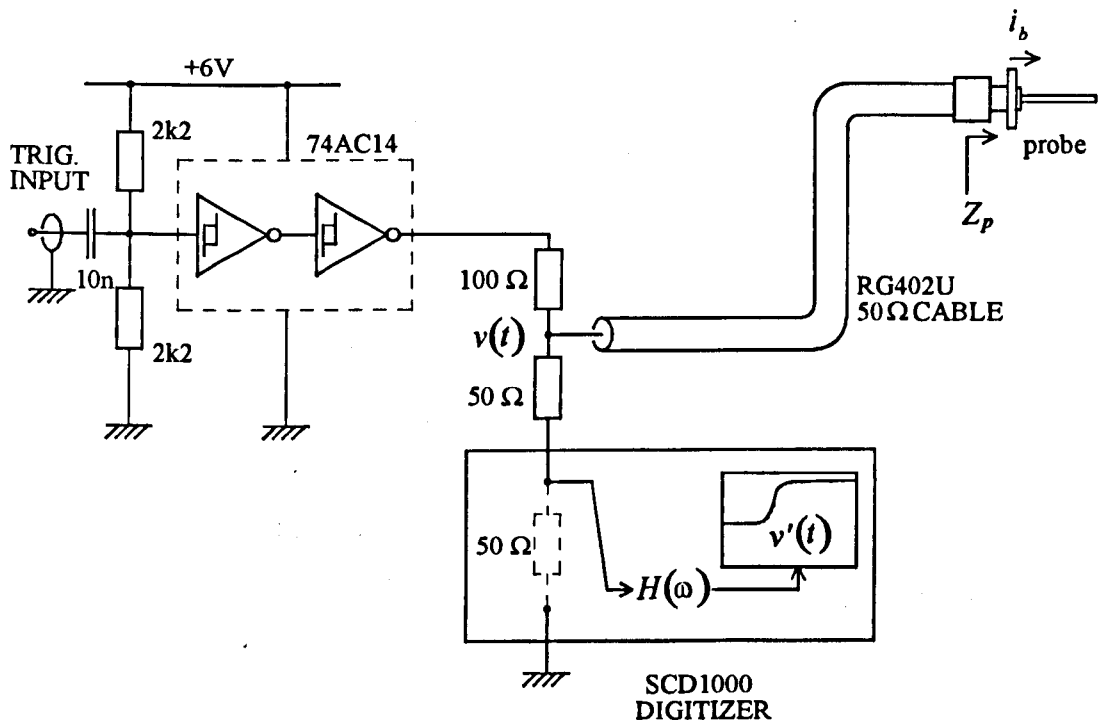
Figure 5.3 CMOS driver and monitoring circuit for generating controlled current pulses on the input probe.

Table 5.1

Data used to model the impedance and effective height of the 25mm probe.

frequency (MHz)	$\Re\{h_e\}$ (mm)	$\Im\{h_e\}$ (mm)	$\Re\{Z_p\}$ (Ω)	$\Im\{Z_p\}$ (Ω)
954.3	11.6	0.0	2.494	-280.00
1336.0	12.0	-0.1	5.155	-178.70
1717.7	12.6	-0.1	9.210	-115.45
2099.4	13.3	-0.2	15.215	-68.55
2290.2	13.7	-0.1	19.215	-48.11
2481.1	14.4	0.3	24.230	-28.91
2672.0	16.0	0.5	30.380	-10.47
2862.8	17.8	-0.5	38.025	7.51

The output stage of the CMOS driver forms a potential divider, so that the voltage recorded at the digitiser input is approximately half the actual voltage $v(t)$ fed to the probe. The finite bandwidth of the digitiser causes significant lengthening of the sub-nanosecond voltage transitions. For this reason, a correction was made for the frequency response $H(\omega)$ of the digitiser in the processing used to recover the current pulse shape. With reference to Figure 5.3, the frequency-domain current pulse flowing into the base of the probe is given by

$$I_b(\omega) = \frac{V(\omega)}{Z_L + Z_p(\omega)} = \frac{2.016}{[Z_L + Z_p(\omega)]} \frac{V'(\omega)}{H(\omega)} \tag{5.1}$$

where Z_L is 50Ω, $V(\omega)$ is the Fourier transform of the probe driving voltage $v(t)$, $V'(\omega)$ is the Fourier transform of the recorded voltage $v'(t)$ and 2.016 is the potential divider ratio of the pulse circuit introduced in Chapter 4. Equation (5.1) was implemented in sampled form using Mathcad to perform the FFT processing

with a 100ns record length and 2048 points. Based on the measured magnitude response of the digitiser, $H(\omega)$ was modelled as a first order lowpass filter with a cut-off frequency of 1.1GHz,

$$H(\omega) = \frac{1}{1 + j(\omega/\omega_c)} \qquad (5.2)$$

The rising voltage edge applied to the probe was extracted from the digitiser record and a cosine smoothing function was used to expand the record length as shown in Figure 5.4, thereby increasing the frequency resolution of the FFT. Figure 5.5(a) shows the critical portion of the voltage waveform $v'(t)$ as recorded on the digitiser and compares this with the waveform corrected for $H(\omega)$,

$$v'(t)_{corr} = \text{FFT}^{-1}\left\{\frac{V'(\omega)}{H(\omega)}\right\} \qquad (5.3)$$

Figure 5.5(b) shows the current pulse $i_b(t)$ recovered using the inverse FFT of (5.1) and compares it with the current pulse determined using a simple capacitive probe model. For the capacitive probe model, the uncorrected rising waveform was differentiated using (4.5) with C_e=0.596pF. The FFT recovered pulse is shorter and larger in amplitude. This pulse was used as the input to the simulations carried out in this chapter. The peak amplitude is 1.57mA and the half-amplitude width is 450ps. Figure 5.5(c) shows the charge flowing into the base of the probe, determined by integrating the current pulse.

The use of the probe technique for simulating PD current pulses, and its equivalence to PD on a protrusion, was demonstrated in Chapter 4. Both the current amplitude and pulse width are comparable with measured PD pulses on a needle in SF_6. The principle advantage relating to the coaxial experiments is that the problem of energising a PD source inside the chamber, without serious intrusion into the volume regarded as free space in the theory, is overcome. The inner conductor could not be

114
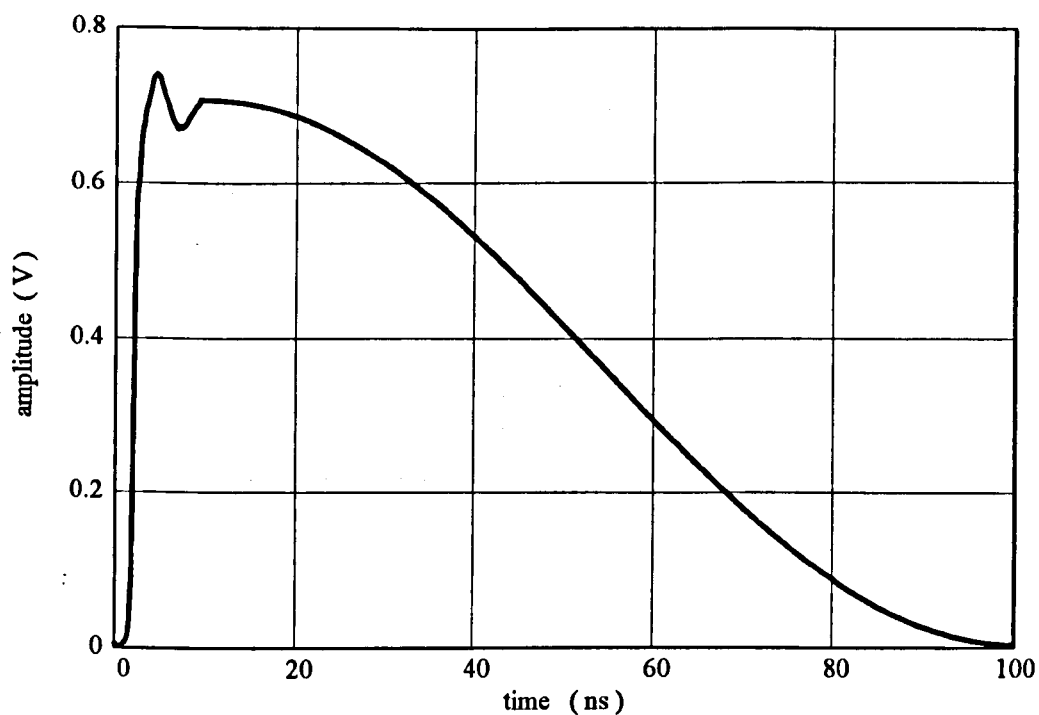
Figure 5.4   The waveform used in the FFT processing to determine the probe
current. The initial rising edge was extracted from the digitiser record
and a cosine smoothing function was used to extend the total record
length to 100ns. The total number of samples for this record is 2048.

(a)

amplitude (V)

- - - uncorrected reflected waveform
— corrected for digitiser response

(b)

amplitude (mA)

- - - simple capacitive probe model
— obtained using FFT

(c)

charge (pC)
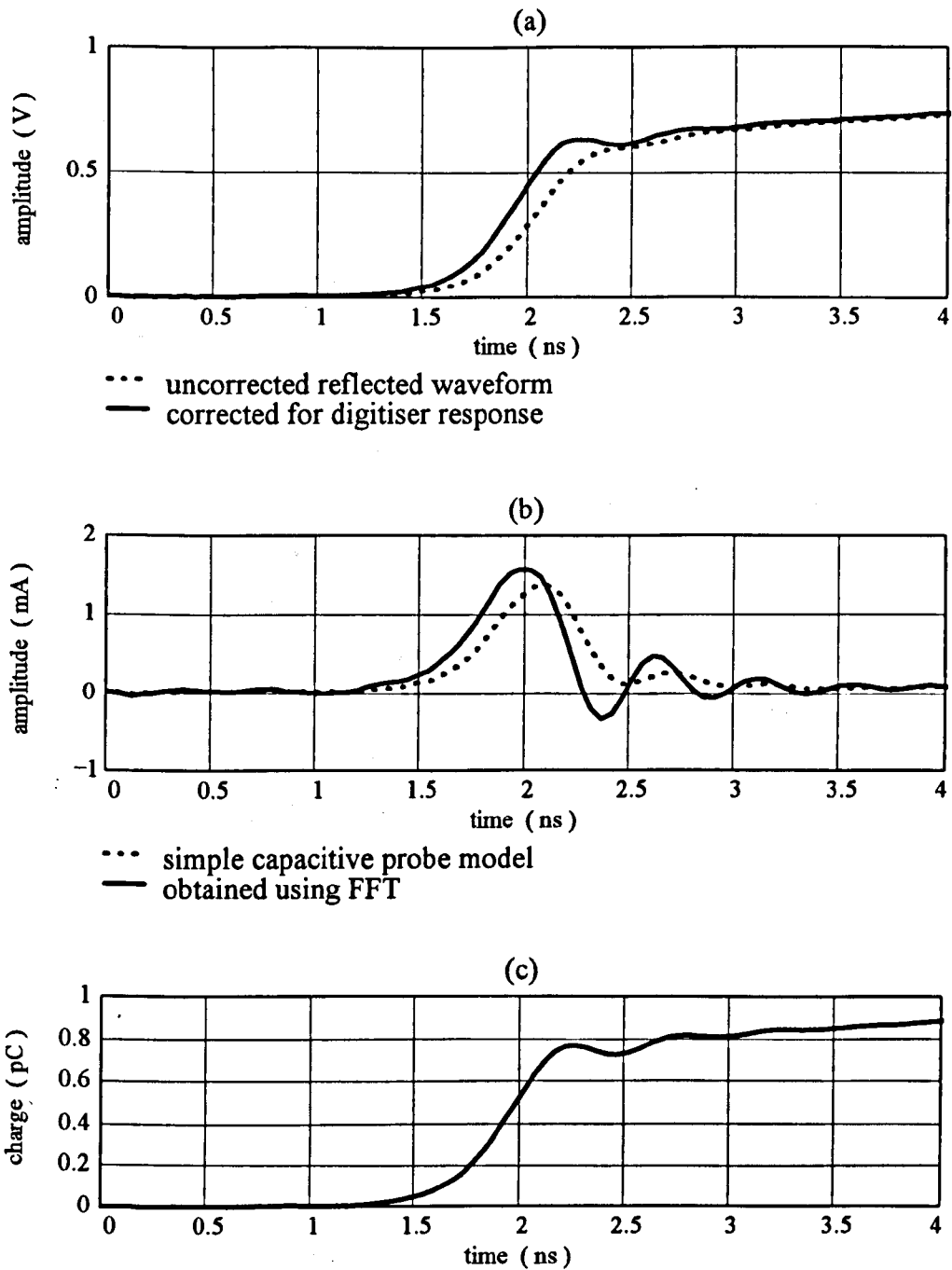
Figure 5.5 (a) Measured and corrected probe driving voltage. (b) Calculated current pulse flowing into the base of the probe. The pulse based on the simple capacitive probe model was obtained from the reflected waveform by differentiating the voltage without compensating for the digitizer response. The pulse shape recovered using the FFT and equation (5.1) is a better approximation to the actual current pulse. (c) The charge flowing into the base of the probe, calculated by integrating the corrected current pulse.

116

used to supply HV to the needle even if the chamber was capable of being pressurised, because of the requirement for short-circuit end plates to permit accurate simulation of the reflected UHF signals.

5.2.3 Recording the UHF signal

The amplified UHF signal was recorded using the digitiser in the experimental arrangement shown in Figure 5.1. The position of the coupler can be altered relative to the source by varying the distance and the relative angle between the two probes. The digitiser timebase was triggered on the rising edge of the source probe driving voltage, so that repetitive operation was possible, with signal averaging to reduce the effects of noise. Each record was averaged over 30 acquisitions. The record length used was 20ns, and this was stored as a 512 point record at an effective sampling rate of 25.6GHz. Longer records were built up in 20ns slices by successively delaying triggering of the digitiser timebase in 20ns steps.

5.3 Theory

5.3.1 Waveguide transfer functions

The frequency-domain transfer functions derived in Chapter 2 for the coaxial configuration are given by equations (2.68), (2.71) and (2.76). These are repeated here for ease of reference:

$$Er_{TEM} = \frac{Z_0}{4\pi b \, ln(b/a)} \, ln\!\left(\frac{r_2}{r_1}\right) I(\omega) e^{-j\omega z/c} \qquad (5.4)$$

$$Er_{TEnm} = K_{TEnm} \int_{r_1}^{r_2} \frac{Z_n(ur')}{r'} dr' \, cos(n\phi) I(\omega) F_{TEnm}(\omega) \qquad (5.5)$$

$$Er_{TMnm} = K_{TMnm} \int_{r_1}^{r_2} X'_n(vr')dr' cos(n\phi)I(\omega)F_{TMnm}(\omega) \qquad (5.6)$$

The TE and TM modes are closely related to those of the hollow cylindrical waveguide, with the $F(\omega)$ functions having an identical form. The TEM mode is non-dispersive; the pulse propagates without distortion and appears at the coupler after a time delay equal to z/c. For a given configuration of source and coupler, the contribution of a mode to the radial electric field in the time-domain can be found by taking the inverse FFT of the product $I(\omega)F(\omega)$.

5.3.2 Sensitivity functions

These functions can be defined by following the procedure used in Chapter 4 for the hollow cylindrical waveguide. The TEM mode is of particular interest, because it is usually the only mode that needs to be considered in VHF detection of PD. The VHF technique was discussed in Section 1.2.5.3, and is sometimes used as an alternative to conventional and UHF PD detection schemes.

As described in Section 4.3.2, we define a short PD path length Δr=0.01m and plot the variation of those terms in the transfer function which are independent of ω. For the TEM mode, let r_1=r-Δr/2 and r_2=r+Δr/2 in (2.68) to give the following sensitivity function

$$S_{TEM}(r) = \frac{Z_0}{4\pi b\, ln(b/a)} ln\left(\frac{r + \Delta r/2}{r - \Delta r/2}\right) \qquad (5.7)$$

Variation of S_{TEM} with radial position r in the coaxial chamber is shown in Figure 5.6. From this graph it is evident that the maximum TEM mode signal at the coupler will occur when the PD source is located at the inner conductor. Since ϕ does not appear in (5.7), the relative angle of coupler and source has no effect. For modes
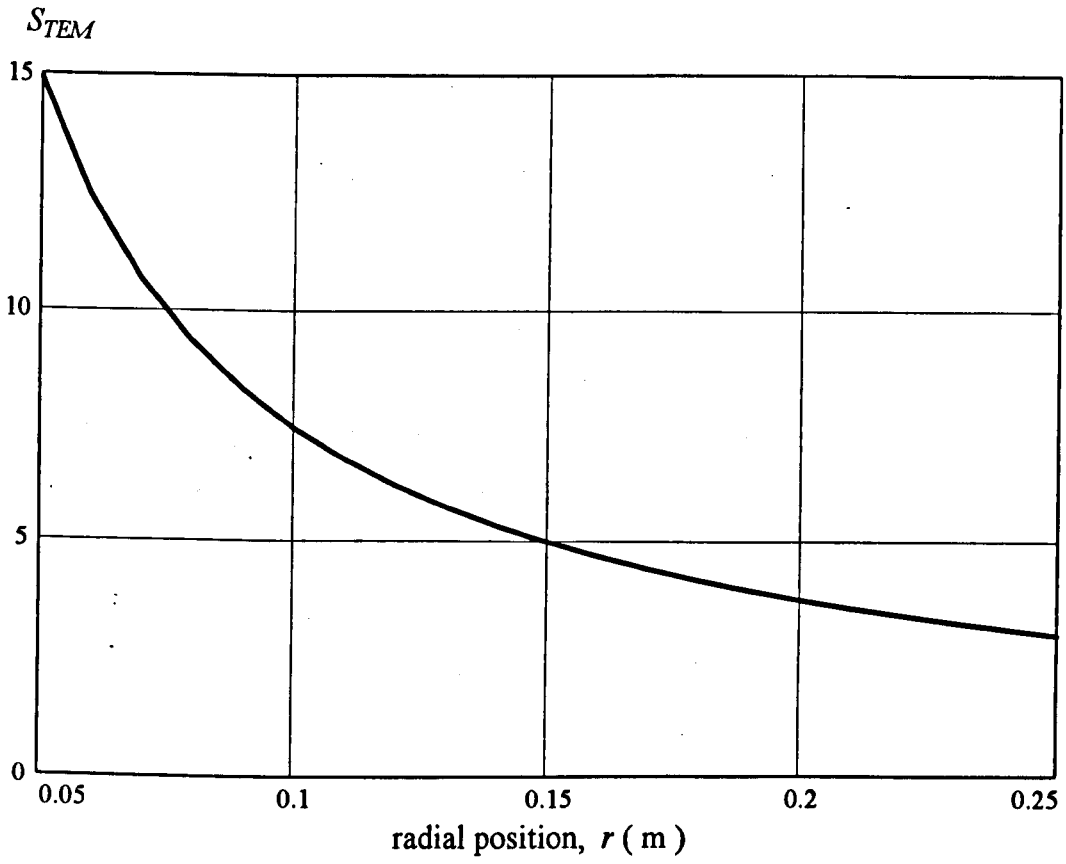
Figure 5.6   Relative sensitivity of the TEM mode to PD excitation as a function of the
radial position of the PD source.

other than the TEM and TM_{0m} modes, angular variation in sensitivity takes the form of modulation by $cos(n\phi)$, with (2.71) and (2.76) giving

$$S_{TEnm}(r,\phi) = K_{TEnm} \int_{r-\Delta r/2}^{r+\Delta r/2} \frac{Z_n(u_{nm}r')}{r'} dr' \, cos(n\phi) \qquad (5.8)$$

$$S_{TMnm}(r,\phi) = K_{TMnm} \int_{r-\Delta r/2}^{r+\Delta r/2} X_n'(v_{nm}r') dr' \, cos(n\phi) \qquad (5.9)$$

The effects of the PD source location defined by (5.8) and (5.9) can be displayed as three-dimensional plots. Two examples are given in Figure 5.7, showing the TEM mode and the TE_{11} mode. The cross-section through the waveguide can be used to select a location for the PD source, and the height of the surface at that point gives the relative amplitude of the radial electric field at the coupler due to the mode in question. Again it should be stressed that the sensitivity functions should only be used to illustrate the relative excitation levels for a single mode, and not for comparison of different mode amplitudes.

5.3.3 Waveguide losses

Dissipative losses have not been included in the theory, to avoid unnecessary complexity. This is reasonable because resonances excited in the test chamber were observed to decay with a time constant of the order of 1μs, much longer than the measurement and simulation periods used in the experiments. However, a brief consideration of the losses caused by the finite conductivity of the waveguide walls is included here because there has been a tendency to assign losses as high as 2dB/m to the skin effect in the GIS.

(a) S_{TEM}
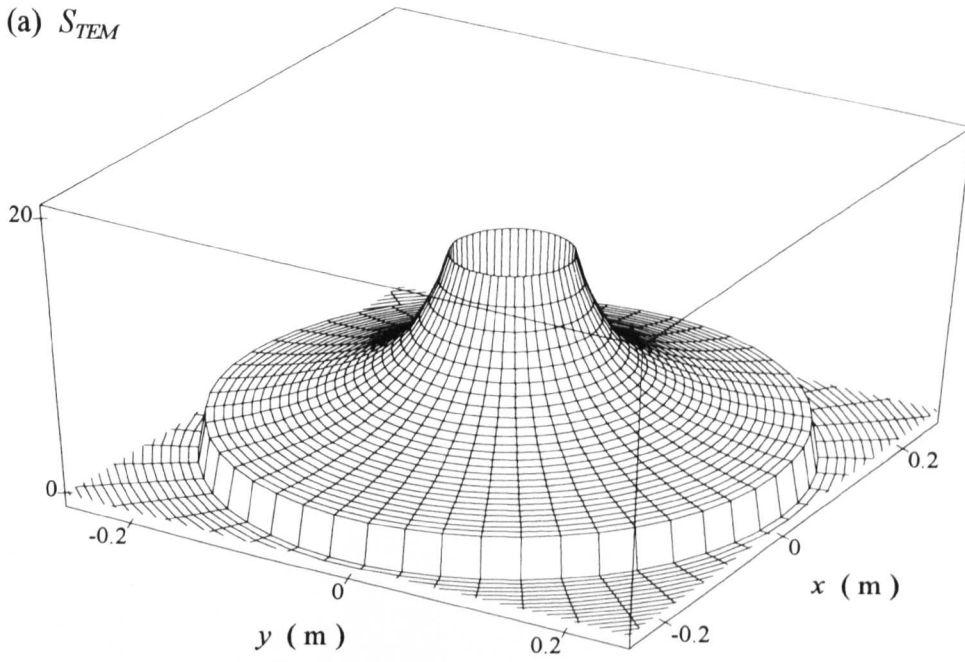
(b) S_{TE11}
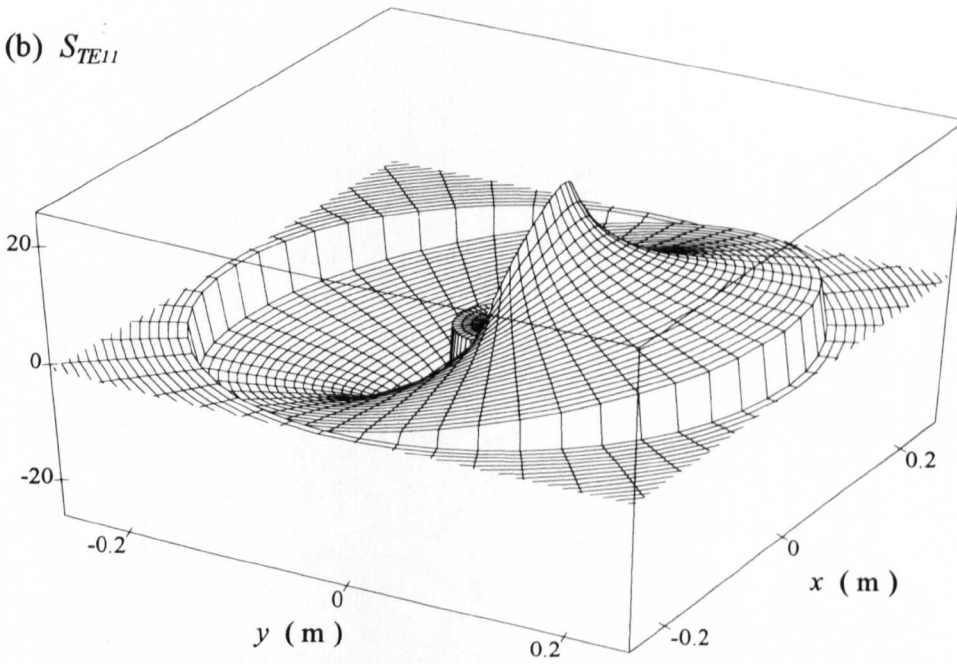
Figure 5.7   Variation of the sensitivity functions over the coaxial cross-section. The polar co-ordinates r and ϕ have been mapped onto a Cartesian x-y plane to produce these plots. The line corresponding to $\phi=0$ is defined as the positive y-axis. (a) TEM mode,   (b) TE_{11} mode.

When the inner and outer conductors are made from the same metal, Marcuvitz [45] gives the following expressions for the attenuation constant α for the three mode types as

$$\alpha_{TEM}(f) = \frac{R(f)}{2Z_0 \, ln(b/a)}\left(\frac{1}{a} + \frac{1}{b}\right) \qquad (5.10)$$

$$\alpha_{TEnm}(f) = \frac{R(f)}{Z_0} \frac{\left[\frac{a^2 J_n'^2(ua)}{b^3 J_n'^2(ub)} + \frac{1}{a}\right]\frac{n^2}{u^2 a^2}\sqrt{1 - \frac{f_{nm}^2}{f^2}} + \left[\frac{J_n'^2(ua)}{bJ_n'^2(ub)} + \frac{1}{a}\right]\left[\frac{f_{nm}^2/f^2}{\sqrt{1 - f_{nm}^2/f^2}}\right]}{\frac{J_n'^2(ua)}{J_n'^2(ub)}\left[1 - \frac{n^2}{u^2 b^2}\right] - \left[1 - \frac{n^2}{u^2 a^2}\right]} \qquad (f > f_{nm}) \qquad (5.11)$$

$$\alpha_{TMnm}(f) = \frac{R(f)}{Z_0} \frac{\left[\frac{J_n^2(va)}{bJ_n^2(vb)} + \frac{1}{a}\right]}{\left[\frac{J_n^2(va)}{J_n^2(vb)} - 1\right]\sqrt{1 - \frac{f_{nm}^2}{f^2}}} \qquad (f > f_{nm}) \qquad (5.12)$$

where f_{nm} is the mode cut-off frequency. The terms in these equations have been converted to a form consistent with the notation used in Section 2.5. $R(f)$ is the frequency dependent characteristic resistance of the conductor surfaces,

$$R(f) = 34.406\sqrt{\frac{f}{\sigma c}} \qquad (5.13)$$

where σ is the conductivity of the conductor surfaces, which in the case of aluminium is typically $\sigma_{al} = 2 \times 10^7$ mhos/m [45]. The attenuation constants defined by (5.10) - (5.12) have units of Nepers/m, so they must be scaled by a factor of 8.686 to obtain dB/m. The calculated losses of some modes are plotted in Figure 5.8
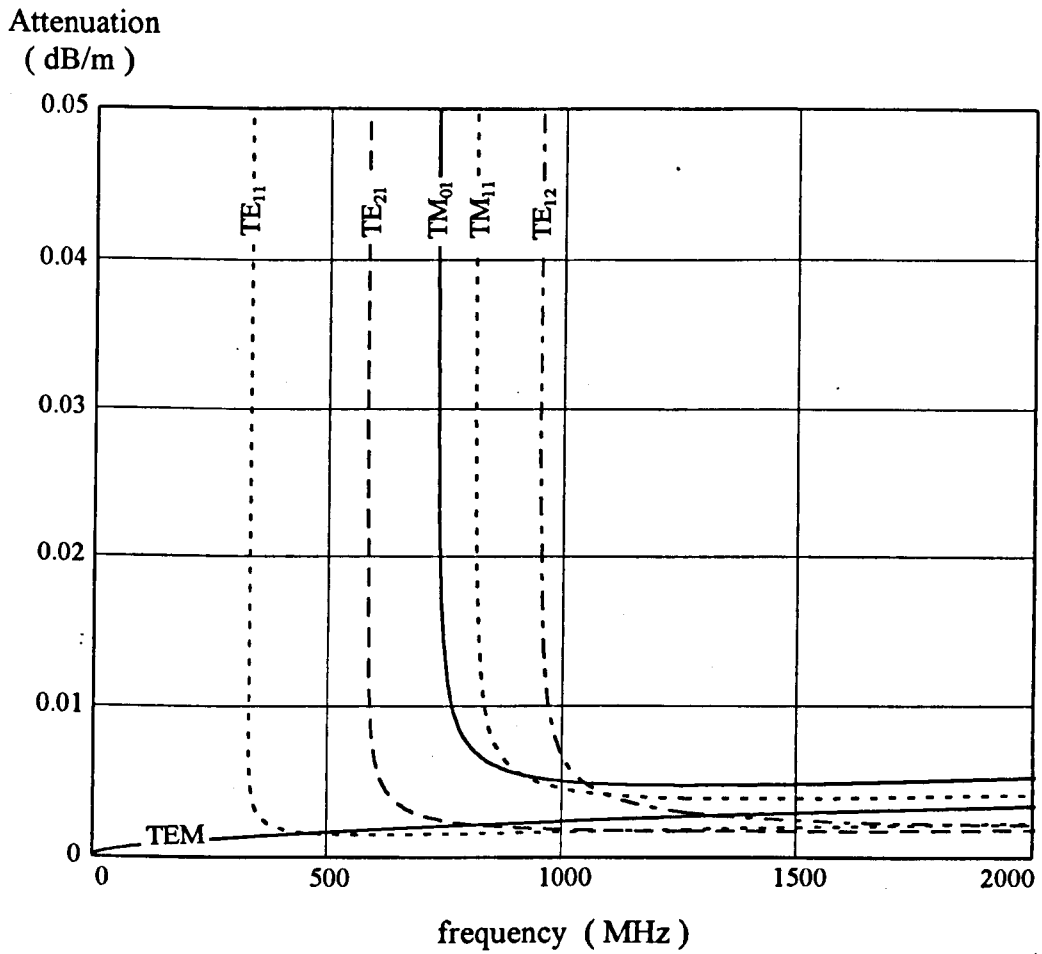
Figure 5.8 Attenuation curves for some propagating modes in an aluminium
coaxial waveguide with inner and outer conductor diameters of
0.10m and 0.50m respectively.

as a function of frequency for a coaxial aluminium waveguide having the same conductor radii as the experimental test chamber shown in Figure 5.1. The predicted attenuation due to surface resistance is typically below 0.005dB/m at frequencies up to 2000MHz. The attenuation peaks close to the cut-off frequencies of the higher order modes occur because at these frequencies the signals undergo a greater number of reflections from the waveguide walls as they propagate over a given distance. This high attenuation just above cut-off only affects a very narrow band of frequencies for each mode.

Attenuation figures of 1-2dB/m have been reported for UHF signals in GIS [2]. This issue requires clarification to distinguish between the effects of losses and those of reflections. Figure 5.8 indicates that skin effect losses cannot account for the observed attenuation, as they are of the order of 10^3 times smaller. Dielectric loss in the epoxy material of which barriers are constructed has been shown to be negligible at frequencies up to 2GHz [63], as have losses in uniform sections of GIS bus duct [64]. Clearly the reported attenuation figures cannot be due to dissipation, and must be caused mainly by the reflections that occur at all discontinuities within the GIS. Each portion of uniform transmission line between two discontinuities forms a leaky cavity that is coupled to adjacent cavities by means of its partially reflecting terminations. This has been illustrated by a first order analysis in which a barrier is modelled as a flat dielectric sheet [65]. Calculation of the higher order mode reflection coefficients for actual barrier shapes and other GIS discontinuities would be difficult. Experimental measurement and finite element modelling may be better tools for determining the effects of real discontinuities.

5.4 Frequency Domain Simulation

5.4.1 Application of the transfer function equations

The various elements of the model were combined and implemented using the Mathcad software package, as follows:

1) The eigenvalues for the TE and TM modes in the experimental coaxial chamber were determined by solving for the roots of equations (2.59) and (2.66) with a=0.05m and b=0.25m. The results are listed in Tables 5.2 and 5.3.

Table 5.2

Eigenvalues u for the TE_{nm} modes.

	m=1	m=2	m=3
n=1	6.820462857	19.84341916	33.73227421
n=2	12.13889805	25.97978485	38.19782403
n=3	16.79624219	31.85512763	44.42412776
n=4	21.26936822	37.09354086	50.44073556
n=5	25.66238603	42.07401978	55.88569106
n=6	30.00505736	46.93900178	61.06088627
n=7	34.31134532	51.72945027	66.11546234
n=8	38.58968655	56.46206419	71.09573739
n=9	42.84573588	61.14694935	76.01832854

Table 5.3

Eigenvalues v for the TM_{nm} modes.

	$m=1$	$m=2$	$m=3$
$n=0$	15.26382532	31.14212681	46.92841421
$n=1$	16.94299218	32.22143300	47.70632716
$n=2$	20.88707308	35.21577432	49.97439355
$n=3$	25.57839667	39.49555796	53.52260421
$n=4$	30.36150216	44.36319845	57.98716995
$n=5$	35.08695553	49.37437657	62.93774791
$n=6$	39.74455654	54.36048212	68.04679699
$n=7$	44.34549309	59.28557474	73.15662010

The cut-off frequencies are determined from the eigenvalues using (2.74) and (2.79). The number of modes used in the simulation was limited to 26 by including only those having a radial component of electric field and a cut-off frequency below 2GHz. The higher order modes included are listed in Tables 5.4 and 5.5.

Table 5.4

Cut-off frequencies of the TE_{nm} modes (MHz).

	$m=1$	$m=2$	$m=3$
$n=1$	325.4	946.8	1609.5
$n=2$	579.2	1239.6	1822.6
$n=3$	801.4	1519.9	-
$n=4$	1014.8	1769.9	-
$n=5$	1224.4	-	-
$n=6$	1431.6	-	-
$n=7$	1637.1	-	-
$n=8$	1841.2	-	-

Table 5.5

Cut-off frequencies of the TM$_{nm}$ modes (MHz).

	$m=1$	$m=2$
$n=0$	728.3	1485.9
$n=1$	808.4	1537.4
$n=2$	996.6	1680.3
$n=3$	1220.4	1884.5
$n=4$	1448.7	-
$n=5$	1674.1	-
$n=6$	1896.3	-

2) The mode constants K_{TEnm} and K_{TMnm} were calculated by substituting the conductor radii and the eigenvalues from Tables 5.2 and 5.3 into (2.72) and (2.77).

3) For a given experimental configuration, the parameters r_1 , r_2 and ϕ are defined, so that the functions of position in the transfer equations (5.4) - (5.6) can be evaluated. Now the integrals over (r_1, r_2) in these equations are valid when the conduction current amplitude is constant over this path. In some cases this is a good approximation, such as for PD at the tip of a protrusion. However, in the case of simulated PD, the current i_b flowing into the base of the probe is not constant along its length. In Chapter 4, the current was scaled for a cosine distribution by defining an equivalent average value of $2i_b/\pi$. For more accurate results, the current distribution given by (4.7) should be included in the path length integrals for the TEM, TE and TM modes. This approach takes account of variations in excitation sensitivity along the PD path. For example, the integral in (5.5) becomes

$$\int_{r_1}^{r_2} \frac{Z_n(ur')}{r'} \cos\left(\frac{\pi}{2}.\frac{r_1-r'}{r_1-r_2}\right) dr' \qquad (5.14)$$

If the probe is mounted at the outer conductor, then $r_1=b-\ell$ and $r_2=b$ in (5.14). These integrals were carried out numerically using Mathcad.

4) All the distances in the z-direction at which the signal passes the coupler position within a 40ns period are determined by sketching the signal paths in the manner shown in Figure 4.15. Only six paths were identified for the configurations used in the 3.6m long chamber. The total field at the coupler is the sum of these six fields, each one having travelled a different distance. The contribution from signals that have undergone an odd number of reflections is reversed in polarity, while those with an even number of reflections are unchanged. The six values for z complete the definition of all the parameters required by the theory.

5) The ω-dependent functions in the transfer equations were converted to complex vectors by frequency-domain sampling.

5.4.2 Modelling the probe coupler

The transfer function of the loaded probe is given by [54] as:

$$T_p(\omega) = \frac{V_L(\omega)}{Er(\omega)} = \frac{-Z_L\, h_e(\omega)}{Z_L + Z_p(\omega)} \qquad (5.15)$$

where V_L is the output voltage, Er is the incident electric field parallel to the probe and Z_L is the load impedance. The effective height h_e and the probe impedance Z_p have been tabulated as complex quantities in Table 5.1. Continuous functions of frequency were constructed from the tabulated values by using the linear interpolation function of Mathcad. At frequencies below those for which data is available, the simple capacitive model C_e=0.596pF gives a good approximation, with

h_e=11.6mm and $Z_p(\omega) = -j/\omega C_e$. The interpolated function can then be sampled in the frequency-domain for FFT processing as described in Section 5.4.4.

5.4.3 Modelling the measurement system

The frequency responses of the preamplifier and digitiser are approximately first order lowpass characteristics within the frequency range of interest. Their combined response $G(\omega)$ was modelled as a second order Butterworth lowpass filter with a cut-off frequency of f_c=1100MHz and a voltage gain of 23,

$$G(\omega) = \frac{23}{1 + j\omega\sqrt{2}/\omega_c - \omega^2/\omega_c^2} \qquad (5.16)$$

where ω_c=$2\pi f_c$.

5.4.4 Simulating the recorded output voltage

The frequency-domain PD current pulse $I(\omega)$ was obtained by taking the FFT of the corrected pulse shape shown in Figure 5.5(b). The total radial electric field at the coupler $E_{tot}(\omega)$ can then be determined by summing the sampled contributions of the individual mode based on equations (5.4) - (5.6). The UHF voltage recorded by the digitiser in each experiment was simulated by combining the sampled transfer functions of the probe and measurement equipment in the frequency-domain. The expression for the recorded voltage is

$$V_r(\omega) = G(\omega) \cdot T_p(\omega) \cdot E_{tot}(\omega) \qquad (5.17)$$

The time-domain signal $v_r(t)$ was recovered for comparison with measured UHF signals by taking the inverse FFT of (5.17). The number of samples used in the FFT processing was 8192 throughout, giving step sizes of 97.66ps in the time-domain and 1.25MHz in the frequency-domain.

5.5 Experimental Results

5.5.1 Comparison of measured and simulated UHF signals

The measured and simulated UHF signals compared in Figure 5.9 are for the 25mm source probe mounted at the outer conductor in the central plane of the coaxial chamber, and the coupler probe mounted 1.2m from this plane, directly in line with the source probe at $\phi=0$. These signals show a greater similarity than those obtained for the cylindrical chamber in Chapter 4. Both traces correspond to the signal levels recorded by the digitiser (including the preamplifier gain), rather than those at the probe output. The corrected excitation current pulse shape shown in Figure 5.5(b) is centred on $t=2.0$ns with respect to the timescales of Figure 5.9. The equivalent PD magnitude is equal to a charge transfer of 0.5pC along the 25mm probe length. The following characteristics of pulse propagation can be deduced from Figure 5.9:

- The direct path between the two probes is 1.2m in length, so the propagation delay at velocity c will be 4ns. With the input pulse centred on $t=2$ns, the corresponding signal should appear at the coupler centred on $t=6$ns. Both measurement and simulation do show a small signal occurring at this time, but a much larger signal occurs a short time later. This can be explained by considering the propagation of the normal electric field around the inner surface of the outer conductor. A single wavefront arrives by the most direct path at $t=6$ns. However, two identical wavefronts that have travelled around the surface of the outer conductor arrive at the coupler having travelled a distance of $\sqrt{1.2^2 + (2\pi b)^2} = 1.98\,\mathrm{m}$, corresponding to an arrival time of $t=8.6$ns. These waves combine to produce the larger signal visible in the regions between the dotted marker lines in Figure 5.9.

- The electric field radiated from the monopole is proportional to the time derivative of the current pulse on the probe. The field radiated by a unipolar pulse will therefore consist of positive and negative peaks corresponding to the rising and falling edges of the current pulse (analogous to Figure 4.5(a)). Coupling
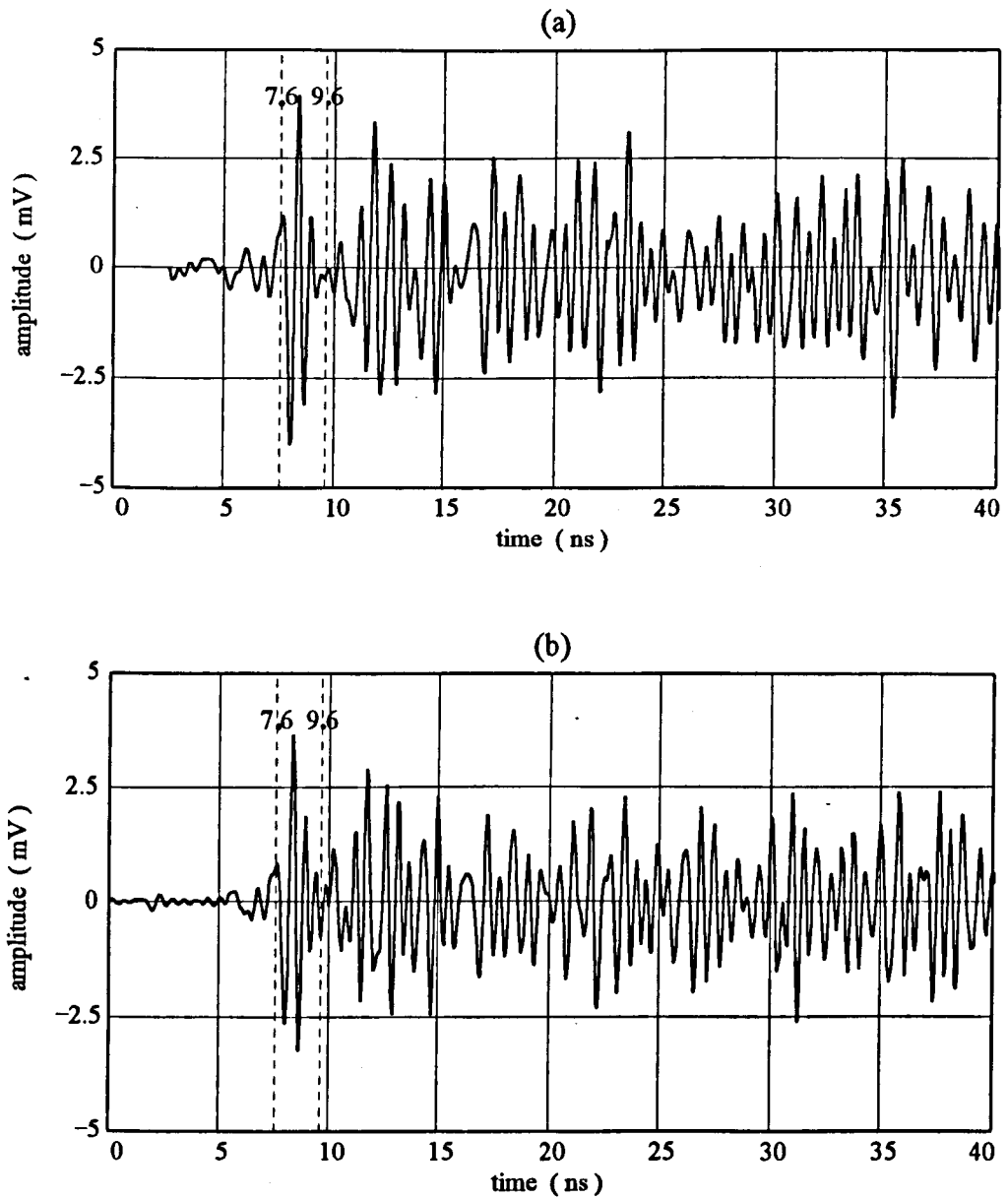
Figure 5.9 Comparison of the first 40ns of measured and simulated UHF signals in the coaxial chamber. The markers indicate the arrival period of the first larger pulse that is due to propagation of the electric field around the circumference of the outer conductor.
(a) Measured signal, (b) simulated signal.

between the electric field and the probe coupler is also dependent on the rate of change, so that a further time differentiation occurs. This effect can be seen quite well in Figure 5.9(b), where four larger peaks of alternating polarity appear between the markers, centred on $t=8.6$ns.

To some extent, the use of normal modes in the analysis can obscure the simple physical processes that give rise to the UHF signal at the coupler. The electric field wavefront spreading out from a PD pulse is proportional to the time derivative of the current, and only has one positive and one negative peak. However, even in a completely uniform section of waveguide, there are an infinite number of paths between the source and coupler because of reflections at the walls. This leads to a UHF signal of much greater duration than the PD pulse. The arrival of the original wavefront by different routes, at different times and with different amplitudes, builds up the 'two-dimensional resonances' referred to by Sellars [66], even at times before any longitudinal reflections in the chamber can occur.

The method of comparing the simulated and measured results by plotting the cumulative energy given by (4.27) will again be employed to assess the accuracy of the results. Figure 5.10 shows the energies calculated for the UHF signals shown in Figure 5.9. These energies are for the signals recorded on the digitiser, and therefore include the preamplifier gain. The cumulative energies at 40ns in Figure 5.10 are 1.07µJ and 0.85µJ for the measured and simulated signals respectively. By using the energy method to compare the signals, the effect of any inaccuracy in the simulation is squared, as discussed in Section 4.5.1. In this case, the energy ratio of $0.85µJ/1.07µJ = 0.79$ corresponds to an amplitude accuracy of $100\sqrt{0.79} = 89\%$.
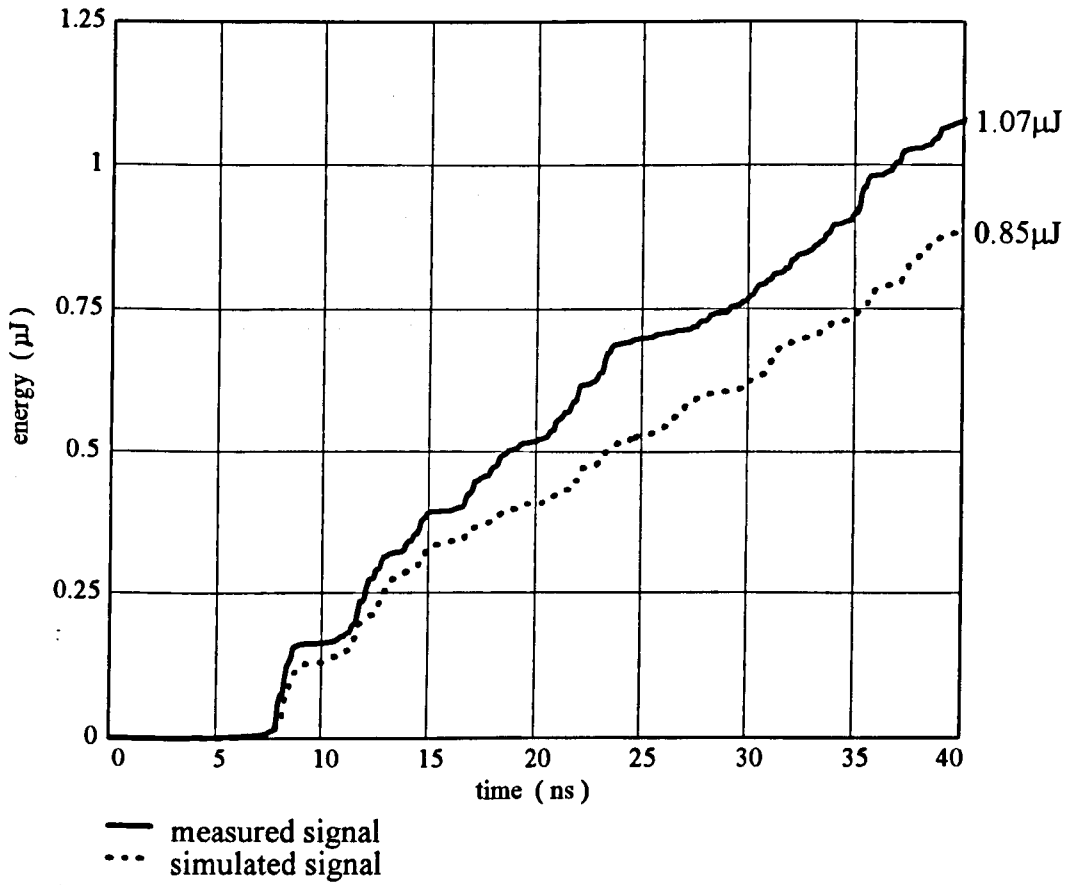
Figure 5.10   Comparison of the cumulative energy for the UHF signals shown in
Figure 5.9, calculated using equation (4.27).

5.5.2 Varying the position of source and coupler

With the source probe mounted at the centre of the chamber, UHF signals were recorded with the coupling probe mounted at distances of 0.9m, 1.2m, and 1.5m from the source in the z-direction, keeping $\phi=0$. The recorded and simulated UHF signals are shown in Figure 5.11, with the timescale expanded to show the first 15ns of the response. The effect of propagation around the circumference of the outer conductor is clearly visible in Figure 5.11(a). In this case the coupler is mounted at 0.9m from the source and an equal distance from the nearest endplate. Considering propagation in the z-direction only, we would expect to see two bursts of UHF signal, centred on $t=2 + 0.9/c = 5$ns and $t=2 + 2.7/c = 11$ns, corresponding to the original wavefront and the first reflection from the endplate. However, the two bursts of UHF at the start of the response are actually due to wavefronts that have both travelled only 0.9m in the z-direction. The first wavefront has also travelled once around the circumference of the outer conductor, while the second one has travelled around it twice. This explains why both bursts have the same polarity and why the increments of 0.3m in probe separation for the three signals in Figure 5.11 cause less than the expected 1ns increase in signal delay. Again this can be explained by circumferential propagation. For example, an increase from $z=0.9$m to $z=1.2$m causes an increase of 0.17m in the length of the propagation path, leading to an additional delay of only 0.57ns. Figure 5.11 illustrates the accuracy of the simulation process, with good agreement between the amplitude and shape of individual cycles of the measured and simulated UHF signals.

Simulations predicted significant variations in the UHF signal level with changes in the relative angle between the source and coupler. To investigate this effect, the coupler probe was mounted at nine angular displacements relative to the source probe, around half the chamber circumference, in the plane 1.2m from the centre of the chamber. The measured signals are compared with simulation in Figure 5.12, which shows the cumulative energies at 40ns. Both sets of results indicate a similar pattern of variation, with significant peaks in signal energy at $\phi=0$ and $\phi=\pi$. This
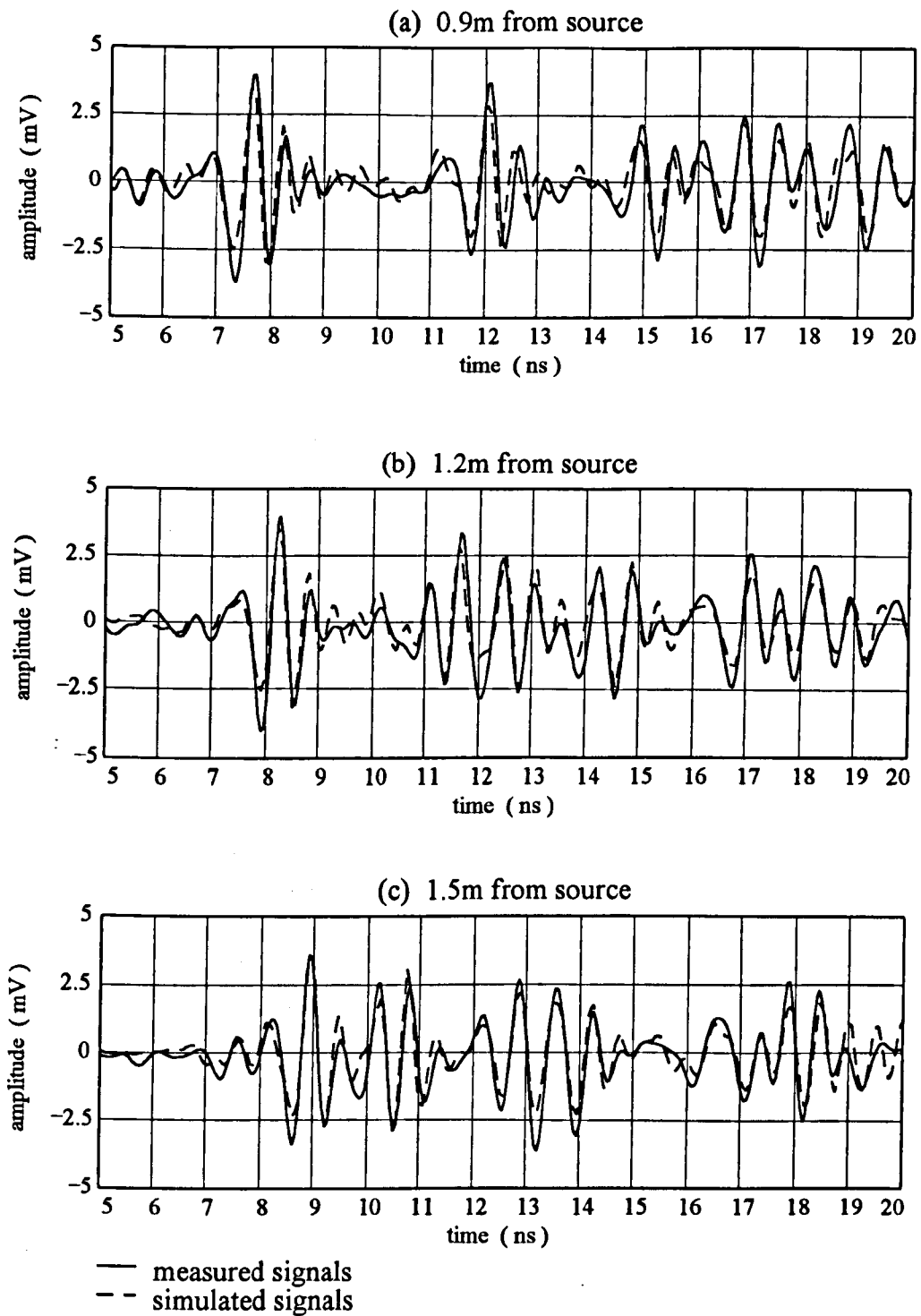
Figure 5.11 Comparison of measured and simulated UHF signals with the coupler located at three distances from the source. The source is in the central plane of the chamber, and the angle between source and coupler is $\phi=0$. (a) 0.9m separation, (b) 1.2m separation, and (c) 1.5m separation.
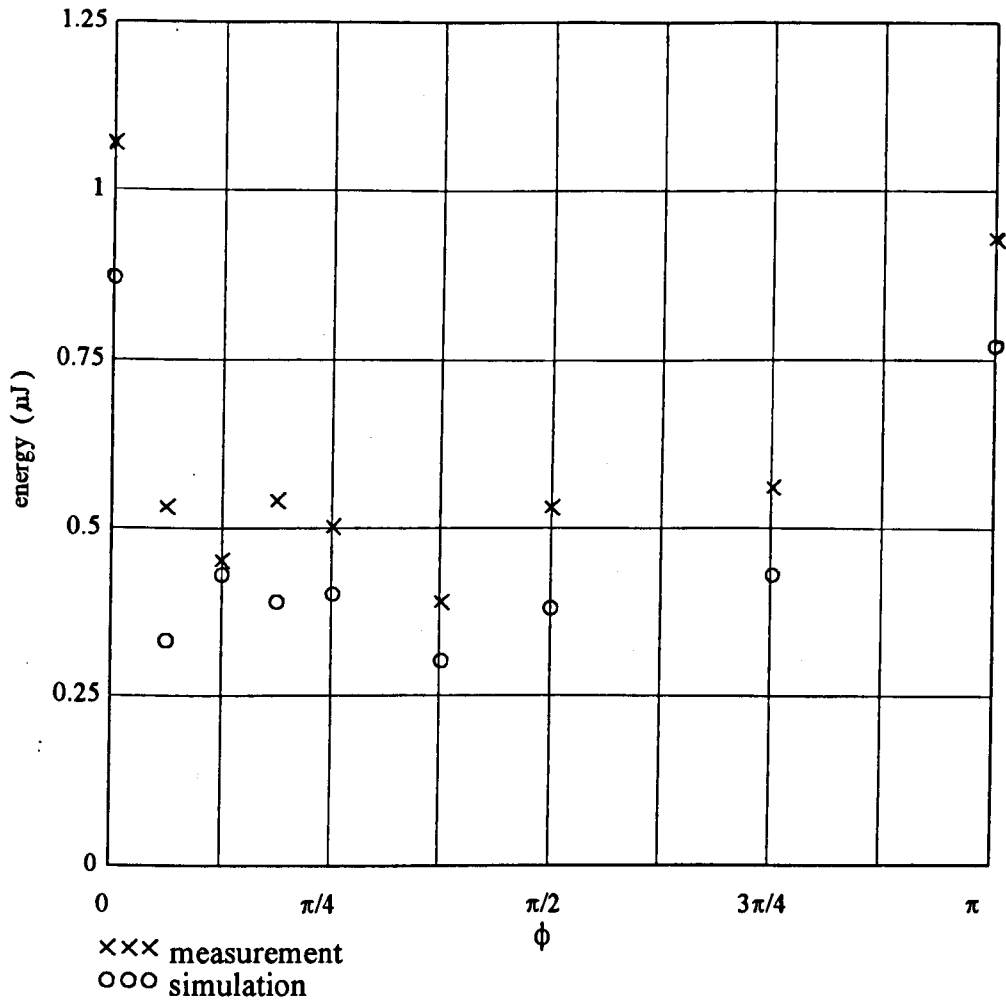
Figure 5.12 Variations in the cumulative UHF energy at 40ns with the relative angle between the source and coupler probes. Separation between source and coupler in the z-direction is 1.2m.

effect is a consequence of the clockwise and anticlockwise circumferential wavefronts discussed above. These wavefronts have travelled equal distances along identical paths and will therefore always interfere constructively at these two angles. The energy predicted by the simulation in Figure 5.12 is consistently less than the measured energy. If these nine results are averaged, the simulated energy is found to be 78% of the measured energy. The average amplitude of the simulated signals is therefore 12% less than the measured signals.

The source probe was then mounted at the inner conductor, at a distance of 0.3m from one end of the chamber. The UHF coupler was mounted in the central plane, at a distance of 1.5m from the source. Examples of the measured and simulated energy with this configuration are shown in Figure 5.13, for relative angles of $\phi=0$, $\pi/2$ and π. Again the energy is greatest when the coupler is 'in line' with the PD source. Simulations with the source probe on the inner conductor gave better agreement with measurement. The average simulated amplitude for these three results was only 1% less than the measured amplitude.

5.5.3 Changing the PD path length and pulse shape

To investigate the accuracy of the theory in predicting the effect of changing the path length of a PD, the 25mm input probe was replaced by a 16mm probe having the same radius. Although the applied voltage waveform remained unaltered, the probe impedance required for determining the current pulse shape was changed. Remodelling of the probe impedance was carried out using the procedure described in Section 5.2.2, with $\Omega=7.793$ resulting in the impedance data shown in Table 5.6. The new locations of the current path endpoints, $r_1=0.250$m and $r_2=0.234$m, were also incorporated in the simulation process. .
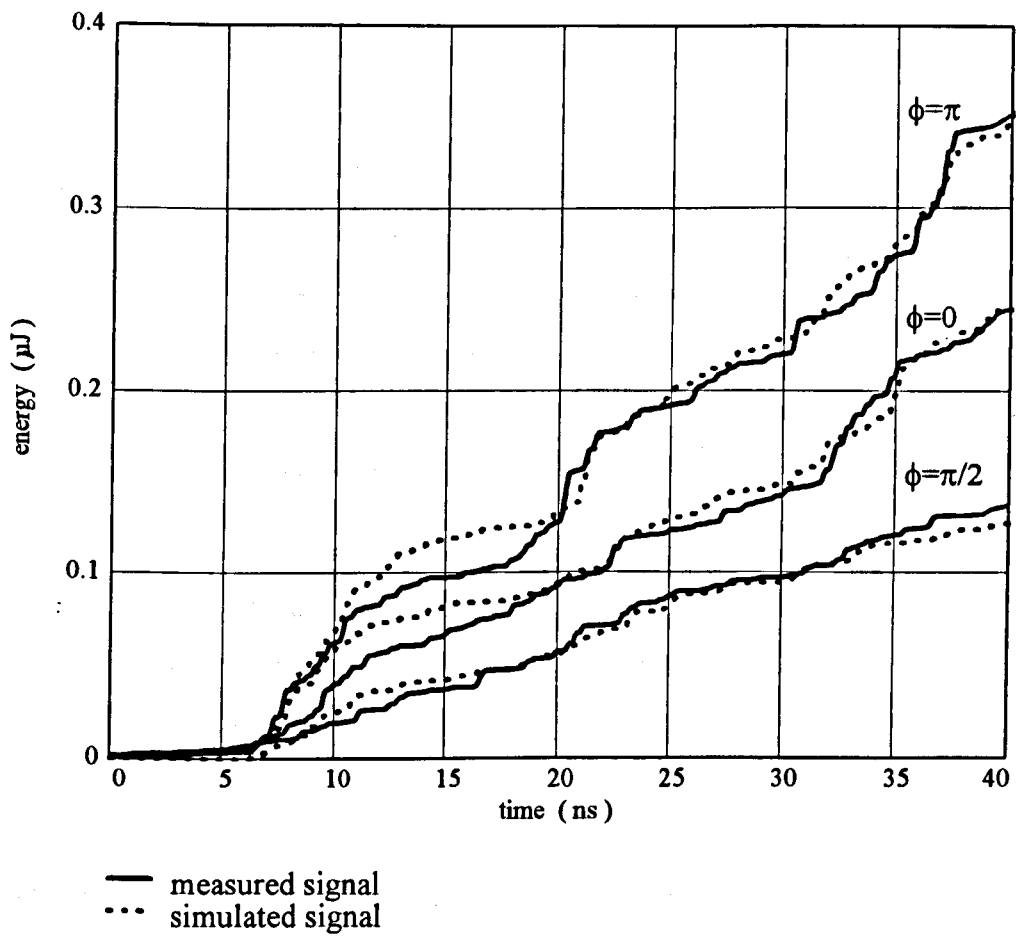
Figure 5.13 Comparison of the measured and simulated UHF energy with the source probe mounted at the inner conductor, 0.3m from one end plate. The coupler is mounted in the plane 1.5m away, and results for three angular displacements are shown.

Table 5.6

Data used to model the impedance of the 16mm probe.

frequency (MHz)	$\Re\{Z_p\}$ (Ω)	$\Im\{Z_p\}$ (Ω)
<1491.0	0	$-1/2\pi f C_e$, C_e=0.462pF
1491.0	2.49	-231.00
2087.5	5.16	-146.85
2683.9	9.26	-94.15
3280.3	15.41	-54.85
3578.5	19.57	-37.65
3876.7	24.73	-21.52
4174.9	31.15	-6.07
4473.1	39.13	8.89

The effect of changing the pulse shape was investigated using the 25mm probe and capacitively loading the CMOS circuit at the input to the microstrip matching resistors. The resulting pulse width could not be greatly extended without decreasing the UHF signal below the level at which a reasonable signal-to-noise ratio could be obtained on the digitiser. However, the maximum rate of change of the current pulse was reduced from 8.6mA/ns to 4.5mA/ns on the falling edge. Experiments using this slower pulse were only carried out with the original 25mm probe, because the 16mm probe did not excite adequate UHF signal levels. Figure 5.14 shows the original current pulse (the corrected pulse from Figure 5.5(b)), for comparison with the corrected current pulses on the 16mm probe and on the 25mm probe with the slower pulse.

The UHF energy excited using the 16mm source probe is compared with that from the 25mm probe in Figure 5.15. The source probe was mounted in the central plane of the chamber and the coupler was mounted 1.2m away, with ϕ=0. In Chapter 4 it was suggested that the UHF signal amplitude is proportional to the product of path
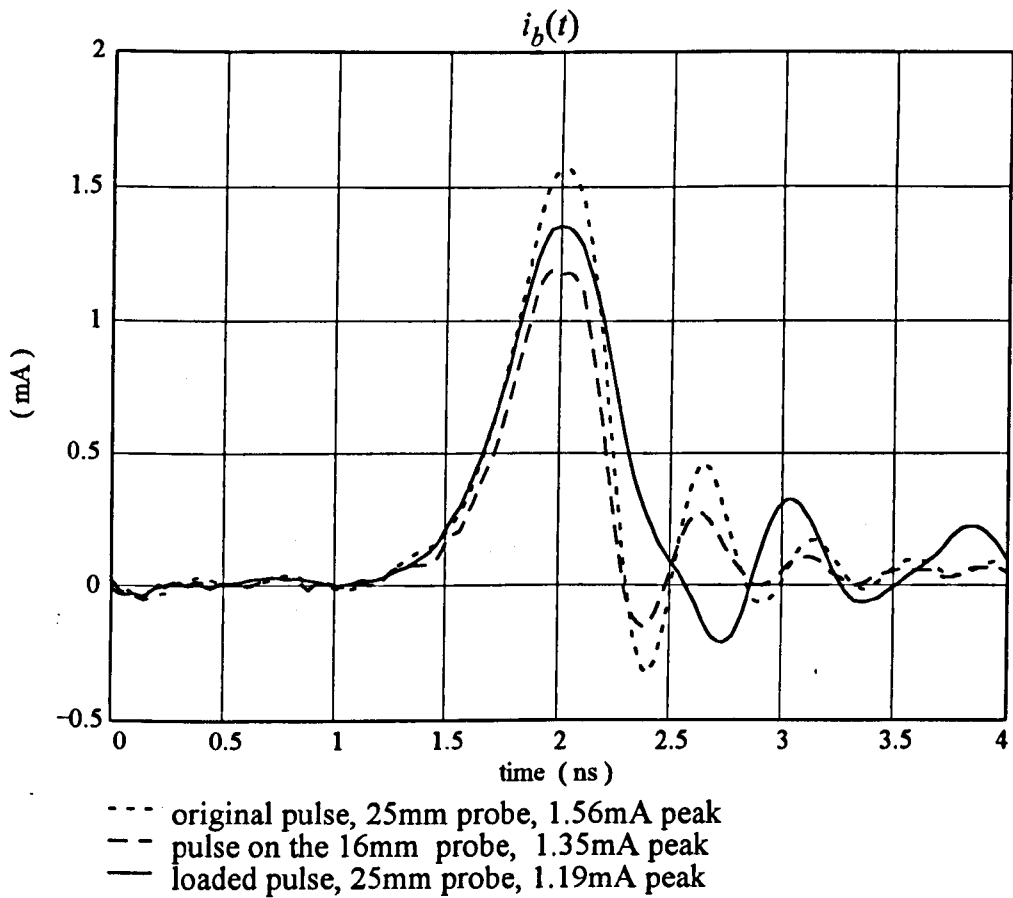
Figure 5.14 Comparison of the original current pulse on the 25mm source probe with the current pulses for the 16mm probe and for the loaded pulse circuit driving the 25mm probe.
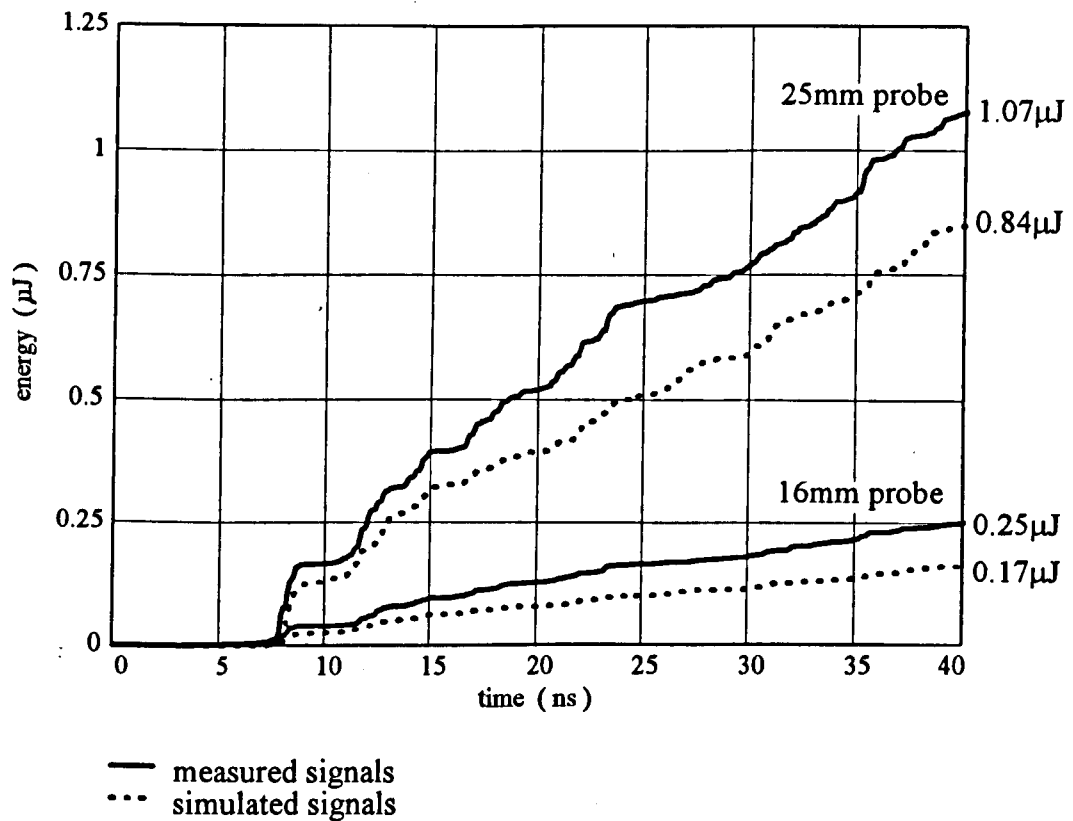
Figure 5.15 Comparison of the UHF energy levels excited by two source probes of different length. Both probes were mounted in the central plane of the chamber, and the coupler was located at a distance of z=1.2m, with ϕ=0.

length and current amplitude for short current paths and a fixed pulse shape. From Figure 5.14, the shape of the pulse on the 16mm probe is seen to be quite similar to that on the 25mm probe, but the peak amplitude has decreased from 1.56mA to 1.19mA. The UHF energy is therefore expected to change by a factor

$$\left(\frac{1.19}{1.56} \cdot \frac{16}{25}\right)^2 = 0.24$$

if any change in the pulse shape is neglected. Taking the energy values at 40ns from Figure 5.15, the ratio of measured energies is 0.23 and the ratio of simulated energies is 0.20. Both of these factors compare well with the expected reduction.

The effect of the slower pulse from Figure 5.14 (on the 25mm input probe) is shown in Figure 5.16. The source probe is mounted in the central plane of the chamber and the coupler is mounted 1.2m away, with $\phi=\pi/8$. On the basis of the reduced current pulse amplitude alone, the signal energy would be expected to change by a factor

$$\left(\frac{1.35}{1.56}\right)^2 = 0.75$$

However, the energy ratios from Figure 5.16 are 0.29 for the measured signals and 0.23 for simulated signals. This demonstrates the importance of the rate of change of current in determining the UHF signal level. The greater percentage difference between simulation and measurement for the smaller signals in Figures 5.15 and 5.16 could be due to the increased significance of noise levels in these records.

5.6 Discussion

5.6.1 Accuracy of results

With the source probe at the outer conductor, the average amplitude accuracy of the simulations (determined on the basis of the square root of the energy ratio relative to measured signals) was 88%. Agreement was better with the source probe at the inner conductor, as can be seen from Figure 5.13. One factor that would explain why
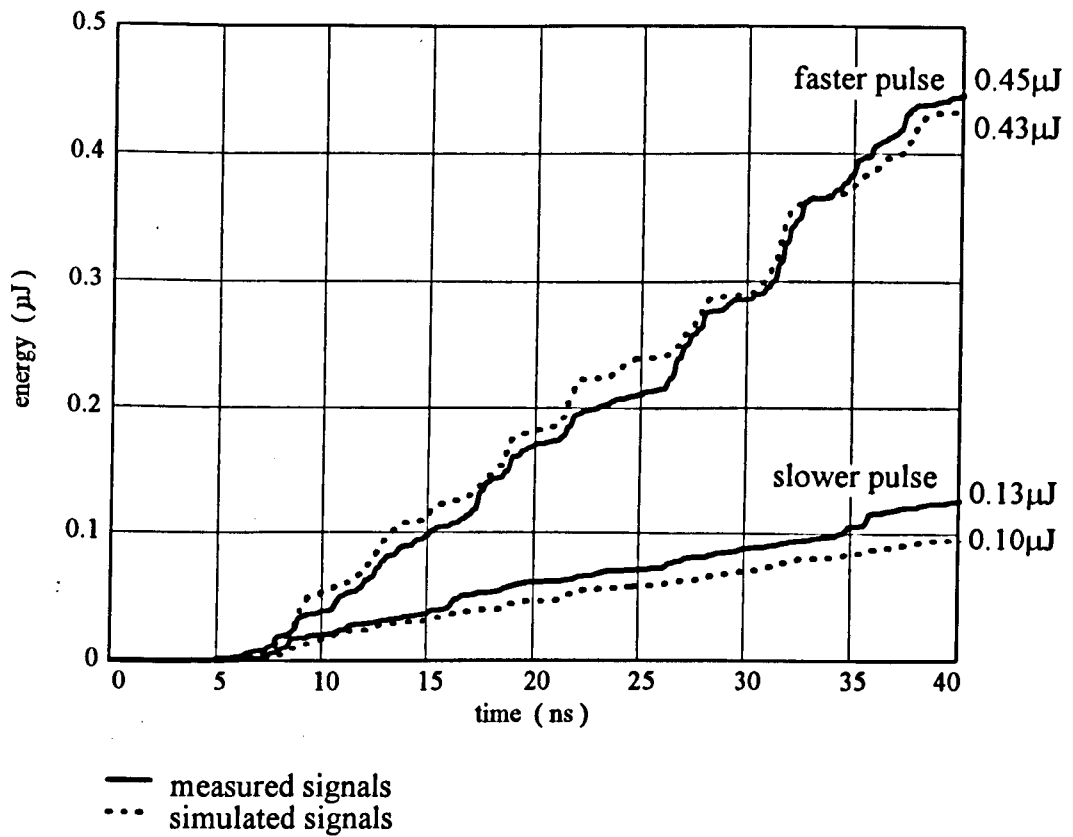
Figure 5.16 Comparison of the UHF energy levels excited by the normal and loaded pulses on the 25mm source probe. The probe was mounted in the central plane of the chamber, and the coupler was located at a distance of $z=1.2$m, with $\phi=\pi/8$.

relatively larger signals are produced by the simulation in relation to measured signals when the input probe is at the inner conductor, is the method used to correct the current pulse shape. This technique uses an approximation for the probe input impedance which is based on that of a monopole protruding through an infinite flat ground plane. When the probe is mounted at the outer conductor the curvature of the wall will increase the capacitive part of the probe impedance. The true current pulse flowing into the probe will therefore have a greater amplitude than that used to generate the simulated signal. If the true current could have been used in the simulation, the amplitude of the resulting UHF signal would have been greater. Conversely, when the probe is mounted at the inner conductor, its capacitance is decreased by the wall curvature. The simulation is then using a slightly larger current than the true probe current. These effects are borne out by comparison of Figures 5.12 and 5.13. In Figure 5.12, the average ratio of simulated to measured energy with the source at the outer conductor is 0.78. In Figure 5.13 this ratio increases to 0.98, confirming that the simulation is producing a larger signal relative to measurement when the source is at the inner conductor.

Another approximation made in the model is that the electric field is constant over the length of the probe coupler, and equal to its value at the surface of the outer conductor. The validity of this approximation depends on the radial variations of the electric field patterns of the propagating modes. Taking the TEM mode as an example, the ratio of the radial field at the tip of the 25mm probe ($r=0.225$m) to that at the outer conductor ($r=0.250$m) is

$$\frac{1/0.225}{1/0.250} = 1.11$$

For the TE_{11} mode, the corresponding ratio is 0.99. Assessing the impact of these variations is difficult, due to the dependence of the total field on the relative contributions of the modes and the uncertain effect of variations in field strength along the probe length. By calculating the radial field variations for some of the modes with lower cut-off frequencies, it appears that a maximum difference of $\pm10\%$

in field strength could occur at the probe tip. An estimate of the possible effect of this variation when averaged over the whole probe length is then ±5%.

5.6.2 Relative contributions of TEM and higher order modes

The TEM mode of propagation in GIS has been studied in some detail, as it is the principal mode of propagation for HV transients and allows GIS components to be modelled using lumped impedance elements [64,67]. This approach can be applied to the consideration of the VHF content of PD signals [21] in the frequency range up to 300MHz, which is usually below the cut-off frequencies of any higher order modes. We have seen that the field radiating from a PD can be represented by a summation of the field patterns of the various modes that it excites. By its nature, a PD source is usually located asymmetrically within the coaxial line. Within the plane containing the source of PD, any excitation of the TEM mode must be associated with considerable contributions from other modes to produce a field that is only non-zero in the region close to the source during the early stages of propagation. As the duration of the PD pulse decreases, the spatial variation of the radiated fields must increase because their propagation velocity is fixed. The number of modes required to adequately represent the field increases as a result. Conversely, if the PD pulse is relatively slowly varying compared with the time taken for the field to traverse the waveguide cross-section, the higher order modes become less significant in the representation of the field pattern and the TEM mode is predominant.

The validity of this argument can be illustrated by comparing the higher order and TEM mode contributions to the electric field for two Gaussian excitation pulses having equal amplitudes but different pulse widths. These contributions cannot be distinguished in an experiment, but a useful feature of the simulation process is that each mode can be examined separately. The configuration used to make the comparison is that of a 10mm PD path located at the outer conductor (r_1=0.240m

and $r_2=0.250m$) in the central plane of the coaxial chamber, with a uniform current distribution over its length. The resulting electric field strength was simulated at a position 1.2m away in the z-direction, with $\phi=0$. The Gaussian current pulse $i(t)$ at the PD source was defined as

$$i(t) = I_{max}\, e^{-(t-t_0)^2/2\sigma^2} \qquad (5.18)$$

For the first example, with $I_{max} = 2.0mA$, $t_0 = 2ns$ and $\sigma = 200ps$, the contributions to the total field are shown in Figure 5.17(a). Integrating the current pulse gives a total charge transfer of 1pC along the path. The higher order modes make a much larger contribution to the total field in response to this pulse, with a peak-to-peak amplitude of 75mV/m compared to 12mV/m peak-to-peak for the TEM mode. The power available from each signal is proportional to the square of the field strength, increasing the significance of this amplitude difference. Furthermore, the higher order modes do not have the 'dead time' that occurs between reflections of the TEM mode pulse, during which it delivers no energy to the coupler.

The second example, shown in Figure 5.17(b), was generated by changing σ to 500ps while leaving t_0 and I_{max} unchanged in (5.18). The pulse width at half-amplitude is thereby increased from 500ps to 1.25ns. The peak amplitude of the TEM mode field remains unchanged and the width of the reflected pulses has increased accordingly. In contrast, the higher order mode field has altered significantly. The amplitude is now comparable to that of the TEM mode, and the high frequency content has decreased.

Er is shown in Figure 5.17 rather than the coupler output voltage, to illustrate the typical electric field strengths to which UHF couplers are subjected. The couplers are normally capacitive, and their sensitivity decreases at lower frequencies [20]. Although the amplitude of the TEM mode field is unchanged in Figure 5.17(b), the resulting coupler output would be significantly reduced because the rate of change of

(a) *Er* for a 500ps pulse width

(a) *Er* for a 500ps pulse width

20mV/m per division

TE & TM

TEM

time (ns)

(b) *Er* for a 1.25ns pulse width

(b) *Er* for a 1.25ns pulse width

20mV/m per division

TE & TM

TEM

time (ns)
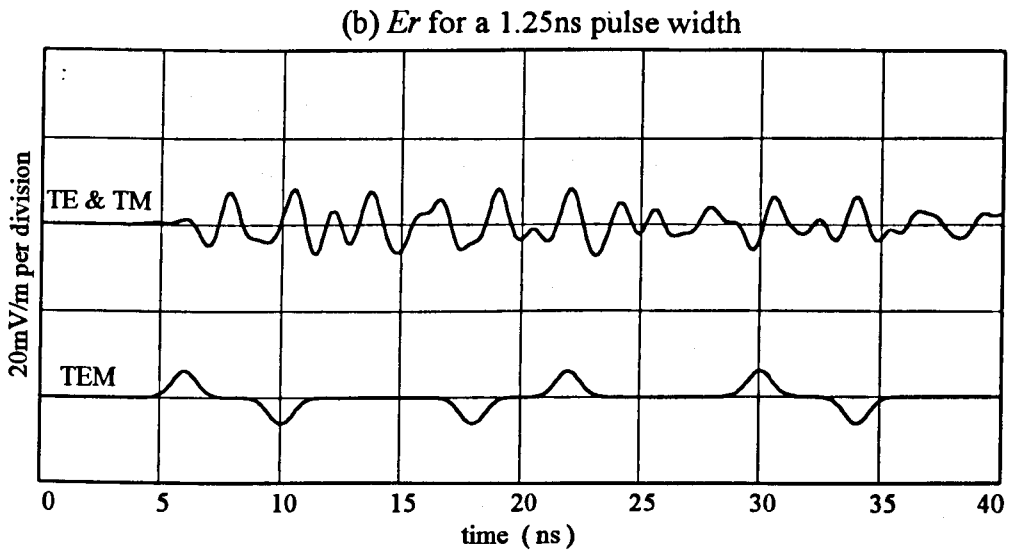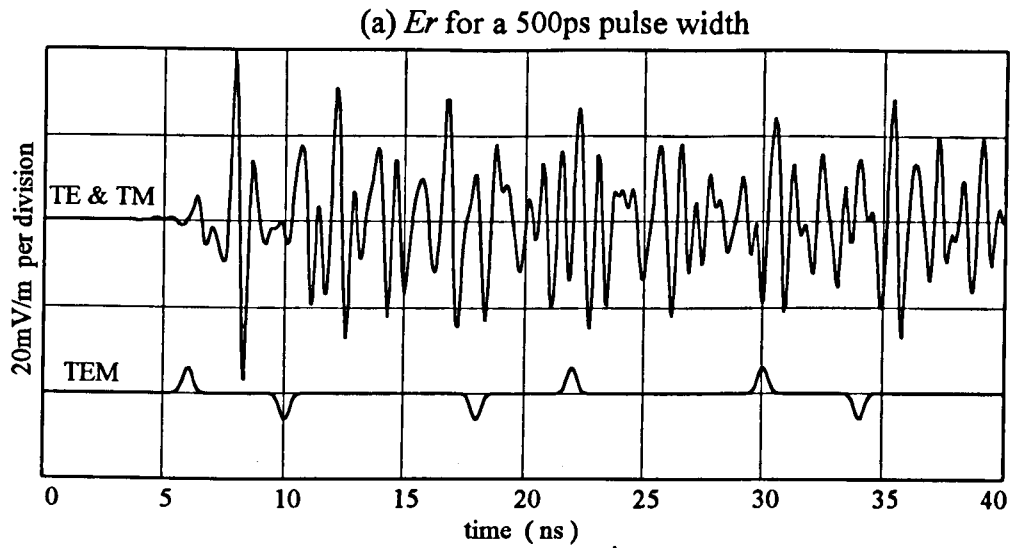
Figure 5.17 Simulation results comparing the TE/TM and the TEM mode
contributions to the electric field *Er* at *z*=1.2m with φ=0.
(a) For a Gaussian PD pulse of half-amplitude width 500ps,
(b) For a Gaussian PD pulse of half-amplitude width 1.25ns.
In both cases the PD source is located in the central plane of the
chamber, with a path length of 10mm and a peak current of 2.0mA.

the electric field is lower. Making the coupler larger to counteract this effect would have the undesirable consequence of increasing the amount of low frequency noise coupled from the GIS. Measurements of the PD current pulses generated by small defects such as particles and protrusions in SF_6 give typical values of less than 500ps for the half-amplitude width. Simulations indicate that for the short PD pulses typical of small defects, limiting PD detection to VHF frequencies (TEM mode only) results in the majority of the available signal power being lost.

5.6.3 Signal-to-noise ratio and coupler location

Experiment and simulation both show that the maximum UHF power is obtained when the coupler and defect are 'in line', rather than having an angular displacement. This is caused by superposition of identical signals at angles of $\phi=0$ and $\phi=\pi$, because of the symmetry about the source at these positions. The power available is typically twice that measured at an angular displacement of $\phi=\pi/2$. The majority of the noise signals in GIS (such as conducted noise from external air corona) are concentrated at lower frequencies, below the cut-off frequency of the dominant TE_{11} mode. The only mode in which this noise can propagate is the TEM mode, and there will be no variation in this noise signal level with the coupler angle ϕ. The coupler mounting angle should therefore be chosen to maximise the UHF signal power. Some defects occur at angular locations that cannot be predicted, and these cannot be anticipated when placing the coupler. However, one of the more common sources of PD and causes of GIS failure is the presence of free metallic particles. These will be located at the bottom of the chamber, moving about on the outer conductor under the influence of the HV field. In the absence of any other motive for locating the coupler at a particular angle, the best coupler locations for detecting these particles would be either along the bottom or the top of the GIS.

The effect which changing the angle between the source and the coupler has on the UHF signal arises because the ratio in which the modes are combined varies, since

their amplitudes are proportional to *cos(nϕ)*. Signals propagating in modes for which *n* is even will arrive in phase at diametrically opposing couplers. Signals in odd order modes will be in antiphase at these locations. This suggests the possibility of using a pair of matched couplers mounted on opposite sides of the waveguide. Addition or subtraction of the signals using a broadband passive circuit could allow the selection of certain modes while rejecting others. For example, subtraction of the signals would attenuate the TEM mode, reducing the transient levels to which the sensitive UHF receiver may be subjected. Attenuation of the TEM mode would also reduce the background noise levels and improve the signal-to-noise ratio of the PD detection system. When using portable monitoring equipment with external couplers at barriers [68], some information about the angular location of the PD source could be obtained by using two couplers to simultaneously monitor the signal level at various positions around the barrier.

5.6.4 Evaluation of the frequency-domain technique

The use of FFT processing and frequency-domain modelling of the transfer function between a source current pulse in the coaxial chamber and the digitised record of the coupler output has demonstrated excellent agreement between the measured and simulated UHF signals. The coaxial Green's functions and the theoretical development presented in Chapter 2 have been verified in their application to this problem.

An increased number of modes can be used in the simulation because the numerical processing is faster than the time-domain approach used in Chapter 4. The total length of the response that could be simulated in the chamber was again limited by the finite number of reflections that can be included. Each reflection path requires sampling of the mode transfer functions as they are dependent on the distance travelled by the signal. For the simulations carried out in this chapter, 26 modes were included, and the time taken to generate a complete 40ns simulation record was

about 20 minutes. Most of this time was consumed in sampling the complex frequency-domain transfer function vectors which are then summed to give the overall sampled transfer function. However, unlike the time-domain simulation, the input pulse is defined separately from the waveguide transfer function equations. Consequently, once the transfer function data has been generated, the response to different excitation pulse shapes can be determined in a few seconds when the physical configuration of source and coupler remains unchanged.

Symmetry of the coaxial line around the PD source causes larger UHF signals to appear 'in line' with the direction of the radial PD current. The development of 'two-dimensional resonances' has been explained in terms of the propagation of electromagnetic wavefronts inside the coaxial chamber. The effects of circumferential propagation around the outer wall of the chamber were predicted by the model and observed during the experiments.

6. USING THE MODEL TO STUDY UHF SIGNAL ENERGIES

6.1 Introduction

The ability of the frequency-domain simulation process to predict changes in the UHF signal energy in a variety of source and coupler configurations has been demonstrated in Chapter 5. In this chapter, the model will be used as a tool to study the effects of various parameters on the UHF signal. Changes at the PD source are of most interest in their effect on the UHF signal because they are usually unknown in a measurement situation and can vary considerably. In contrast, factors such as the GIS dimensions and the coupler frequency response are fixed by design. The PD source parameters to be investigated include the effects of:

- length of the PD current path,

- duration of the PD pulse,

- position of the PD source,

- multiple PD pulses.

The effects of signal reflections will not be included as they are specific to a given configuration of GIS components. The total signal results from the superposition of multiple signals that have travelled different distances. However, each of these signals has an amplitude proportional to that of the original signal excited in the uniform line. A comparison of the signals excited in a uniform coaxial transmission line (free from reflecting obstacles) is therefore relevant to situations where reflections do occur.

6.2 Standard Conditions for the Simulations

UHF signals are best compared by simulating the cumulative energy delivered by the coupler to the measurement system over a representative period of the UHF signal. In the case of a transmission line that is free from reflections, most of the energy is delivered within the first 200ns. *The following conditions apply to all the simulations presented in Section 6.3:*

- inner and outer GIS conductor radii are 0.05m and 0.25m,

- the PD current pulse has a Gaussian shape, a magnitude of 1pC, flows in the radial direction and is centred on t_0=5.0ns,

- the UHF coupler is a 25mm monopole probe at a distance of z=4m from the PD source,

- the measurement system has an input impedance of 50Ω and a first order lowpass frequency response with a 3dB cut-off frequency of 1.1GHz,

- all modes with cut-off frequencies below 2GHz have been included in the simulations.

This configuration is depicted in Figure 6.1. In each of the plots of UHF energy, the time scale has been normalised to remove the propagation delay time of z/c. Therefore t=5.0ns corresponds to the theoretical arrival time of the peak of the PD pulse given a propagation velocity c in the z-direction. The energy levels have also been scaled relative to the results for the following standard conditions at the PD source:

- half-amplitude pulse width of w=500ps,

- PD current path of length ℓ =10mm,

- PD path at outer conductor, from r_1=0.250m to r_2=0.240m (r' =0.245m),

- angular displacement of ϕ=0 between coupler and PD source.

Uniform section of 400kV GIS:
Inner conductor radius = 0.05m,
Outer conductor radius = 0.25m.

4.0m

Location of the
PD source

Location of the
UHF coupler

Measurement
system
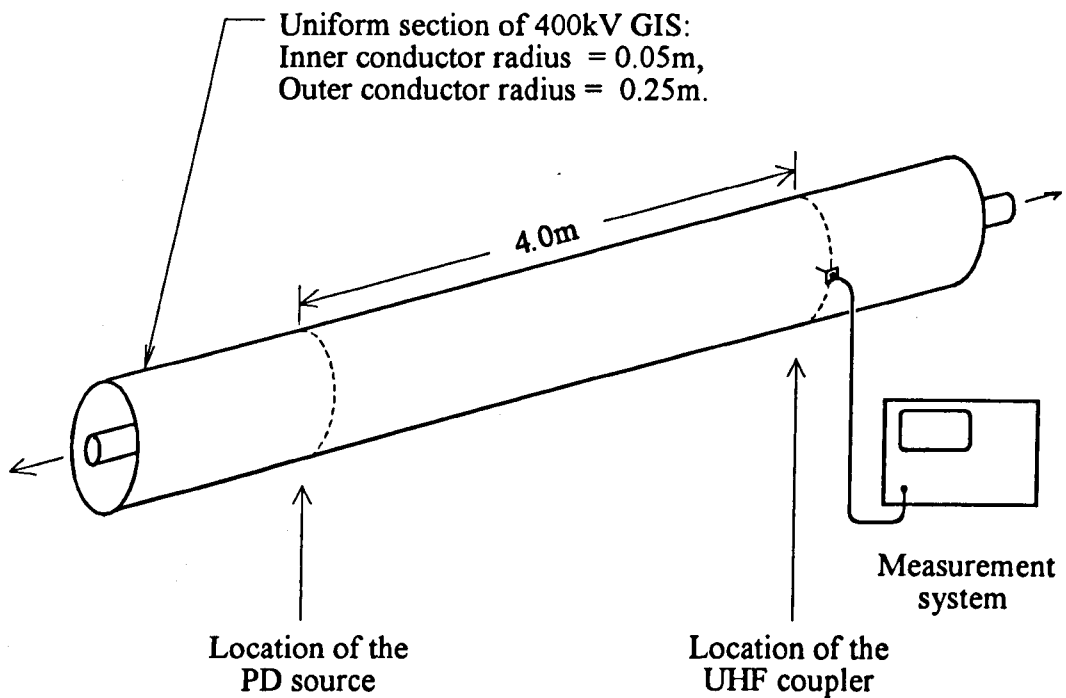
Figure 6.1 A uniform coaxial section of GIS fitted with a UHF coupler
and PD measurement system. Simulations based on this
configuration were used to investigate changes in the UHF
signal energy as parameters of the PD source were altered.

The PD current pulse, simulated UHF signal at the coupler output and the cumulative energy for these standard conditions are shown in Figure 6.2 for reference.

6.3 Simulation Results

6.3.1 Length of the PD current path

Standard conditions that apply: w=500ps, ϕ=0.

Figure 6.3(a) shows the simulation results for a PD current path of varying length ℓ. One end of this current path is fixed at the outer conductor (r_1=0.250m) while the other end advances towards the inner conductor. Although lengths over a few tens of millimetres are unrealistic for protrusions in GIS, the variation of the UHF signals follows the trend of empirical results [41,69]. The relative energies of the signals are compared in Figure 6.3(b). As the energy is proportional to the square of the signal amplitude, the square root of the energy levels is also plotted against ℓ. This shows that for lengths up to about 80mm the amplitude of the UHF signal is proportional to the length of the current path. For longer paths the relationship departs from a linear one. This is due to changes in the excitation sensitivity of the modes with radial position, as described in Section 5.3.2.

6.3.2 Duration of the PD pulse

Standard conditions that apply: ℓ=10mm, r'=0.245m, ϕ=0.

The UHF signal is highly sensitive to the rate of change of the current pulse. This has been investigated by simulating the response to Gaussian current pulses of
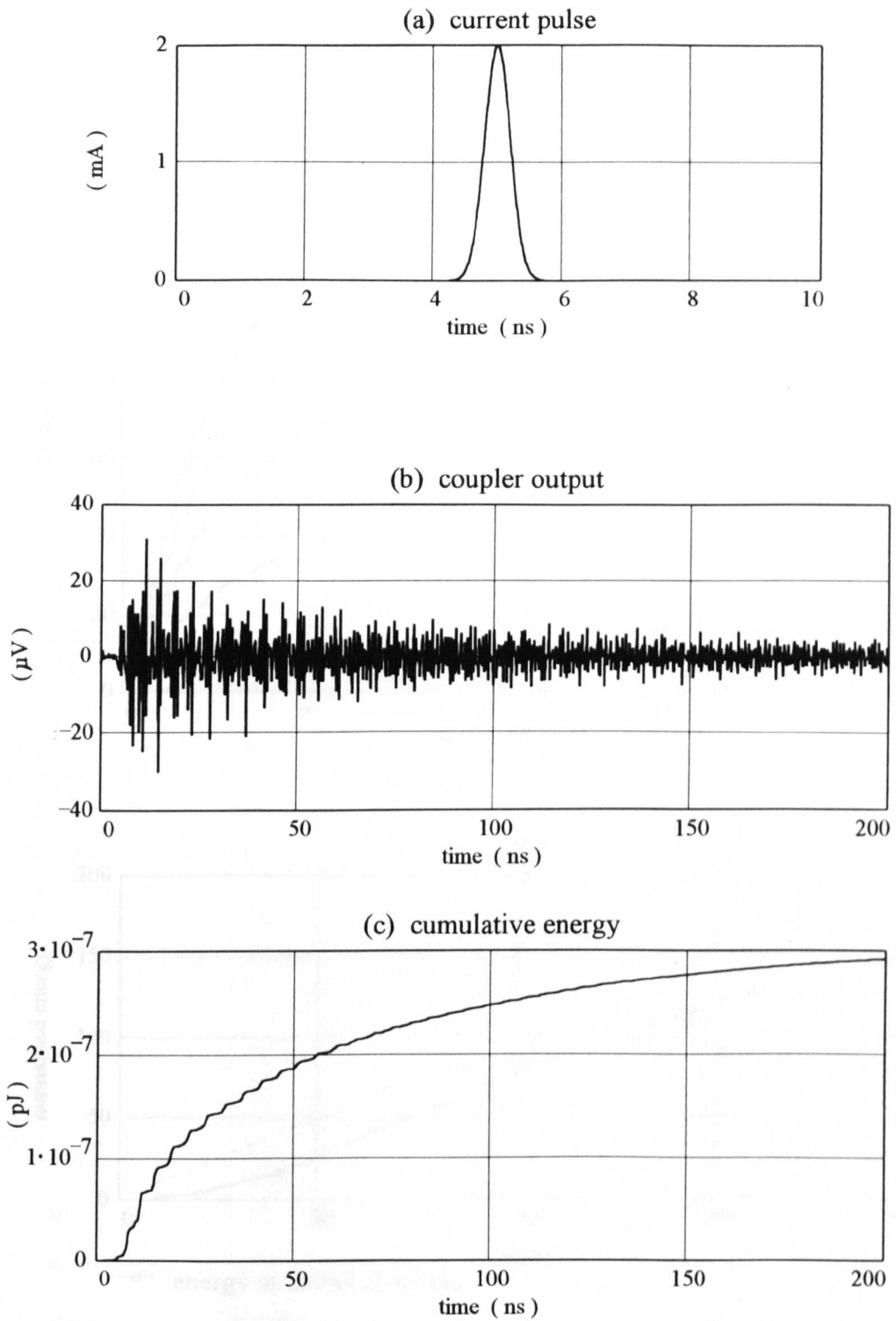
Figure 6.2   Illustration of the standard conditions used for the energy simulations.
(a) 1pC Gaussian current pulse centred on t_0=5ns.
(b) UHF output from the coupler 4m away.
(c) energy delivered from the coupler to a 50Ω load.
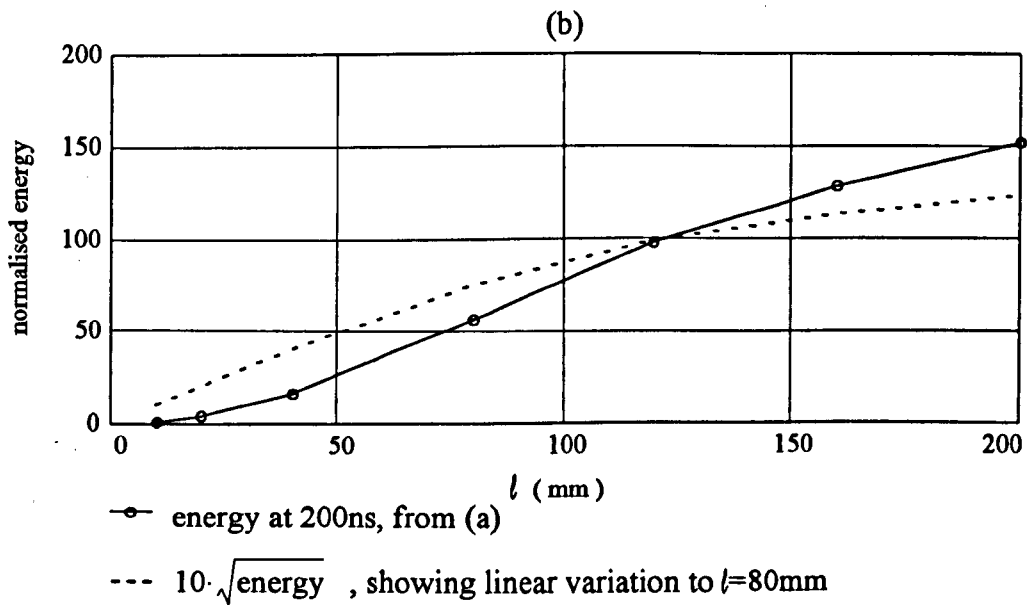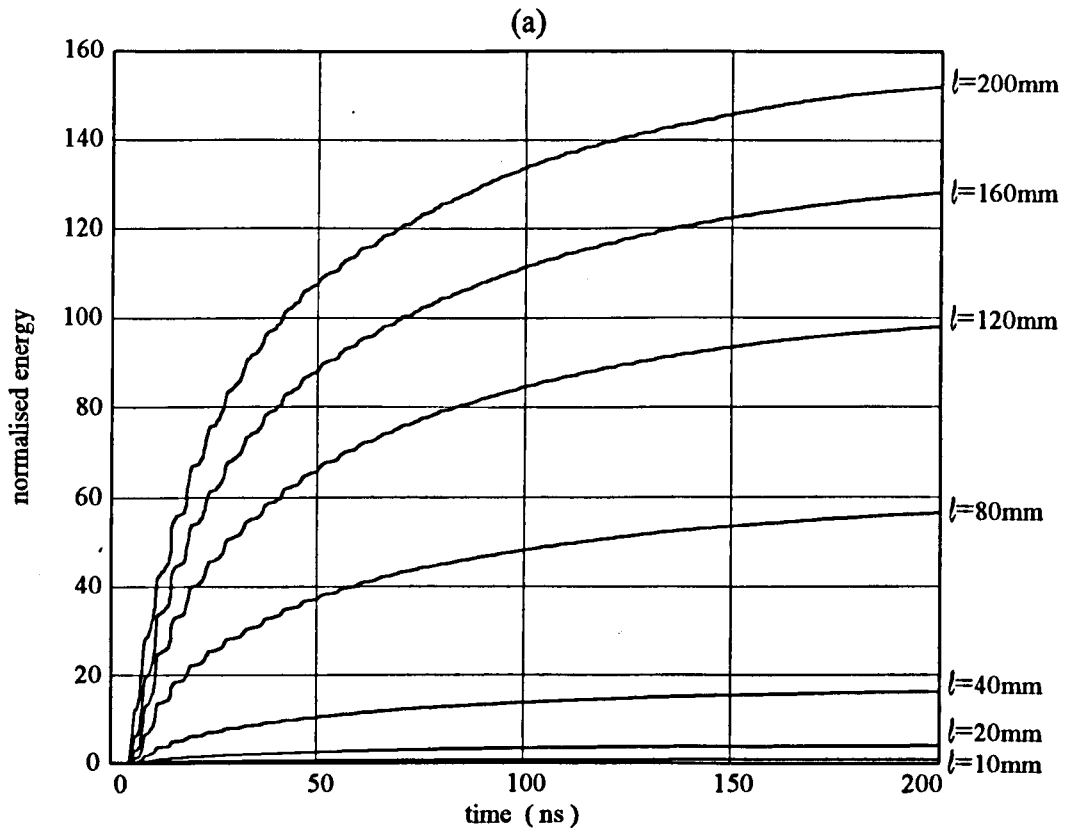
Figure 6.3   UHF energy as a function of the PD current path length l.
(a) Energy plotted against time for each path length simulated.
(b) Cumulative energy at t=200ns as a function of l.

constant total charge but varying half-amplitude widths w. The results in Figure 6.4 show that the signal energy increases rapidly as the pulse width decreases. This is due to a combination of three factors:

1) As the rate of rise of the current pulse increases, a larger portion of the pulse spectrum exceeds the cut-off frequencies of the higher order modes. More energy is therefore able to propagate within the GIS and contribute to the UHF signal at the coupler.

2) Maintaining a constant charge magnitude for the pulses requires the peak current amplitude to be inversely proportional to w. The higher current amplitudes for shorter pulses increase the amplitude of the UHF signal.

3) The coupler response is proportional to the time derivative of the electric field, which will be greater for pulses with higher rates of change.

Each of these amplitude effects is exaggerated by the squaring involved in calculating the signal energy.

6.3.3 Position of the PD source

Standard conditions that apply: w=500ps, ℓ=10mm.

The effect of the position of the PD source was investigated by simulating the UHF signal generated by a PD source whose angular displacement and radial position were varied in the transverse plane. Figure 6.5 shows the variation with ϕ when the midpoint of PD path is located at r'=0.245m (a 10mm PD path at the outer conductor). Note the similarity with Figure 5.12 for the coaxial test chamber, with peaks occurring at ϕ=0° and ϕ=180°. Figure 6.6 shows the variation with r' when ϕ=0°. The variation in signal energy of approximately 4:1 corresponds to a 2:1 change in the amplitude of the UHF signal with the radial position of the PD source. Under these conditions the maximum energy occurs when the PD is located at the outer conductor.
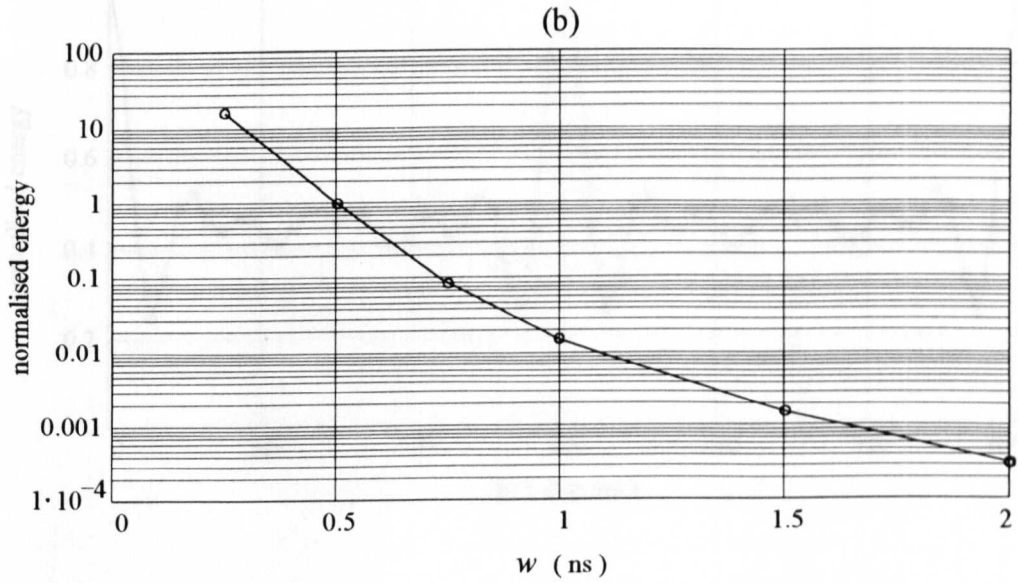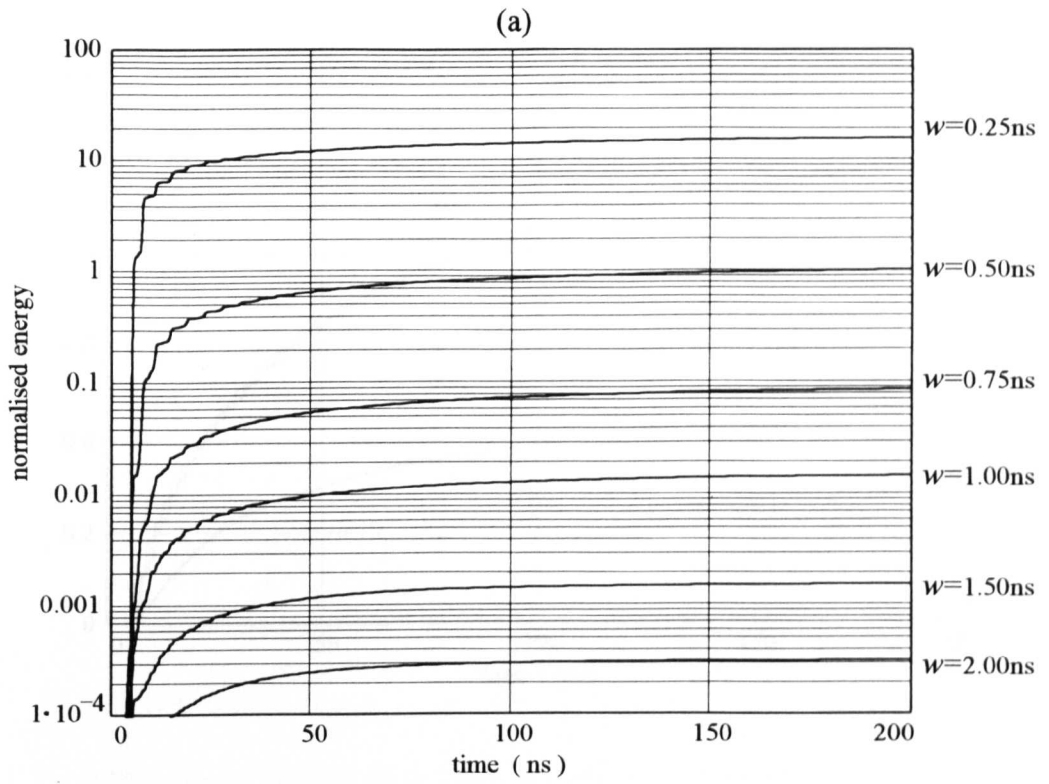
Figure 6.4   UHF energy as a function of pulse width w.
(a) Energy plotted against time for various pulse widths.
(b) Cumulative energy at t=200ns as a function of w.
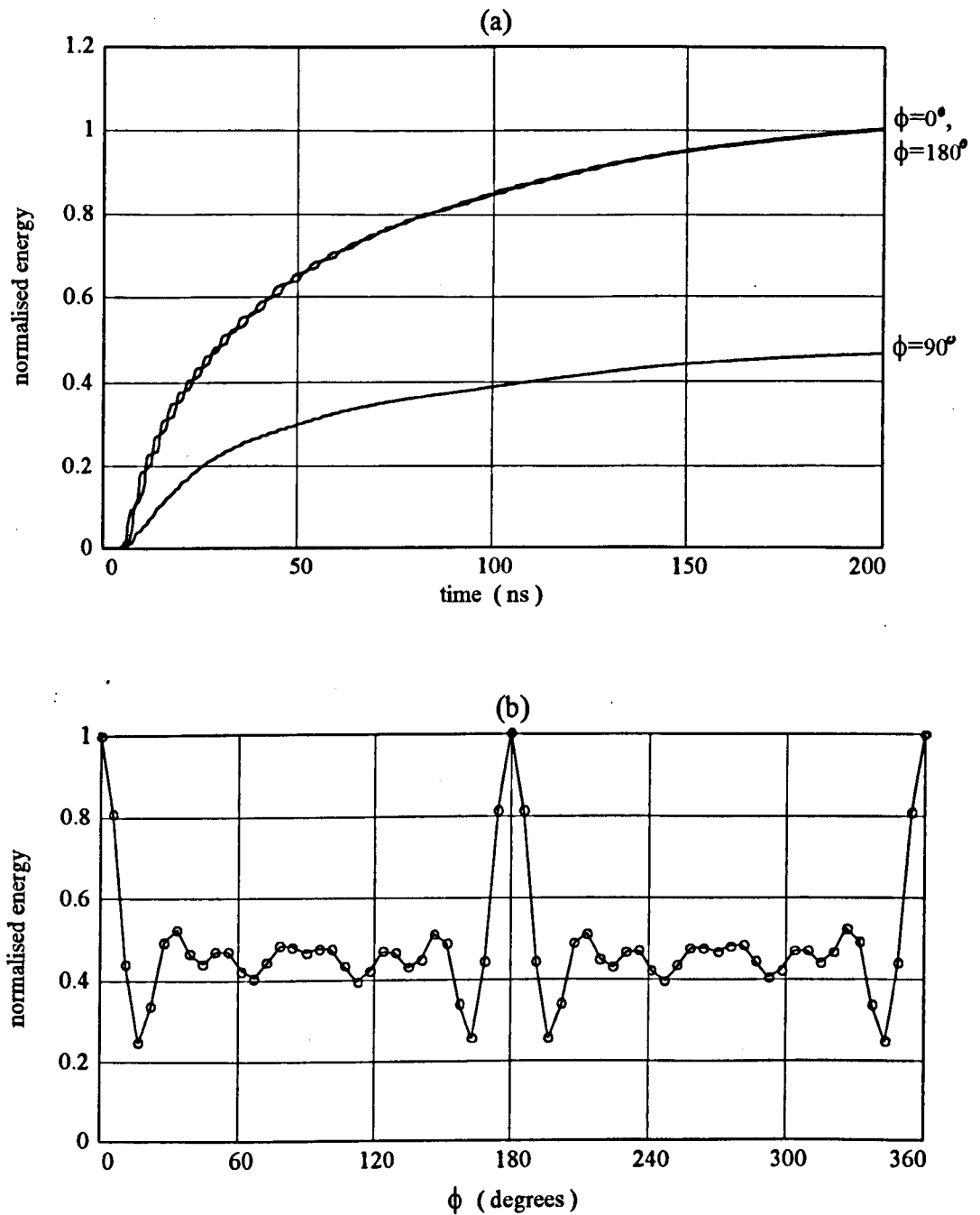
Figure 6.5   UHF energy as a function of angular displacement φ in the
transverse plane. (a) Energy plotted against time for three of the
angular displacements. (b) Cumulative energy at *t*=200ns as a
function of φ.
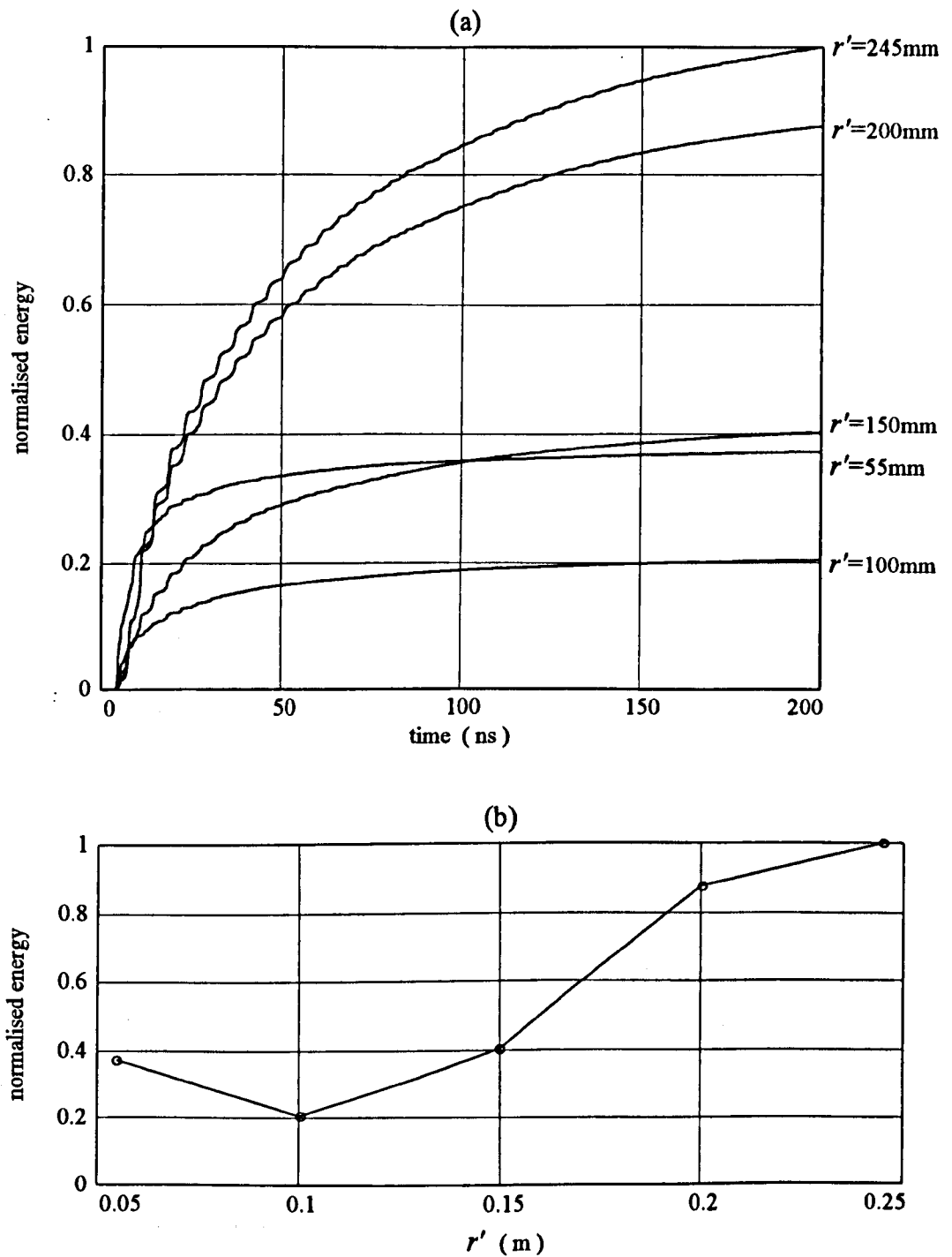
Figure 6.6   UHF energy as a function of radial position for a PD current path of
length l=10mm.
(a) Energy plotted against time for various radial positions.
(b) Cumulative energy at t=200ns as a function of radial position.

The UHF electric field patterns at the coupler result from the superposition of wavefronts arriving by many reflection paths inside the waveguide. Therefore we should expect that the interference patterns which cause variations in the signal energy with the location of the source will not be independent of the PD pulse width. This proves to be the case, and is illustrated by the following examples in which the pulse width has been increased by a factor of 2.

Standard conditions that apply: w=1.0ns, ℓ=10mm.

Figure 6.7 shows the variation in signal energy with angular displacement for the longer pulse, for comparison with Figure 6.5(b). Figure 6.8 shows the variation with radial position, for comparison with Figure 6.6(b).

6.3.4 Multiple PD pulses

Standard conditions that apply: w=500ps, ℓ=10mm, r'=0.245m, ϕ=0.

Often multiple PD pulses are generated in quick succession by a defect such as a protrusion [19], and the resulting UHF signals overlap. In these circumstances it is useful to know how the total signal energy is affected. Two patterns of multiple pulse occurrence have been investigated. Firstly, two identical 1pC current pulses with a variable separation were simulated. The resulting energies are shown in Figure 6.9. Secondly, a variable number of 1pC pulses with a fixed separation were used for the current source, with the results shown in Figure 6.10. Some variation depending on the pulse separation and number of pulses is evident, but there is no great departure from linearity.
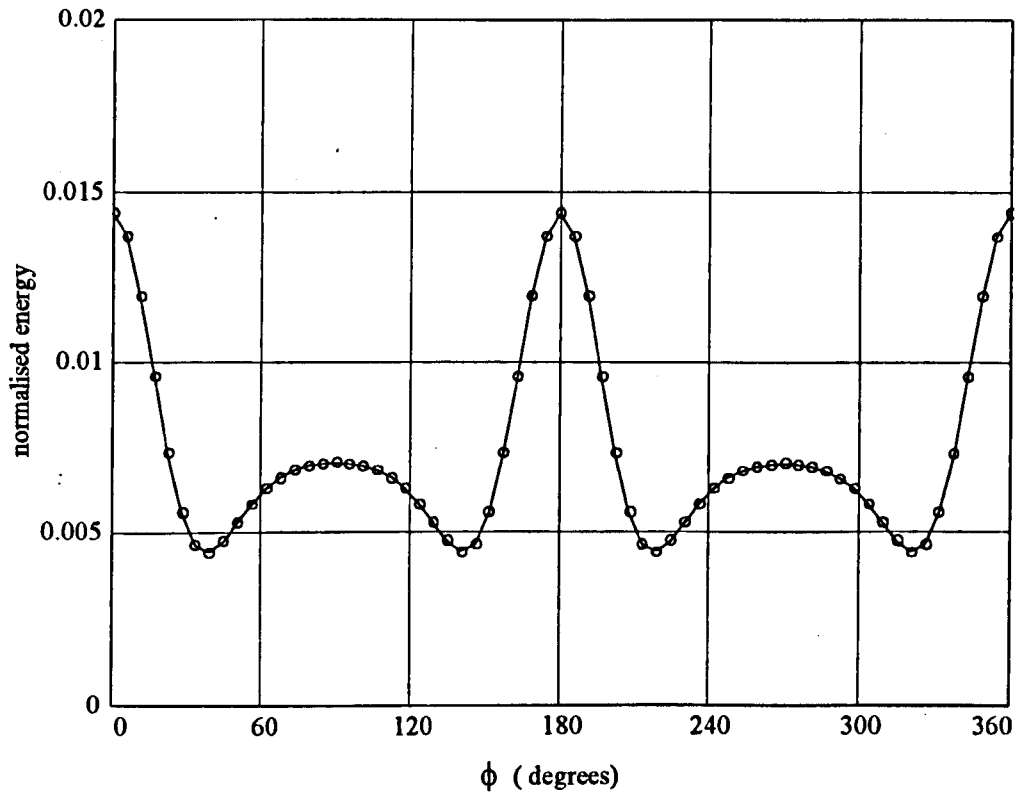
Figure 6.7   UHF energy as a function of angular displacement ϕ for a PD
pulse width of w=1.0ns rather than the value w=500ps used
to generate Figure 6.5(b).
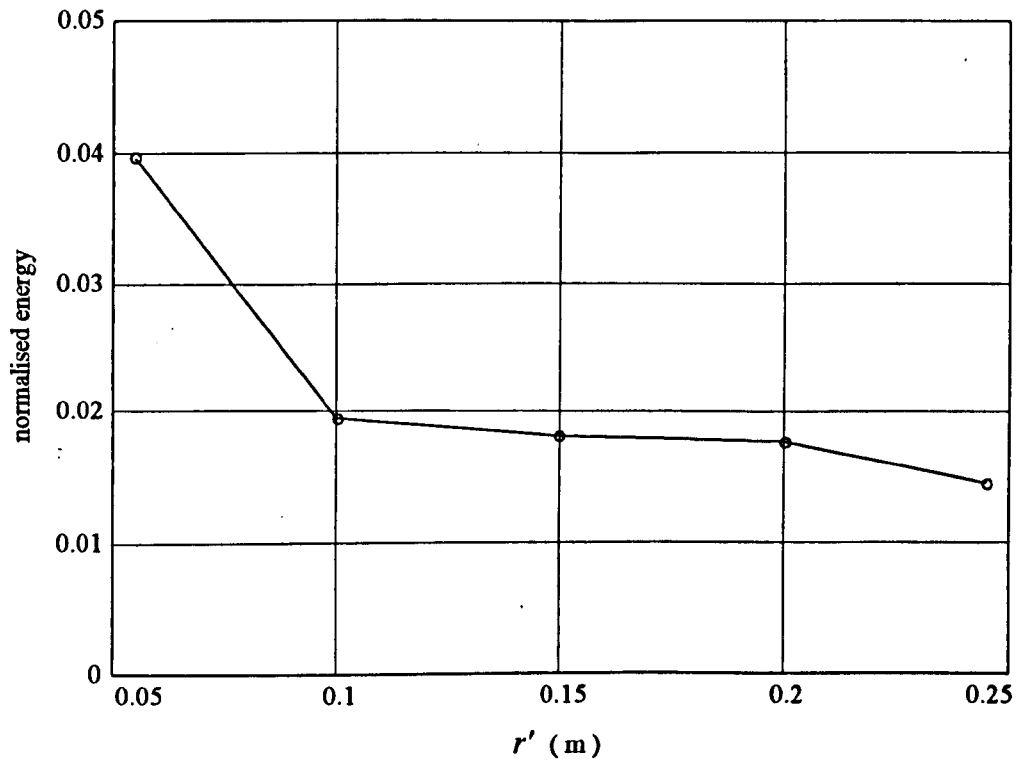
Figure 6.8   UHF energy as a function of radial position r' for a PD pulse
width of w=1.0ns rather than the value w=500ps used to
generate Figure 6.6(b).
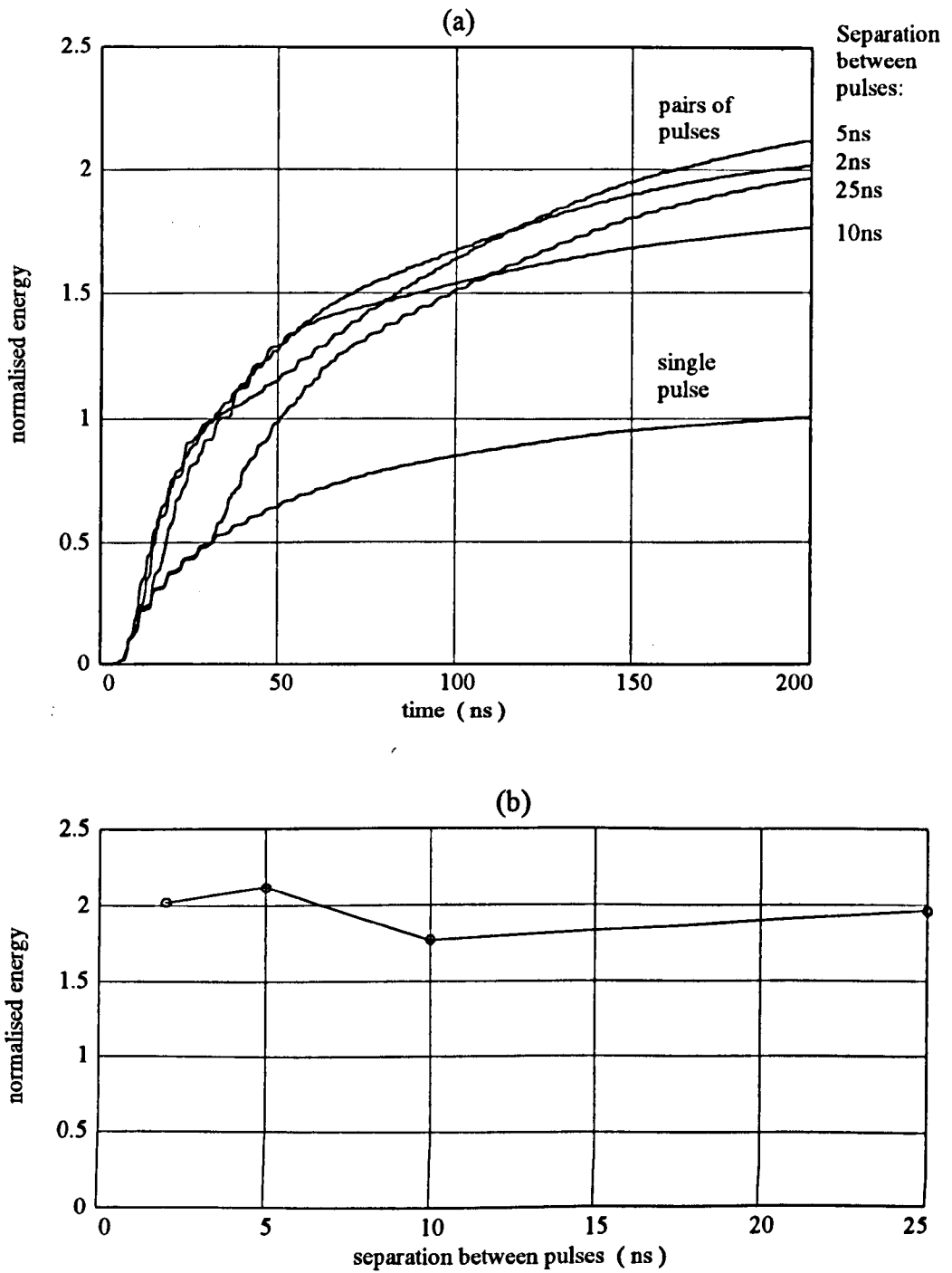
Figure 6.9   Variations in UHF energy for pulse pairs with variable separation.
(a) Energy plotted against time, for a single pulse and pulse pairs.
(b) Cumulative energy at t=200ns as a function of pulse separation.
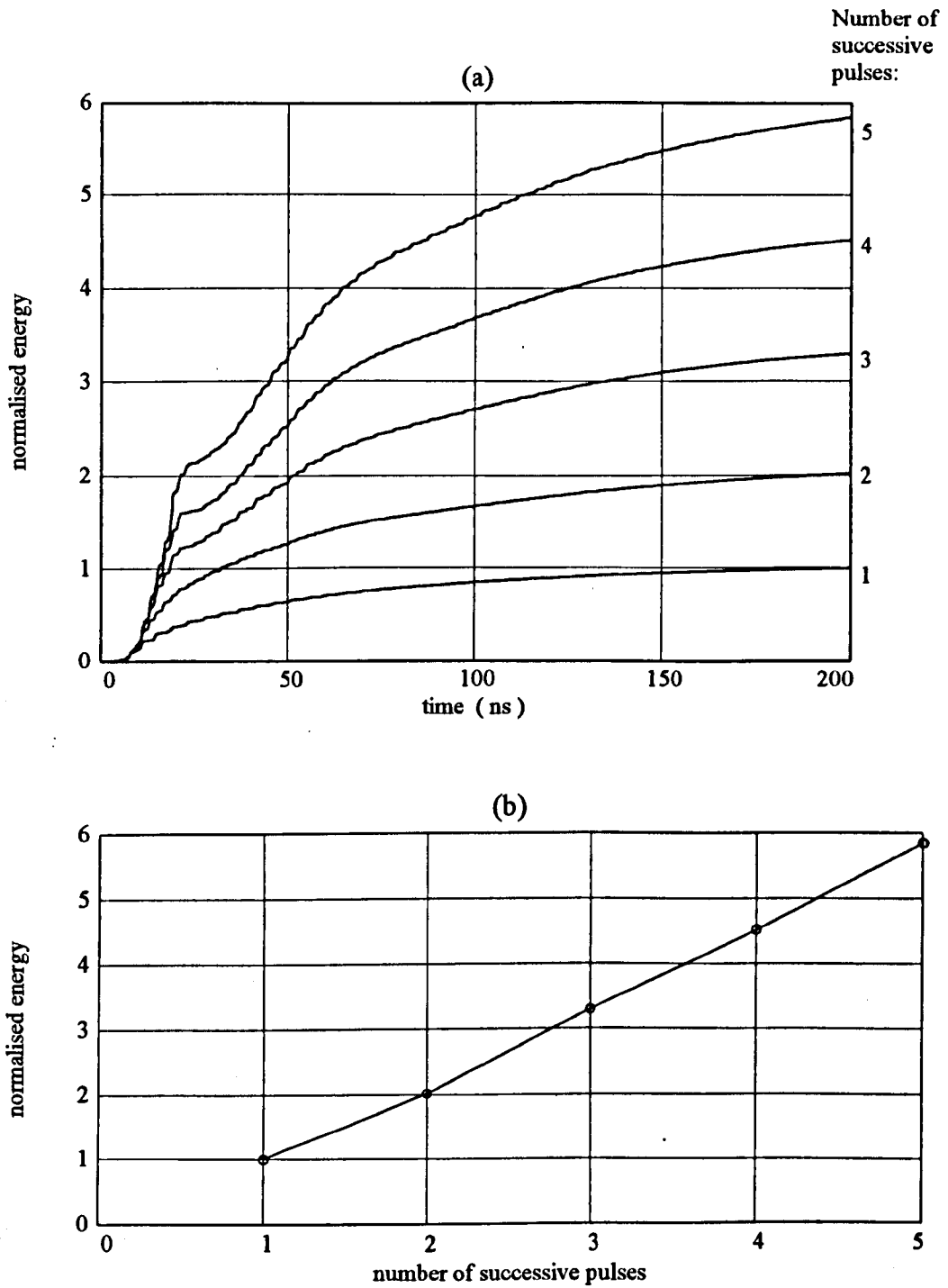
Figure 6.10   Variations in UHF energy with the number of successive PD pulses.
(a) Energy plotted against time for 1 to 5 pulses spaced 2ns apart.
(b) Cumulative energy at t=200ns as a function of the number of pulses.

The theoretical analysis in Chapter 2 showed a linear relationship between the current amplitude and the amplitude of the UHF signal if all other factors remain constant. This is an obvious consequence of the linearity of the system under these conditions. In Section 6.3.1 we have seen that for small path lengths, the UHF signal amplitude is also proportional to the path length. This leads to the conclusion that for small PD sources, the UHF energy is proportional to the *charge* × *path length* product for a given pulse shape and configuration of source and coupler. As this product represents a fundamental limit to the information available from the UHF signal energy, the detection threshold of a UHF PD measurement system should be specified in these terms.

Figure 6.4 shows that the UHF technique is only suited to the detection of fast PD pulses. For example, increasing the width of the 1pC Gaussian pulse by a factor of four from $w=0.5$ns to $w=2.0$ns causes a decrease in UHF signal energy of more than three orders of magnitude. Such signals are unlikely to be detectable unless the currents involved are very high or the path length is long. For more typical small PD sources, a reasonable estimate of the cut-off point for UHF detection would be 1.0ns pulse width. This figure must be used with caution because the critical factor is the maximum rate of change of the current rather than the pulse width. However, for smooth pulses, such as those shown in Chapter 2 for PD on the needle, these parameters are related.

Figures 6.5 and 6.7 confirm that the maximum UHF energy is available at angular positions that are 'in line' with the direction of the PD current flow. The peaks in signal energy at $\phi=0°$ and $\phi=180°$ broaden as the pulse width increases, although the ratio of the energy at these angles to that at $\phi=90°$ remains at around 0.5. For very long pulses the peaks would be expected to merge, ultimately resulting in no measurable angular variation. This corresponds to the low frequency case of TEM mode propagation. A similar effect can be seen in the variations of signal energy

with radial position of the PD source. The energies predicted for the longer pulse (Figure 6.8) show a pattern of variation that is much closer to the low frequency TEM mode sensitivity curve (Figure 5.6) than that of the shorter pulse (Figure 6.6). The general conclusion that may be drawn from Figures 6.5-6.8 is that the effects of PD location are not independent of the pulse width.

When multiple PD pulses occur, Figures 6.9 and 6.10 indicate that the total UHF energy can be approximated by summing the individual contributions. Identical pulses have been used in the simulations, as these were considered most likely to result in signal cancellation, giving a non-linear response. When a single pulse in a group is much larger than the others, the UHF energy will be primarily dependent on that one pulse.

The results that have been presented in this chapter illustrate the complexity of the UHF signals and the factors affecting them. While there may be no method of working backwards from the UHF signal to arrive at a description of the PD source, the ability to carry out the reverse process could be useful when some of the other unknowns are eliminated. For example, a free particle in a GIS can be identified by the characteristic point on wave pattern of its PD. The location of the defect in the transverse plane when the PD takes place is at the bottom of the outer conductor, where the particle falls due to gravity. The current pulse shape is primarily governed by the physics of the SF_6 gas, and studies of the pulse shapes at typical gas pressures may restrict them to a narrow range. In these circumstances, if the coupler response is known, a measurement of the *charge × path length* product may be possible. A more useful application of the model would be in a study of the worst case signal levels given a specified minimum *charge × path length* product that must be detectable anywhere within the GIS. This topic will be discussed in more detail in Chapter 7.

7. GENERAL CONCLUSIONS AND RECOMMENDATIONS FOR FURTHER WORK

7.1 General Conclusions

Techniques for detecting the PD caused by defects in GIS have been reviewed, showing that the UHF method is the most practical option when continuous, sensitive diagnostic monitoring required. The true charge flowing at the defect site is not directly measured by either conventional PD measurements to IEC270 or UHF measurements. However, the principles of the conventional method have been explained, and this has led to its general acceptance. The purpose of this work was to redress the balance by explaining the processes involved in the UHF technique.

Green's functions for the electric field were used in the analysis of the UHF signals, and the PD was treated as a current source inside a cylindrical waveguide. A hollow cylindrical chamber was first used to test the suitability of this approach. The radial component of electric field at the wall of the chamber was measured using a probe coupler with a known response. The response of the chamber to a Gaussian current pulse excitation was approximated by mathematical expressions in the time-domain. Using a needle PD test cell, the excitation current pulses could be recorded together with the corresponding UHF signal. The current pulses were approximated by similar Gaussian pulses so that the UHF signals could be simulated by numerical evaluation of the contributions from each of the propagating modes. Agreement between the simulated and measured UHF signal energies was within the limits imposed by experimental error and the approximations made in the theory. The success of this preliminary work prompted the subsequent more rigorous modelling of the coaxial configuration.

During the experiments, a simple method for simulating PD pulses on a protrusion was developed. A CMOS driver circuit and a monopole probe were used to generate current pulses that compare well with real PD pulses in SF_6. This method can be

used to generate current pulses having peak amplitudes of up to 2mA, equivalent to charge transfer levels of about 1pC. This technique could be used for calibrating UHF couplers in terms of a minimum detectable defect. Larger currents could be obtained by switching a higher voltage in similar transition time, using an avalanche transistor circuit, for example.

The theoretical model and FFT simulation process developed for the coaxial chamber resulted in excellent agreement with measured UHF signals, allowing the characteristics of pulse propagation to be explained. A variety of configurations of source and coupler were tested, with the excitation probe mounted at the outer and inner conductors. Having demonstrated the accuracy of the model, it was then used to study the effect that altering various parameters of the PD source has on the UHF signal at the coupler.

There is a fundamental limitation of proportionality to the product *charge × path length* in the amplitude of the UHF signal. A measurement of UHF signal power is not sufficient to define the charge magnitude of the PD without additional information about the PD source. However, other techniques, such as point on wave analysis, can give considerable useful information concerning the source parameters. The UHF signal power should be representative of the *charge × path length* product of the defect when a reasonable estimate of the UHF transfer function can be made.

The most critical factor determining the UHF signal level is the maximum rate of change of the PD current. Variations in UHF power with location of the PD source in the transverse plane are also pulse width dependent, but to a lesser extent. The types of low level PD that can be detected by the UHF method will be those which involve current risetimes of less than 1ns. In practice, the pulse risetime will be limited to a narrow range by the physics of PD in SF_6.

The theoretical development has concentrated on relating the radial component of PD current to the radial electric field at the coupler. However, any other components

can be analysed in the same way, yielding similar functions of time and position. When couplers are mounted close to the outer conductor, the boundary conditions on the electric field lead to the radial component being predominant in determining the coupler response. The field pattern is dependent on the GIS dimensions, so the best way to standardise the measurement of coupler response would be to mount the couplers in a flat ground plane and subject them to an electric field normal to the plane. In this way, the coupler response could be measured in a configuration that is similar to the situation in GIS.

Calculation of the theoretical losses in aluminium waveguide has shown that quoted figures in the region of 2dB/m for the attenuation of UHF signal are too high to be caused by the skin effect. The attenuation in GIS is better accounted for by the reflection of significant fractions of the signal energy at discontinuities. The sections of uniform transmission line between discontinuities can be regarded as separate chambers that 'leak' energy to adjacent chambers.

The contribution made by the TEM mode to the electric field at the coupler has been compared to that from higher order propagating modes. For PD pulses occurring in GIS, which typically have risetimes of less than 500ps [70], the energy available in the UHF range is much greater than that in the VHF (TEM mode only) range. Broadband UHF monitoring is therefore to be preferred when maximum sensitivity is required.

The development of 'two-dimensional resonances' has been explained in terms of the propagation of electromagnetic wavefronts around the circumference of the coaxial chamber. Symmetry of the coaxial line around the PD source causes larger UHF signals to appear 'in line' with the direction of the PD current. Location of couplers in the vertical plane has been proposed, to give the best signal-to-noise ratio for detecting free particles. There may be possibilities for using the angular variations of the electric field patterns to determine the angular location of the defect.

This work provides a foundation for an understanding of the UHF technique, particularly with regard to the aim of standardising UHF PD measurements. The same theoretical analysis could be applied to other situations where PD takes place within the insulation system of a coaxial line, for example, in gas insulated transmission lines (GITL). Improved understanding of the UHF signals generated by PD is likely to lead to increased sensitivity and better signal interpretation techniques. A proper assessment of the capabilities of UHF diagnostics for applications such as GIS commissioning tests will require standard definitions of system sensitivity.

7.2 A Scheme for Standardising UHF PD Detection in GIS

7.2.1 Background

At present there is no standard approach to UHF measurements of PD and a variety of couplers and monitoring systems have evolved. Consequently, comparison of measurements obtained using different systems or recorded during experimental work has not been possible. The most important aspect of defect detection in GIS is to ensure that the whole substation is monitored with a sensitivity capable of detecting the smallest PD that is considered to be critical. The level of PD activity that represents a significant risk depends on the nature of the defect (protrusion, particle, floating electrode, etc.). However, the lowest PD level from a critical defect is likely to be that due to a small protrusion on the busbar. This will be referred to as the *critical PD level*. This level has been quantified as an apparent charge of 1-2pC using conventional measurements [18]. Some knowledge of the *excitation*, *propagation* and *extraction* transfer functions (defined in Figure 2.1) for the complex structure of a real GIS is important if UHF monitoring systems are to be properly designed. The scheme described below is proposed to address this requirement.

7.2.2 Critical PD level

The critical PD level can be conveniently defined for a UHF monitoring system in terms of a *charge × path length* product for a defined current pulse shape, as described in Section 6.4. The pulse shape should be typical of the current pulses caused by small defects in SF_6. A value for the *charge × path length* product could be estimated using published figures for a protrusion [18], but care is required since the UHF theory is based on real charge flow, as opposed to apparent charge. The UHF electric field at a remote coupler location could then be determined by simulation, using the critical defect as the PD source. This is the electric field to which the coupler would be subjected if the intervening transmission line was uniform.

7.2.3 Propagation through the GIS

Propagation of UHF signals within the GIS is impeded by obstacles such as barriers, corners and junctions, which are difficult to analyse theoretically. The attenuation caused by reflections is far more significant than that due to dissipation over the distances involved for UHF couplers, which are seldom mounted at more than 10m from a PD source. To account for these effects, an attenuation figure or frequency response must be associated with each discontinuity. These figures are likely to depend on the PD source and adjacent discontinuities, and worst case values will have to be determined by measurement and simulation. The aim is to obtain a value for the additional attenuation of the electric field that is caused by discontinuities between the PD source and the nearest coupler.

7.2.4 Coupling of the UHF signal

The response of a UHF coupler is dependent on its construction and mounting arrangement. If the response is to be defined, a standard method of measuring the performance of couplers is required. This will allow comparison of different designs

and optimisation of sensitivity, as well as ensuring that a specified response is achieved. An important factor determining the performance of a coupler for use in GIS is its response to an incident electric field normal to the plane in which the coupler is mounted. This is a consequence of the coupler's location close to the outer conductor and the boundary conditions that must be satisfied by the field in this region. The complete transfer function could only be determined for the experiments presented in this work because the transfer function of the probe coupler was known. The coupler output voltage could therefore be obtained from the incident electric field. For practical couplers, such as the disc type [20] designed for the HV environment of GIS, derivation of a theoretical model for the response may not be possible. In these cases, the frequency response could be measured by subjecting the coupler and its mounting (often a recess) to a uniform, normal UHF electric field of known intensity.

7.2.5 Combining the transfer functions

Assessment of a UHF PD monitoring system design for GIS could be achieved by combining the three elements of the transfer function. When a defect is located at the position of maximum signal attenuation relative to the nearest UHF coupler, the detection threshold of the monitoring system must be sufficient to reliably detect PD at the critical level. This scheme for standardising PD measurements using the UHF technique should ensure that a specified critical defect can always be detected.

7.3 Recommendations for Further Work

The following recommendations are made with the aim of addressing the requirement for standardisation of UHF PD measurements:

- A calibration technique for UHF couplers should be defined that will enable utilities and manufacturers to specify the response required and to allow optimisation and comparison of different designs. This study has suggested that the best measure of the coupler transfer function is that relating its output voltage to an incident electric field normal to the coupler mounting plane. The measurement could be accomplished using a parallel plate structure to generate a plane wave, with the coupler mounted in the ground plane. Swept frequency and pulsed FFT excitation techniques should be investigated. As couplers are not usually mounted in a uniform section of the coaxial line, but at window or inspection hatch, the mounting structure should be reproduced in the test facility, as it is likely to have a significant influence on the response.

- The phase variation of the higher order electric fields with angular position around the GIS suggests the possibility of using pairs of matched couplers mounted on opposite sides of the waveguide. The signal propagating in even order modes or the TEM mode would be in phase at these locations, whereas signals in odd order modes would be in antiphase. Addition or subtraction of the coupler signals before subsequent processing would allow selection certain modes while rejecting others, a property which may be useful for improving the signal to noise ratio of a PD detection system [69].

- The effects of discontinuities in GIS on the propagation of UHF signals require considerable investigation to determine the worst case attenuation figures associated with corners, tee-junctions, gas barriers, etc. This work would have to be based mainly on laboratory measurements of attenuation in typical GIS sections, but techniques such as finite element modelling of electromagnetic propagation may also play a part.

8. ACKNOWLEDGEMENTS

Martin D Judd

14 June 1996

9. REFERENCES

[1]   CIGRE WG 23.10, "GIS in service - experience and recommendations",
      CIGRE Paper 23-104, Paris, 1994

[2]   CIGRE Working Group 15-03, "Diagnostic methods for GIS insulating
      systems", paper 15/23-01 presented at the request of Study Committee 15,
      CIGRE, 1992

[3]   A Sabot, A Petit and J P Taillebois, "GIS Insulation Co-ordination: on-site
      tests and Dielectric Diagnostic Techniques, A utility point of view", Stockholm
      Power Tech Conference, Invited paper SPT IS 05-2, pp. 110-117 (Invited
      Speaker's Sessions), June 1995

[4]   R Baumgartner, B Fruth, W Lanz and K Pettersson, "Partial Discharge - Part
      X: PD in Gas-Insulated Substations - Measurement and Practical
      Considerations", IEEE Electrical Insulation Magazine, Vol. 8, No. 1,
      pp. 16-27, January/February 1992

[5]   IEEE Substations Committee, Working Group K4 - GIS Diagnostic Methods,
      "Partial discharge testing of gas insulated substations", IEEE Trans. on Power
      Delivery, Vol. 7, No. 2, pp. 499-506, April 1992

[6]   F Y Chu, "SF_6 decomposition in gas-insulated equipment", IEEE Trans.
      Electrical Insulation, Vol. EI-21, No. 5, pp. 693-725, October 1986

[7]   J S Pearson, B F Hampton and A G Sellars, "A continuous UHF monitor for
      gas-insulated substations", IEEE Trans. on Electrical Insulation, Vol. 26,
      No. 3, pp. 469-478, June 1991

[8]   R Baumgartner, B Fruth, W Lanz and K Pettersson, "Partial Discharge - Part
      IX: PD in Gas-Insulated Substations - Fundamental Considerations", IEEE
      Electrical Insulation Magazine, Vol. 7, No. 6, pp. 5-13,
      November/December 1991

[9]   L G Christophorou and L A Pinnaduwage, "Basic physics of gaseous
      dielectrics", IEEE Trans. on Electrical Insulation, Vol. 25, No. 1, pp. 55-74,
      February 1990

[10] L Niemeyer, "The physics of partial discharges", Int. Conf. on Partial
      Discharge, IEE Conf. Proc. No. 378, pp. 1-4, 1993

[11] J M Braun and F Y Chu, "Novel low-cost SF_6 arcing byproduct detectors for
      field use in gas-insulated switchgear", IEEE Trans. Power Delivery, Vol. 1,
      No. 2, pp. 81-86, April 1986

[12] L E Lungaard and B Skyberg, "Acoustic diagnosis of SF_6 gas insulated
      substations; a theoretical and experimental basis", IEEE Trans. on Power
      Delivery, Vol. 5, No. 4, pp. 1751-1759, November 1990

[13] L E Lungaard, G Tangen, B Skyberg and K Faugstad, "Acoustic diagnoses of
      GIS; field experience and development of expert system", IEEE Trans. on
      Power Delivery, Vol. 7, No. 1, pp. 287-294, January 1992

[14] K Fujii, M Yamada, A Tanaka and K Kurosawa, "Emission spectrum of partial
      discharge light in SF_6 gas", Conf. Record, IEEE Int. Symp. on Electrical
      Insulation, pp. 332-335, 1992

[15] *Partial discharge measurements*, IEC Publication 270, 1981

[16] H J Weber, "Partial discharge measuring techniques", Tettex Instruments
      Information Bulletin 21

[17] O S Ilyenko and Y V Romanenko, "Real charge definition method in seeming
      charge of partial discharge measurements", Proc. 9th Int. Symp. on High
      Voltage Engineering (Graz), Vol. 4, 1995

[18] H-D Schlemper, R Kurrer and K Feser, "Sensitivity of on-site partial discharge
      detection in GIS", Proc. 8th Int. Symp. on High Voltage Engineering
      (Yokohama), Vol. 3, pp. 157-160, 1993

[19] G Wanninger, "Apparent charge measurement in GIS by modern diagnostic methods", paper to be published in European Trans. on Electrical Power Engineering, 1996

[20] M D Judd, O Farish and B F Hampton, "Broadband couplers for UHF detection of partial discharge in gas insulated substations", IEE Proc., Science, Measurement and Technology, Vol. 142, No. 3, pp. 237-243, May 1995

[21] H-D Schlemper, A Vogel and K Feser, "Calibration and sensitivity of VHF partial discharge detection in GIS", Proc. 9th Int. Symp. on High Voltage Engineering (Graz), Vol. 5, 1995

[22] M Oyama, E Hanai, H Aoyagi, H Murase, I Ohshima and S Menju, "Development of detection and diagnostic techniques for partial discharges in GIS", IEEE Trans. on Power Delivery, Vol. 9, No. 2, pp. 811-818, April 1994

[23] B F Hampton and R J Meats, "Diagnostic measurements at UHF in gas insulated substations", IEE Proc., Vol. 135, Part C, No. 2, pp. 137-144, March 1988

[24] B F Hampton, J S Pearson, C J Jones, T Irwin, I M Welch and B M Pryor, "Experience and progress with UHF diagnostics in GIS", CIGRE Paper 15/23-03, Paris, 1992

[25] M Albiez, W Zaengl, K J Diederich and J Meppelink, "Design and calibration of a universal sensor for the measurement of partial discharges and very fast transients in GIS", Proc. 6th Int. Symp. on High Voltage Engineering (New Orleans), paper No. 42.28, 1989

[26] M D Judd, O Farish and B F Hampton, "Excitation of UHF signals by partial discharges in GIS", IEEE Trans. Dielectrics and Electrical Insulation, Vol. 3, No. 2, pp. 213-228, April 1996

[27] B M Pryor, "UHF partial discharge detection in GIS", IERE Workshop on Gas Insulated Substations, Toronto, pp. 5/16-5/25, 1990

[28] J S Pearson, O Farish, B F Hampton, M D Judd, D Templeton, B M Pryor and I M Welch, "Partial discharge diagnostics for gas insulated substations", IEEE Trans. Dielectrics and Electrical Insulation, Vol. 2, No. 5, pp. 893-905, October 1995

[29] A G Sellars, "Interpreting the UHF signals produced by partial discharge activity in GIS", PhD Thesis, University of Strathclyde, 1995

[30] B Fruth and J Fuhr, "Partial discharge pattern recognition - a tool for diagnosis and monitoring of ageing", CIGRE Paper 15/33-12, Paris, 1990

[31] A G Sellars, O Farish, B F Hampton and L S Pritchard, "Using the UHF technique to investigate PD produced by defects in solid insulation", IEEE Trans. on Dielectrics and Electrical Insulation, Vol. 2, No. 3, pp. 448-459, June 1995

[32] A G Sellars, O Farish and B F Hampton, "Assessing the risk of failure due to particle contamination of GIS using the UHF technique", IEEE Trans. Dielectrics and Electrical Insulation, Vol. 1, No. 2, pp. 323-331, April 1994

[33] A G Sellars, O Farish and M M Peterson, "UHF detection of leader discharges in SF_6", IEEE Trans. Dielectrics and Electrical Insulation, Vol. 2, No. 1, pp. 143-154, February 1995

[34] R J Van Brunt, "Stochastic properties of partial-discharge phenomena", IEEE Trans. on Electrical Insulation, Vol. 26, No. 5, pp. 902-948, October 1991

[35] F H Kreuger, E Gulski and W A Sonneveld, "Diagnosis in GIS by statistical analysis of discharges", CIGRE Paper 15/23-04, Paris, 1992

[36] B Fruth and L Niemeyer, "The importance of statistical characteristics of partial discharge data", IEEE Trans. on Electrical Insulation, Vol. 27, No. 1, pp. 60-69, February 1992

[37] E Gulski and F H Kreuger, "Computer aided recognition of discharge sources", IEEE Trans. on Electrical Insulation, Vol. 27, No. 1, pp. 82-92, February 1992

[38] L Satish and W S Zaengl, "Artificial neural networks for recognition of 3-D partial discharge patterns", IEEE Trans. on Dielectrics and Electrical Insulation, Vol. 1, No. 2, pp. 265-275, February 1994

[39] E Gulski and A Krivda, "Neural networks as a tool for recognition of partial discharges", IEEE Trans. on Electrical Insulation, Vol. 28, No. 6, pp. 984-1001, December 1993

[40] E Gockenbach and K Straßburg, "PD-measurement and localization in high voltage switchgears", Proc. 9th Int. Symp. on High Voltage Engineering (Graz), Vol. 5, 1995

[41] A G Sellars, S J MacGregor and O Farish, "Calibrating the UHF technique of partial discharge detection using a PD simulator", IEEE Trans. Dielectrics and Electrical Insulation, Vol. 2, No. 1, pp. 46-53, February 1995

[42] C-T Tai, *Dyadic Green's functions in electromagnetic theory*, 2nd Edition, IEEE Press, 1994

[43] R E Collin, *Field theory of guided waves*, McGraw-Hill, 1960

[44] J van Bladel, "Expandability of a wave-guide field in terms of normal modes", Journal of Applied Physics, Vol. 22, No. 1, pp. 68-69, January 1951

[45] N Marcuvitz, *Waveguide Handbook*, Peter Peregrinus Ltd, 1986

[46] M D Judd, O Farish and B F Hampton, "Modelling partial discharge excitation of UHF signals in waveguide structures using Green's functions", IEE Proc., Science, Measurement and Technology; Vol. 143, No. 1, pp. 63-70, January 1996

[47] G F Roach, *Green's functions: Introductory theory with applications*, Van Nostrand: London, 1970

[48] J J Freeman, "The field generated by an arbitrary current distribution within a waveguide", Journal of Research of the National Bureau of Standards, Vol. 44, pp. 193-198, February 1950

[49] J J Freeman, "Theory and design of a cavity attenuator", Journal of Research of the National Bureau of Standards, Vol. 40, pp. 235-243, March 1948

[50] *SCD1000 & 5000 Transient Waveform Recorders User Manual*, Tektronix Part No. 070-6960-02, 1992

[51] *Communications Components Designer's Catalogue, GaAs and Silicon Products*, Hewlett-Packard Co., 1993

[52] *LabVIEW for Windows User Manual*, National Instruments Corporation, Part No. 320534-01, December 1993

[53] *Mathcad User's Guide, Mathcad PLUS 6.0*, Mathsoft Inc., June 1995

[54] H J Schmitt, C W Harrison and C S Williams, "Calculated and experimental response of thin cylindrical antennas to pulse excitation", IEEE Trans. Antennas and Propagation, vol. AP-14, No. 2, pp. 120-127, March 1966

[55] C W Harrison, "The radian effective half-length of cylindrical antennas less than 1.3 wavelengths long", IEEE Trans. Antennas and Propagation, vol. AP-11, No. 6, pp. 657-660, November 1963

[56] G A Thiele, "Calculation of the current distribution on a thin linear antenna", IEEE Trans. on Antennas and Propagation, Vol. AP-14, No. 5, pp. 648-649, September 1966

[57] S L Dvorak and D G Dudley, "Propagation of ultra-wide-band electromagnetic pulses through dispersive media", IEEE Trans. on Electromagnetic Compatibility, Vol. 37, No. 2, pp. 192-200, May 1995

[58] D Kralj, L Mei, T-T Hsu and L Carin, "Short-pulse propagation in a hollow waveguide: Analysis, optoelectronic measurement, and signal processing", IEEE Trans. on Microwave Theory and Techniques, Vol. 43, No. 9, pp. 2144-2150, September 1995

[59] Staff of the R.E.A., *Handbook of Mathematical, Scientific and Engineering formulas, tables, functions, graphs, transforms*, Research and Education Association, 1988

[60] E O Schulz-DuBois, "Sommerfeld pre- and postcursors in the context of waveguide transients", IEEE Trans. Microwave Theory and Techniques, vol. MTT-18, No. 8, pp. 455-460, August 1970

[61] P Pleshko and I Palocz, "Experimental observation of Sommerfeld and Brillouin precursors in the microwave domain", Physical Review Letters, Vol. 22, No. 22, pp. 1201-1204, June 1969

[62] W A Saxton and H J Schmitt, "Transients in a large waveguide", Proc. IEEE (Correspondence), Vol. 51, pp. 405-406, February 1963

[63] S Pack, A Diessner and J Gorablenkow, "PD signal propagation in GIS considering frequencies up to GHz", Proc. 8th Int. Symp. on High Voltage Engineering (Yokohama), Vol. 3, pp. 93-96, 1993

[64] R Witzmann, "Fast transients in gas insulated substations (GIS) - modeling of different GIS components", Proc. 5th Int. Symp. on High Voltage Engineering (Braunschweig), paper No. 12.06, 1987

[65] R Kurrer, K Feser and I Herbst, "Calculation of resonant frequencies in GIS for UHF partial discharge detection", Gaseous Dielectrics VII, Plenum Press, pp. 557-563, 1994

[66] A G Sellars, B F Hampton and O Farish, "Identifying the streamer-leader transition in SF_6 using the UHF technique", Proc. 8th Int. Symp. on High Voltage Engineering (Yokohama), pp. 279-282, 1993

[67] S Matsumura and T Nitta, "Surge propagation in gas insulated substations", IEEE Trans. Power Apparatus and Systems, Vol. PAS-100, No. 6, pp. 3047-3054, June 1981

[68] J M M e Silva, J S Pearson, B F Hampton and O Farish, "PD measurements in GIS using portable equipment", Proc. 9th Int. Symp. on High Voltage Engineering (Graz), Vol. 4, 1995

[69] M D Judd, B F Hampton and O Farish, "Partial discharge excitation of UHF modes in a cylindrical cavity", Proc. 9th Int. Symp. on High Voltage Engineering (Graz), Vol. 4, 1995

[70] S A Boggs, "Electromagnetic techniques for fault and partial discharge location in gas-insulated cables and substations", IEEE Trans. Power Apparatus and Systems, Vol. PAS-101, No. 7, pp. 1935-1941, July 1982

10. PUBLICATIONS

1)   M D Judd, "Evaluation of the circular metal plate as a UHF coupler for partial discharge monitoring", IEE Colloquium Digest 1994/093, pp. 7/1-7/4, April 1994

2)   M D Judd, O Farish and B F Hampton, "Broadband couplers for UHF detection of partial discharge in gas insulated substations", IEE Proc., Science, Measurement and Technology, Vol. 142, No. 3, pp. 237-243, May 1995

3)   M D Judd, "UHF signals and partial discharges in GIS", CIGRE Working Group 15/33.03.05 - IWD 5, June 1995

4)   M D Judd, B F Hampton and O Farish, "Partial discharge excitation of UHF modes in a cylindrical cavity", Proc. 9th Int. Symp. on High Voltage Engineering (Graz), Vol. 4, 1995

5)   M D Judd, O Farish and B F Hampton, "Modelling partial discharge excitation of UHF signals in waveguide structures using Green's functions", IEE Proc., Science, Measurement and Technology, Vol. 143, No. 1, pp. 63-70, January 1996

6)   M D Judd, O Farish and B F Hampton, "Excitation of UHF signals by partial discharges in GIS", IEEE Trans. Dielectrics and Electrical Insulation, Vol. 3, No. 2, pp. 213-228, April 1996